Carbon Nanotube Porin Based Biosensors

by

Xi Chen

A dissertation submitted in partial satisfaction of the

requirements for the degree of

Doctor of Philosophy

in

Chemistry and Chemical Biology

in the

Graduate Division

of the

University of California, Merced

Committee in charge:

Professor Michael E. Colvin, Chair
Professor Aleksandr Noy, Advisor
Professor Ajay Gopinathan
Professor Marco Rolandi
Professor Tao Ye

Spring 2020

The dissertation of Xi Chen, titled Carbon Nanotube Porin Based Biosensors, is approved:

Chair _____ Date _____

Professor Michael E. Colvin

_____ Date _____

Professor Aleksandr Noy

_____ Date _____

Professor Ajay Gopinathan

_____ Date _____

Professor Marco Rolandi

_____ Date _____

Professor Tao Ye

University of California, Merced

Carbon Nanotube Porin Based Biosensors

Abstract

Carbon Nanotube Porin Based Biosensors

by

Xi Chen

Doctor of Philosophy in Chemistry and Chemical Biology

University of California, Merced

Advisor: Professor Aleksandr Noy

The biomimetic structures of carbon nanotube porins and lipid membranes provide a membrane coating to isolate biosensor surface from potential foulants present in biological fouling solution. The lipid membranes mimic cellular membrane while the ultrashort carbon nanotube porins mimic the structure and functionalities of membrane protein channels. This versatile biosensor platform enables the ion sensing at nano-bio interfaces and opens up the potential for intracellular and multimodal sensing.

In this dissertation, I will review the properties and advantages of carbon nanotubes in the nanofluidics field. I will report the optimization of high-yield synthesis of carbon nanotube porins, the biomimetic nanochannels in membranes. I will also discuss the fully synthetic membrane with incorporation of carbon nanotube porins into a block-copolymer matrix. In addition, I will present a biomimetic approach for creating fouling-resistant pH sensors by integrating silicon nanoribbon transistor sensors with an antifouling lipid bilayer coating that contains proton-permeable carbon nanotube porin channels and demonstrate robust pH detection in a variety of complex biological fluids. And lastly I will describe potential applications of the carbon nanotube porin based biosensor platform.

To My Family

Life is a journey,

not a destination.

- Ralph Waldo Emerson

Contents

List of Figures

List of Tables

Acknowledgments

I would like to express my sincere gratitude to many people through my journey. Over these years, I have had great guidance and support towards my Ph.D. degree. This dissertation would not have been completed without them.

First and foremost, I would like to thank my advisor Prof. Aleksandr Noy. I am deeply grateful for his continuous and unwavering support. There are ups and downs during my graduate studies. And I could always rely on his insightful comments and kind encouragement.

I would also like to express my deepest appreciation to my dissertation committee professors, Prof. Michael E. Colvin and Prof. Tao Ye from Department of Chemistry and Chemical Biology, Prof. Ajay Gopinathan from Department of Physics, and Prof. Marco Rolandi from Department of Electrical and Computer Engineering at UC Santa Cruz. I would never have finished my doctoral studies without the guidance and support from my committee professors.

I would like to acknowledge Physical and Life Sciences Directorate in Lawrence Livermore National Laboratory (LLNL) and the Molecular Foundry in Lawrence Berkeley National Laboratory (LBNL) for allowing me to use the resources and facilities for my research. It would be impossible for me to carry out most of my experiments without the access to these two labs.

I would also like to extend my appreciation to the research staff scientists and engineering associates in LBNL and LLNL, Dr. Stefano Cabrini, Dr. Scott Dhuey, Michael Elowson, Dr. Caroline Ajo-Franklin, Dr. Virginia Altoe, Dr. Alex Weber-Bargioni, Dr. Doris Lam, Dr. Nick Fischer, Dr. Heather Enright, and Nicholas Hum.

I am thankful for the funding from UC-National Lab In-residence Graduate Fellowship in the UC National Laboratory Fees Research Program.

I want to give special thanks to Dr. Yuliang Zhang for his support and companion throughout my entire PhD studies. He is my go-to person whenever I needed suggestions, no matter what the problem is. I am fortunate to have him around.

It is my pleasure to acknowledge all the help I got from the Noy group members: Dr. Jia Geng, Dr. Ramya Tunuguntla, Dr. Huanan Zhang, Dr. Jeremy Sanborn, Dr. Nga Ho, Dr. Yuhao Li, Dr. Margaryta Sheliakina, Joyce Yao, Wu Zhan and Zhongwu Li.

Last but not least, I would like to thank my family. I owe a lot to my parents, Jianjun Chen and Xia Dong, who encouraged me for my entire life. Thank you for your support and your faith in me. I would like to thank my beloved wife, Xi Chen, for your continued love and being supportive of me. I would not be where I am today without you.

Chapter 1

Introduction

The interface between biological systems and nanoelectronics allows the interaction and communication between natural and synthetic systems. It serves as a powerful toolkit to interpret complicated yet fascinating processes of living systems in a way that can be readily understood by current technologies. Biological signaling mechanisms often involve small molecules, ions [1], and protons and facile *in situ* monitoring of the levels of these species is vital for medical diagnostics. Even the simplest signals, such as intracellular pH level can provide important information: for example, acidification of tumors because of elevated glucose uptake and lactic acid release is a biomarker of cancer cells [2] (Figure 1.1). Acidification of extracellular fluid is also one of the key processes during epileptic seizures, and monitoring and controlling pH of extracellular fluid has diagnostic and therapeutic potential [3]. Another example is diabetes insipidus, which is caused by the improper response of kidney to Vasopressin (ADH). Depending on the different types of the condition (Nephrogenic, Dipsogenic, and Hypothalamic), it has different treatment plan. Unfortunately, this condition is often recognized late after a "diagnostic odyssey" involving false leads and dangerous treatments [4]. If we can monitor the Na^+/K^+ imbalance to help diagnosis at an early stage, appropriate treatment can be initiated to achieve urinary concentration independent of vasopressin, avoiding a lot of tragedies. The list of examples could go on and on. This and other challenges have motivated me to develop a biosensor platform that can achieve ion sensing at the nano-bio interface to enable medical diagnosis.

Of all biosensing platforms, electrical sensors represent the best opportunity to develop implantable long-term sensing platforms because of their typically high sensitivity levels, fast response, and ease of multiplexing, signal processing, and coupling to wireless readout components [6, 7]. Although ion-selective electrodes represent the most ubiquitous electrical ion sensing platform, field effect transistors (FETs) have matured into a versatile alter-

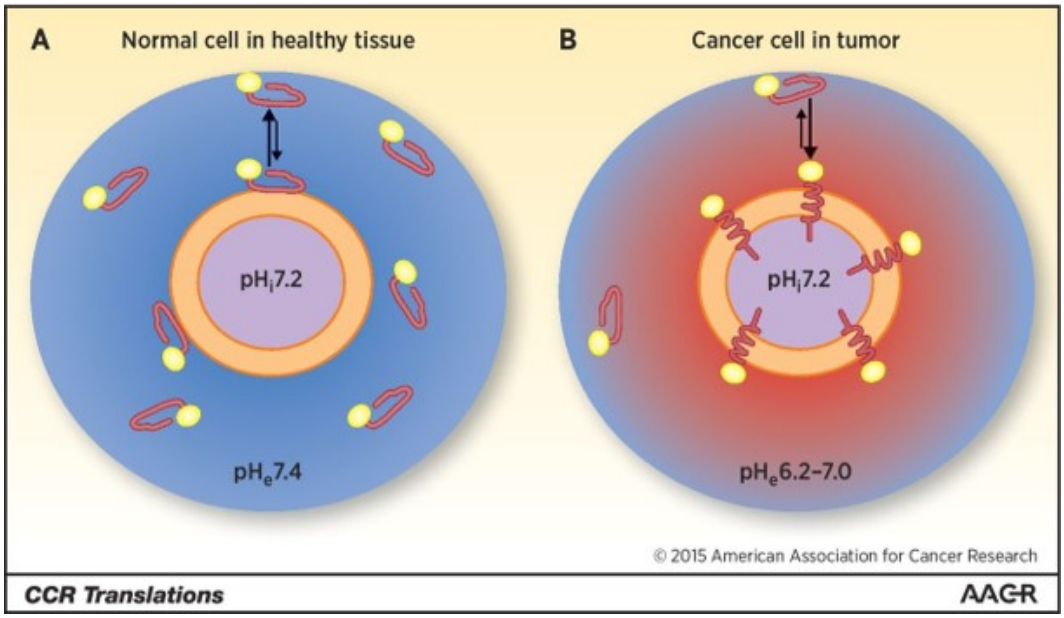

Figure 1.1: Schematic presentation of (A) normal cell in healthy tissue and (B) cancer cell in tumor. The extracellular pH in healthy tissue is around pH = 7.4 while pH in tumor can be as low as pH = 6.2. (Reproduced with permission from [5]. © *2015 American Association for Cancer Research*).

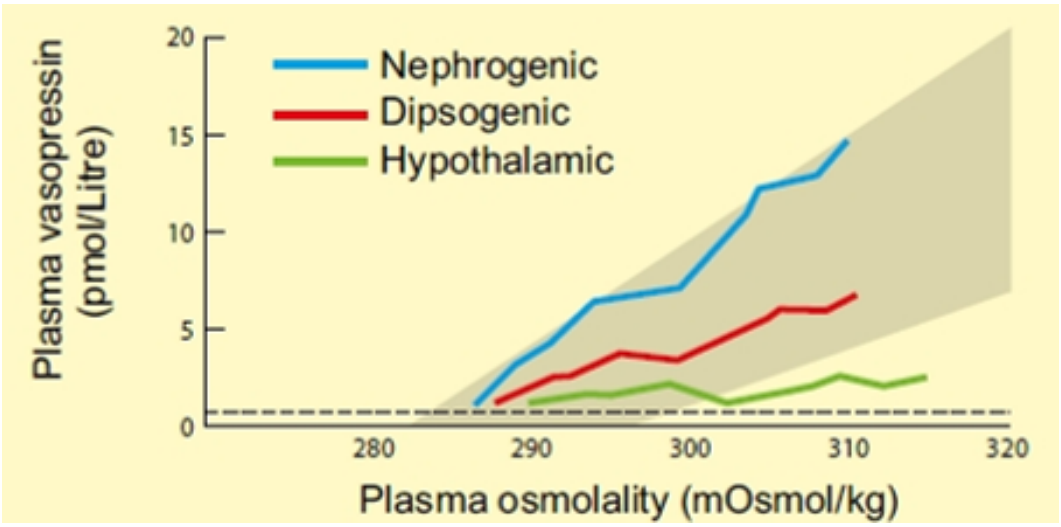

Figure 1.2: Vasopressin response to plasma osmolality for different types of diabetes insipidus. (Reproduced with permission from [4]. © *2006 American College of Physicians*).

native sensing platform that excels at continuous monitoring of small analyte levels [8]. FET sensors typically respond to the changes in the surface potential on the device channel region due to analyte binding or local ionization events and then amplify this signal using the high intrinsic transistor gain. Silicon nanowire/nanoribbon devices that exploited tailorable nature of silicon, advances in nanowire synthesis, and the existing mature silicon processing technologies have developed into a versatile platform for real-time, label-free, highly sensitive detection of disease biomarkers [9–13], DNA mismatches [14–16], and viruses [17].

However, due to the nature of biological materials (high ionic concentration), large background noise resulting from non-specific absorption and fouling propensity of the sensitive device surface, there are limitations to the FET-based biosensing and diagnostic platforms. As the platforms move into the realms of clinical use and potentially even long-term implantable applications, some of the limitations come into sharp relief, especially those related to device fouling in complex fluid environments.

Researchers have used different fouling mitigation strategies based on polymeric surface coatings [18–20], bioinspired functionalization approaches [21, 22], and low-adhesion coatings [23]. Another general strategy to mitigate fouling is based on separating the sensing surface, which houses the analyte targets, from the measuring surface of the FET device. To implement this strategy, researchers developed sensors with side gate [24], floating gate [25, 26], and dual gate [27, 28]. In both cases, purification/filtering-separation-preconcentration process is inevitable.

In this dissertation, I proposed an alternative strategy that uses a semipermeable lipid membrane coating on a device to isolate the sensor surface from the sensing solution. They are self-healing, easy to form on sensor surface, and fouling-resistant to large molecules. The lipid membranes mimic cellular membrane and are universal matrix for housing transmembrane proteins [29]. They can act as a versatile platform for creating nanoelectronics with and assembly of synthetic membrane channel to mimic biological protein pore. In order to perform the sensing ability as designed, we need to incorporate specific membrane channels that can self-insert into the lipid membranes and only allow species of interest to reach the device sensing surface. Previously, Noy group have demonstrated the versatility of this approach by creating SiNW FET devices that incorporate specific ion channels [30], and ion pumps [31]. The channels Noy group used are **Carbon Nanotube Porins**, or CNTPs (Figure 1.3) [32, 33]. Carbon Nanotube Porins are biomimetic analogs of biological protein channels. CNTPs are named due to they resemble the structure of β-barrel structure of porin proteins and the functionality of self-insertion into lipid membranes.

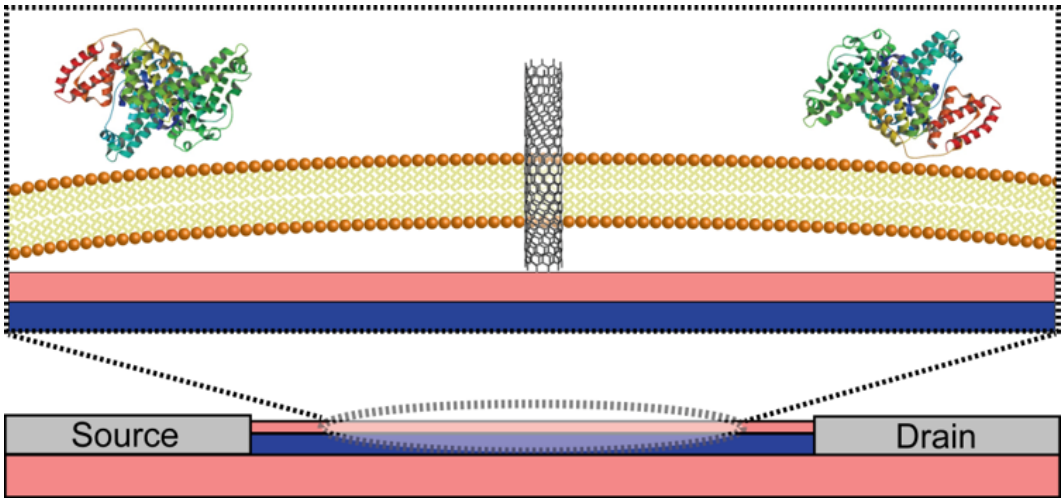

Figure 1.3: Schematic illustration of CNTP-lipid membrane passivation on sensor surface. The lipid membrane coating will work as protection layer to inhibit foulants adsorb on sensor surface. Carbon Nanotube Porins will self-insert into the membrane, allowing small ions to go through, thus maintaining the ion sensing ability of sensors.

1.1 Biomimetic carbon nanotube porins

Carbon has been one of the most important elements in nanobioelectronics. Not only because it is the dominant element in organic living systems, but also because of a variety of allotropes of Carbon, especially those nanoscale allotropes. Fullerene (Buckminsterfullerene, C_{60}) was acknowledged by Nobel Prize in Chemistry in 1996 for its discovery. It is sometimes deemed as zero-dimensional (0D) Carbon nanostructure. Graphene was acknowledged by Nobel Prize in Physics in 2010 for a series of groundbreaking experimental studies on its properties. It is often described as the two-dimensional (2D) materials. Their one-dimensional (1D) cousin, Carbon Nanotubes (CNTs), even though haven't won any Nobel Prizes yet, have been acknowledged by the Benjamin Franklin Medal in Physics in 2002. These nanoscale materials draw research interests due to their unique properties caused by quantum confinement.

Carbon nanotubes have smooth, narrow and hydrophobic inner surface. These make them the perfect candidate for the synthetic transmembrane channels we need. They also have ultrafast water and ion transport rate as well as biologically relevant pore sizes. In addition, their pore diameters, rim functionality, etc. can be controlled to achieve selectivity that rivals biological

membrane channels. We just need to have a much shorter CNT structure with a length comparable to the thickness of lipid membrane to provide a closer match to the protein in membrane structure. They also need to self-insert into lipid membrane spontaneously to enable efficient transport of water, ion and small molecules across the lipid bilayer, just like the common behaviors in biological channels. We used sonochemical cutting to synthesize carbon nanotube porins (CNTPs) [32, 34], about 10 nm carbon nanotube (CNT) segments that spontaneously insert into lipid or polymer membranes and form transmembrane channels. CNTPs have extremely high ion permeability that is an order of magnitude higher than bulk permeability. Inert smooth surface of narrow CNT pores that is responsible for creating conditions that favor fast ionic transport, also ensures that CNTPs can effectively block most of the fouling components of biological mixtures and prevent them from reaching the sensor surface.

1.2 Scope of this dissertation

The objective of my dissertation is to achieve high-yield synthesis of Carbon Nanotube Porins; investigate the properties of this biomimetic transmembrane channel in lipid and polymer membranes; and use CNTPs in lipid passivation to achieve an anti-fouling biosensing platform. This dissertation is organized in the following five chapters.

In Chapter 2, I will review the unique properties of Carbon Nanotubes and their outstanding performance in nanofluidics field.

In Chapter 3, I will present a generalized approach for CNTP synthesis using sonochemistry assisted segmenting of carbon nanotubes. I will discuss the main parameters that determine the efficiency and the yield of this process, describe the optimized conditions for high-yield CNTP synthesis, and demonstrate that this methodology can be adapted for synthesis of CNTPs of different diameters. I will also present the optical properties of CNTPs and show that a combination of Raman and UV-vis-NIR spectroscopy can be used to monitor the quality of the CNTP synthesis.

In Chapter 4, I will report a fully synthetic biomimetic membrane with CNTPs incorporated into a block-copolymer matrix. I will demonstrate CNTPs maintain high proton and water permeability in these membranes. CNTPs can also mimic the behavior of biological gap junctions by forming bridges between vesicular compartments that allow transport of small molecules.

In Chapter 5, I will present a biomimetic approach for creating fouling-resistant pH sensors. I integrate silicon nanoribbon transistor sensors with an antifouling lipid bilayer coating that contains proton-permeable CNTP chan-

nels and demonstrate robust pH detection in a variety of complex biological fluids.

In Chapter 6, I will describe other potential uses of this Carbon Nanotube Porin based biosensors platform. Some exploratory design ideas for this CNTP based sensing platform are conceptualized: (a), using CNTPs as cellular interface to achieve intracellular recording; (b), functionalizing the rim of CNTPs through EDC coupling to realize tailorable channels thus allowing specific ions transport for selective sensors; and (c), making a multimodal biosensor by adopting receptors for different ions and differential setup to probe different ions' concentrations simultaneously. Overall, CNTPs represent a versatile nanopore building block for creating higher-order functional biomimetic materials.

References

(1) Alberts, B. et al. Mol Biol Cell (Garland Science, New York), 2002.

(2) Damaghi, M.; Wojtkowiak, J. W.; Gillies, R. J. *Frontiers in physiology* **2013**, *4*, 370.

(3) Pavlov, I.; Kaila, K.; Kullmann, D. M.; Miles, R. *The Journal of physiology* **2013**, *591*, 765–774.

(4) Sands, J. M.; Bichet, D. G. *Annals of Internal Medicine* **2006**, *144*, 186–194.

(5) Reshetnyak, Y. K. *Clinical Cancer Research* **2015**, *21*, 4502–4504.

(6) Ronkainen, N. J.; Halsall, H. B.; Heineman, W. R. *Chemical Society Reviews* **2010**, *39*, 1747–1763.

(7) Lin, P.; Yan, F.; Chan, H. L. *ACS applied materials & interfaces* **2010**, *2*, 1637–1641.

(8) Chen, K.-I.; Li, B.-R.; Chen, Y.-T. *Nano today* **2011**, *6*, 131–154.

(9) Zheng, G.; Patolsky, F.; Cui, Y.; Wang, W. U.; Lieber, C. M. *Nature biotechnology* **2005**, *23*, 1294.

(10) Lin, T.-W.; Hsieh, P.-J.; Lin, C.-L.; Fang, Y.-Y.; Yang, J.-X.; Tsai, C.-C.; Chiang, P.-L.; Pan, C.-Y.; Chen, Y.-T. *Proceedings of the National Academy of Sciences* **2010**, *107*, 1047–1052.

(11) Wang, W. U.; Chen, C.; Lin, K.-h.; Fang, Y.; Lieber, C. M. *Proceedings of the National Academy of Sciences* **2005**, *102*, 3208–3212.

(12) Chua, J. H.; Chee, R.-E.; Agarwal, A.; Wong, S. M.; Zhang, G.-J. *Analytical chemistry* **2009**, *81*, 6266–6271.

(13) Stern, E.; Klemic, J. F.; Routenberg, D. A.; Wyrembak, P. N.; Turner-Evans, D. B.; Hamilton, A. D.; LaVan, D. A.; Fahmy, T. M.; Reed, M. A. *Nature* **2007**, *445*, 519.

(14) Hahm, J.-i.; Lieber, C. M. *Nano letters* **2004**, *4*, 51–54.

(15) Li, Z.; Chen, Y.; Li, X.; Kamins, T.; Nauka, K.; Williams, R. S. *Nano Letters* **2004**, *4*, 245–247.

(16) Ganguly, A.; Chen, C.-P.; Lai, Y.-T.; Kuo, C.-C.; Hsu, C.-W.; Chen, K.-H.; Chen, L.-C. *Journal of Materials Chemistry* **2009**, *19*, 928–933.

(17) Patolsky, F.; Zheng, G.; Hayden, O.; Lakadamyali, M.; Zhuang, X.; Lieber, C. M. *Proceedings of the National Academy of Sciences* **2004**, *101*, 14017–14022.

(18) Banerjee, I.; Pangule, R. C.; Kane, R. S. *Advanced materials* **2011**, *23*, 690–718.

(19) Krishnan, S.; Weinman, C. J.; Ober, C. K. *Journal of Materials Chemistry* **2008**, *18*, 3405–3413.

(20) Vaisocherová, H.; Brynda, E.; Homola, J. *Analytical and bioanalytical chemistry* **2015**, *407*, 3927–3953.

(21) Zhang, P.; Lin, L.; Zang, D.; Guo, X.; Liu, M. *Small* **2017**, *13*, 1503334.

(22) Nir, S.; Reches, M. *Current opinion in biotechnology* **2016**, *39*, 48–55.

(23) Detty, M. R.; Ciriminna, R.; Bright, F. V.; Pagliaro, M. *Accounts of chemical research* **2014**, *47*, 678–687.

(24) White, S. P.; Sreevatsan, S.; Frisbie, C. D.; Dorfman, K. D. *ACS Sensors* **2016**, *1*, 1213–1216.

(25) Meyburg, S.; Goryll, M.; Moers, J.; Ingebrandt, S.; Böcker-Meffert, S.; Lüth, H.; Offenhäusser, A. *Biosensors and bioelectronics* **2006**, *21*, 1037–1044.

(26) Meyburg, S.; Stockmann, R.; Moers, J.; Offenhäusser, A.; Ingebrandt, S. *Sensors and Actuators B: Chemical* **2007**, *128*, 208–217.

(27) Wu, T.; Alharbi, A.; You, K.-D.; Kisslinger, K.; Stach, E. A.; Shahrjerdi, D. *ACS nano* **2017**, *11*, 7142–7147.

(28) Ahn, J.-H.; Choi, S.-J.; Han, J.-W.; Park, T. J.; Lee, S. Y.; Choi, Y.-K. *Nano letters* **2010**, *10*, 2934–2938.

(29) Groves, J. In *BioMEMS and Biomedical Nanotechnology*; Springer: 2006, pp 305–323.

(30) Misra, N.; Martinez, J. A.; Huang, S.-C. J.; Wang, Y.; Stroeve, P.; Grigoropoulos, C. P.; Noy, A. *Proceedings of the National Academy of Sciences* **2009**, *106*, 13780–13784.

(31) Huang, S.-C. J.; Artyukhin, A. B.; Misra, N.; Martinez, J. A.; Stroeve, P. A.; Grigoropoulos, C. P.; Ju, J.-W. W.; Noy, A. *Nano letters* **2010**, *10*, 1812–1816.

(32) Geng, J.; Kim, K.; Zhang, J.; Escalada, A.; Tunuguntla, R.; Comolli, L. R.; Allen, F. I.; Shnyrova, A. V.; Cho, K. R.; Munoz, D., et al. *Nature* **2014**, *514*, 612.

(33) Tunuguntla, R. H.; Escalada, A.; Frolov, V. A.; Noy, A. *Nature protocols* **2016**, *11*, 2029.

(34) Tunuguntla, R. H.; Allen, F. I.; Kim, K.; Belliveau, A.; Noy, A. *Nature nanotechnology* **2016**, *11*, 639.

Chapter 2

Carbon Nanotubes in Nanofluidics

2.1 Introduction

Carbon nanotubes (CNTs) were first observed by transmission electron microscopy (TEM) in 1991 [1]. Ever since the discovery of single wall carbon nanotubes (SWCNTs) in 1993 [2, 3] these cylinders of carbon atoms with thickness of one atomic layer have found extensive applications in a number of research areas [4] and become a truly iconic molecule of nanotechnology. Subsequent synthetic breakthroughs allowed production of large quantities of high-purity single wall CNTs with a small diameter distribution [5, 6]. High resolution TEM, scanning tunneling microscopy (STM), and Raman scattering measurements have shown that SWCNTs exist as rolled-up seamless graphene cylinders with sp^2 bonded carbon atoms organized into a honeycomb structure (Figure 2.1). This roll-up vector (n, m) determines the key parameters of a CNT - diameter and chirality [7]. Depending on the chirality (i.e the chiral angle between hexagons and the tube axis), SWCNTs can behave as metallic or semiconducting molecules (with band gaps that range from ca. 10 meV to 0.5 eV for a typical diameter of 1.5nm) even if they have nearly identical diameters [7]. Intensive effort has been made to study the electronic properties of nanotubes and their atomic structures [8–12]. Metallic CNTs are ideal for studying quantum phenomena in quasi 1D solids, including single electron charging, Luttinger Liquid, weak localization, ballistic transport and quantum interference [8–10, 13, 14] while semiconducting CNTs are utilized as a perfect building blocks for nanoelectronics, e.g. transistors, logic gates, memory

Part of this work has been submitted as a book chapter: Transport in Carbon Nanotube Pores: Implications for next generation water purification technologies. *World Scientific Publishing Company* , **2020**, submitted.

devices and sensors [8–12].

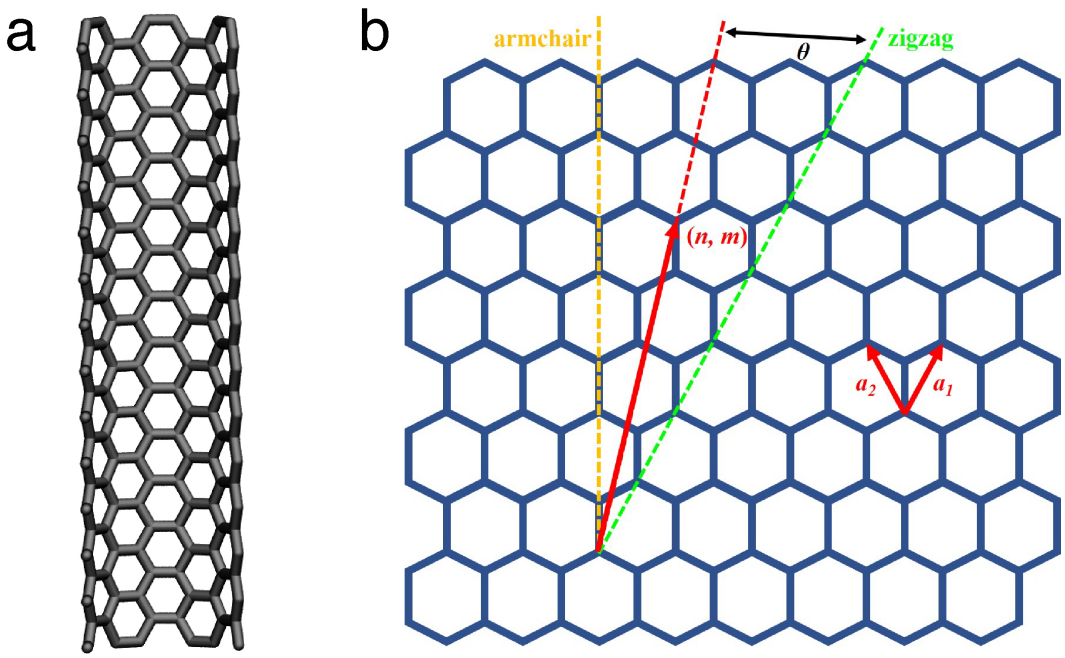

Figure 2.1: (a) A molecular model of a single-wall carbon nanotube. Half of the nanotube closest to the viewer was removed for clarity. (b). A schematic illustration of honeycomb structure of a graphene sheet that can be folded into single-walled carbon nanotubes along the lattice vectors.

2.2 Structure

Structure of single wall CNTs is determined by the diameter d, and chiral angle θ (Figure 2.1). The chiral angle is commonly defined between 0 and 30 degrees (0° to denote zigzag CNTs, 30° to denote armchair CNTs). The circumference of CNT can be expressed by the chiral vector ($\overrightarrow{C} = n\overrightarrow{a_1} + m\overrightarrow{a_2}$, $\overrightarrow{a_1}$ and $\overrightarrow{a_2}$ are the unit vectors of the hexagonal graphene honeycomb lattice) connecting two crystallographically equivalent sites on the 2D graphene sheet [15]. The superimposition of two edges perpendicular to the vector $\overrightarrow{C}$ yields the chiral CNT structure, which has no distortion of bond angles other than the distortions caused by the cylindrical curvature of the CNT itself.

Alternatively, we can use the (n,m) notation where the chiral vectors (n,0) and (0,m) denote zigzag CNTs; (n,n) denotes armchair CNTs, while the others

denote chiral CNTs [16]. The diameter d of a CNT is given by

$$d = \frac{\sqrt{3}a}{\pi}(m^2 + mn + n^2)^{1/2}$$

where the nearest neighboring carbon atoms have a distance of $a = 1.44$Å, and the chiral angle is given by

$$\theta = tan^{-1}\frac{\sqrt{3}n}{2m + n}$$

.

2.3 Synthesis

CNTs are synthesized by three major methods: arc discharge, laser ablation and chemical vapor deposition (CVD) [12]. The earliest CNTs were produced by the Iijima group using arc discharge methods where CNTs were formed as bundles on the negative electrode, and the positive electrode was consumed in a helium atmosphere [17]. Typical lengths of the grown CNTs were in μm ranges, yielding an aspect ratio of 10^2 to 10^6. The very first single wall CNTs were also synthesized in an arc discharge chamber with Fe, Co and other transition metals as catalysts [2, 3]. Smalley group introduced the first synthetic breakthrough when they developed a more efficient synthesis route using laser ablation [5]. This method uses a Co-Ni/graphite composite target operating in a furnace at 1200°C yielding 70-90% conversion of graphite to SWCNTs. Argon gases sweep the CNTs from high temperature zone to a water cooled Cu collector downstream outside of the furnace. An even more significant advance came when researchers developed CVD synthesis of SWCNTs using hydrocarbon decomposition over transition metal catalyst nanoparticles [18, 19].

Arc discharge and laser ablation use solid state carbon precursors to provide carbon source for the CNT growth, which involves carbon vaporization at high temperature. They can consistently yield high quality and near-perfect CNT structures, even though large amount of amorphous carbon and other byproducts are inevitable. CVD, on the other hand, utilizes hydrocarbon gases as sources and catalyst particles as seeds for CNT growth. This process happens at comparatively lower temperatures of 500-1000°C [12]. Even though none of these three methods can yet produce large amount of CNTs with identical diameters and chirality, catalytic chemical vapor deposition is preferred over the other two methods [5, 6] due to its ability to produce both individually isolated nanotubes and densely packed vertically aligned arrays [12, 20–25]. Previous studies show that the most probable diameter and the width of the

diameter distribution is determined by the size and composition of the catalyst particle, growth temperature and other growth conditions [26–28], even though this control is still far from perfect.

2.4 Mechanical properties

CNTs have excellent mechanical properties, exhibiting no cross-sectional and twisting distortions. They can be bent and elongated/compressed without fracture. This excellent flexibility is in good agreement with their high tensile strength and bulk modulus [29]. Even CVD-grown CNTs with relatively larger diameters ($\sim 10nm$) can bend, twist and kink without fracturing [30, 31]. CNTs also show excellent mechanical properties when compressed and can form kink-like structures that can relax elastically then the stress is released [32, 33]. These properties bode well for the perspective of incorporating CNTs into membrane structures.

CNTs are also a very hard and tough material. The Young's modulus (Y) of small diameter single wall CNT is in the range of several TPa [34]. The tensile strain to failure can be as high as 40% [33]. Raman spectroscopy has been used to indirectly calculate the Young's modulus in both single-wall [35] and multi-wall [36] CNTs by measuring the shift with strain of the frequency of second-order Raman band in the region of $2600 - 2700cm^{-1}$.

2.5 Electronic structure

Carbon nanotubes have circumferential periodic boundary condition applied to the unit cell that is formed in the real space. The 1D electronic energy band structure for CNTs is related to the structure for the 2D graphene sheet used to form the CNTs [37–41] . Depending on the nanotube diameter d and chiral angle θ, CNTs can be metallic and semiconducting. Metallic conduction in a (n, m) carbon nanotube can only be achieved when $2n + m = 3q$, where q is an integer. This is also why the majority of CNTs synthesized are semiconducting in nature. All armchair carbon nanotubes ($\theta = 30°$, (n, n)) are metallic.

The electronic structure of CNT is a graphene sheet (which is a zero bandgap Dirac-Fermi cone) with bonding and antibonding π bands that are degenerate at the K-point (zone corner) of the hexagonal 2D Brillouin zone. The periodic boundary conditions for CNTs only allow few wave vectors to exist in the circumferential direction, and these wave vectors k satisfy the relation $n\lambda = \pi d$ where $\lambda = 2\pi/k$ is the de Broglie wavelength. Metallic conduction can only be achieved when wave vectors k passes through the K-

point of the 2D Brillouin zone, where the valence and conduction bands are degenerate because of the special symmetry of the 2D graphene lattice [42].

As the CNT diameter increases, more wave vectors are allowed for the circumferential direction, so that the nanotubes become more two-dimensional and the semiconducting band gap disappears. The semiconducting band gap is proportional to the reciprocal CNT diameter

$$Eg = \frac{2\gamma a}{d}$$

, where $a = 1.44$ Å is the nearest neighboring carbon atoms distance and the nearest neighbor overlap integral (or transfer integral) γ is found to be 2.7 eV [43, 44]. When d approaches ca. 3 nm, the band gap becomes comparable to kT at room temperature, marking the upper threshold for 1D quantum effects.

The density of states (DOS) of CNTs determines the 1D dispersion relations. Sharp singularities associated with $(E - E_0)^{-1/2}$ dependence are expected at subband edge where $k = 0$. Metallic CNTs have small yet non-vanishing DOS at Fermi level ($E = 0$), which is independent of the energy up to the first subband edges of valence and conduction bands are filled. On the other hand, the DOS for semiconducting CNTs is zero at the band gap. The band gap E_g is the energy difference between the singularities in the DOS at Fermi level. Due to these singularities, high optical absorption is can be achieved when the photon energy matches the separation between occupied state and empty one. This can happen at the band gap for semiconducting CNTs. For both semiconducting and metallic CNTs, transitions can also happen at higher energies from an occupied subband edge state to the corresponding unoccupied edge state.

In terms of the electronic properties, like mentioned above, majority of CNTs synthesized are semiconducting in nature. Most CVD synthesized CNTs are hole-doped p-type FETs with hole depletion and diminished conductance (100 $k\Omega$ to 1 $M\Omega$). The molecular oxygen adsorbed on the CNTs is responsible for the hole doping [45–48]. And removal of O_2 can lead to nearly intrinsic semiconducting behavior [48]. There is also another type of CNTs synthesized by CVD can be quasi-metallic with E_g on the order of $10meV$ [49]. These CNTs are not sensitive to electrostatic doping but exhibit a conductance dip associated with the small E_g. The small E_g is due to the slight sp^2 to sp^3 hybridization originated from the nonflat nature of the hexagons on the tube walls [50, 51]. The conductance of these quasi-metallic CNTs will increase as the temperature decreases. The quantum conductance limit $4e^2/h = 2G_0$ $= (6.45\times10^3\ \Omega)^{-1}$ is reached at $\sim$1.5 K (compared to the room temperature resistance of $\sim$ 10 -20 $k\Omega$). Electron transport is highly phase coherent and ballistic in CNTs at low temperatures. Quantum interference effects have also been reported [14].

2.6 Transport properties

Single wall carbon nanotubes have been an ideal example of studying the electronic structure and transistor effects [52–54]. Due to the scope of this chapter, we will briefly cover the electron transport but not go into details here.

Interaction with environment (like van der Waals interaction with the substrate), structural imperfections, bends or twists in the CNTs can localize the electron conduction. For a fixed degree of disorder, the mean free path of the electrons increases with decreasing CNT diameters. If the CNT diameter is small enough ($d \sim 1.4$ nm), the localization lengths will be long enough (~ 10 μm) to enable ballistic transport.

Coulomb charging effects will happen at low temperature, when CNTs (capacitors with capacitance C) have a thermal energy kT smaller than the charging energy $E_{charging} = e^2/2C$ for individual electrons. Coulomb blockade will happen when the current is blocked by $E_{charging}$ which shifts levels out of the tunneling window for conducting channels.

We can expect to observe steps in conductance for CNTs, the perfect and probably the most famous example of 1D materials. This is due to the steps in quantum conductance and the charging effects associated with capacitance of the CNTs and the gate. The conductance step is $G_0 = 2e^2/h$=$(12.9\times10^3$ $\Omega)^{-1}$, which corresponds to a single conductance channel.

Transport measurements indicate that the IV characteristics for CNTs are ohmic at room temperature [55]. There will be reduction in conductance for low temperature, which can be explained by single electron tunneling through small band gap within the Coulomb blockade framework. This increase in resistance with decreasing temperature deviates from Fermi-liquid behavior due to the strong 1D properties [56] and tube-tube interaction [57], indicating Coulomb interactions between electrons near Fermi level results in a Luttinger-liquid behavior in CNTs. Resistance measurements categorize CNTs into semiconducting with resistivity $\sim 10^1$ Ω·cm and metallic ones in the range of $10^{-4} \sim 10^{-3}$ Ω·cm. The Seebeck coefficient S at room temperature is $\sim +50\pm10\mu$V/K and has a non-linear temperature dependence [58, 59].

2.7 Vibrational spectra of CNTs

Phonon dispersion relations in CNTs can be studied via those of graphene using a zone folding approach [60–62]. When the lengths are much larger than the diameters, CNTs can be described in the 1D limit: the length is infinite; k points are continuous; and the contributions from the cap Carbon atoms

can be neglected. The same as almost all the other properties, the phonon dispersion relations are diameter and chirality dependent.

For a CNT with N hexagons per unit cell, there are 2 carbon atoms per hexagon and 3 vibrational degrees of freedom per atom, yielding $6N$ total degrees of freedom per the unit cell. For zigzag and armchair CNTs, $N = 2n$, while for chiral CNTs

$$N = \frac{2(m^2 + n^2 + nm)}{d_R}$$

, where d_R is the greatest common divisor of $(2n + m, 2m + n)$ and is given by

$$d_R = \begin{cases} d & \text{if } n - m \text{ is not a multiple of } 3d \\ 3d & \text{if } n - m \text{ is a multiple of } 3d \end{cases}$$

.

For all symmetry types, CNTs have 4 modes for which the frequency vanishes ($\omega \to 0$) as the wave vector approaches the zone center ($k \to 0$). These modes include rigid rotation around the cylindrical axis and has A_{2g} (A) symmetry; rigid translation mode along the axis and has A_{2u}(A) symmetry; rigid translations along the directions perpendicular to the axis and have E_{1u} (E_1) symmetry (two-fold degenerate).

To be more specific, for (n, n) armchair CNTs with an even n, the vibrational modes are decomposed according to the point group D_{nh}. Armchair CNTs with an odd n in the circumferential direction have D_{nd} symmetry. Zigzag $(n, 0)$ CNTs with an odd n also fall into the D_{nd} point group while when n is even, they fall into D_{nh} point group. For both armchair and zigzag CNTs, the translations are decoupled from the rotations, so that they can be described by symmorphic groups. Chiral CNTs (n, m) are more complicated since the basic symmetry operations involve both rotations and translations. They can be described by a nonsymmorphic space group C_j, where $j = (N/2 - 1)$. The irreducible representations A_{2g}, A_{2u} and E_{1u} are relevant to the groups D_{nh} and D_{nd}, while A and E_1 are relevant to group C_j.

The number of vibrational modes increases as the diameter of CNT increases. However the number of Raman-active and infrared-active modes remain constant for each symmetry type. The Raman-active modes transform from A_{1g}, E_{1g}, or E_{2g} for D_{nh} and D_{ng} groups, and from A, E_1 and E_2 for C_j group. Similarly, IR-active modes transform from A_{2u} or E_{1u} for D_{nh} and D_{nd} groups, and from A and E_1 for C_j group. More details can be found in Table 2.1.

Some of the vibrational modes frequencies and Raman cross sections are sensitive to the CNT diameter. Significantly, the radial breathing mode (RBM), A_{1g} is a convenient tool for CNT diameter estimation. The RBM frequency does not depend on the CNT chirality since all the atoms move in phase for

Table 2.1: Symmetries of Raman-active and IR-active modes for CNTs [63]

CNTs	point group	Raman-active modes	IR-active modes
armchair (n,n) with even n	D_{nh}	$4A_{1g} + 4E_{1g} + 8E_{2g}$	$A_{2u} + 7E_{1u}$
armchair (n,n) with odd n	D_{nd}	$3A_{1g} + 6E_{1g} + 6E_{2g}$	$2A_{2u} + 5E_{1u}$
zigzag $(n,0)$ with even n	D_{nh}	$3A_{1g} + 6E_{1g} + 6E_{2g}$	$2A_{2u} + 5E_{1u}$
zigzag $(n,0)$ with odd n	D_{nd}	$3A_{1g} + 6E_{1g} + 6E_{2g}$	$2A_{2u} + 5E_{1u}$
chiral (n,m) with $n \neq m \neq 0$	C_N	$4A + 5E_1 + 6E_2$	$4A + 5E_1$

the radial breathing mode. Raman spectroscopy of the RBMs has been widely used to provide information on CNT diameter distribution, which is a critical parameter for mass transport studies in CNTs.

2.8 Water transport in CNTs

The macroscopic laws of hydrodynamics, given by the Hagen–Poiseuille equation, govern the flow in conventional fluidic channels. From the very first simulations that predicted fast flow in carbon nanotubes it was clear that the conventional fluid flow description would not be applicable anymore [65, 66]. What are the physical reasons behind this discrepancy? Further simulations provided some valuable clues. A pioneering work from the Aluru group indicated that continuum flow theory was valid for CNT with 10 nm diameter, but broke down in 0.95 nm nanotubes [67]. Clearly, one of the reasons why conventional hydrodynamics breaks down in the smallest CNT pores with diameters below 1 nm is that those pore sizes squeeze water molecules down into a single-file configuration with the hydrogen bonding pattern drastically different from conventional bulk water arrangement [65, 68]. Smooth hydrophobic surface of carbon nanotubes enable inherently low friction at the interface, which is conventionally described as very large slip length [69, 70] (the slip length is defined as the depth inside a solid surface where the extrapolated fluidic velocity profile goes to zero). A conventional version of the Hagen-Poiseuille equation assumes a no-slip condition at the interface (i.e. a zero value of the slip length). In the extreme case of a very large slip length compared to the channel diameter, which corresponds to a nearly frictionless surface, the boundary can be considered virtually shear-free, making the Hagen-Poiseuille equation invalid. A simulation by the Aluru group (Figure 2.2) demonstrated some of the effects the nature of the channel surface enacts on the flow inside a nanotube. Of the three nanotubes with similar diameter, a CNT had the highest water velocity and the highest flux, compared to boron

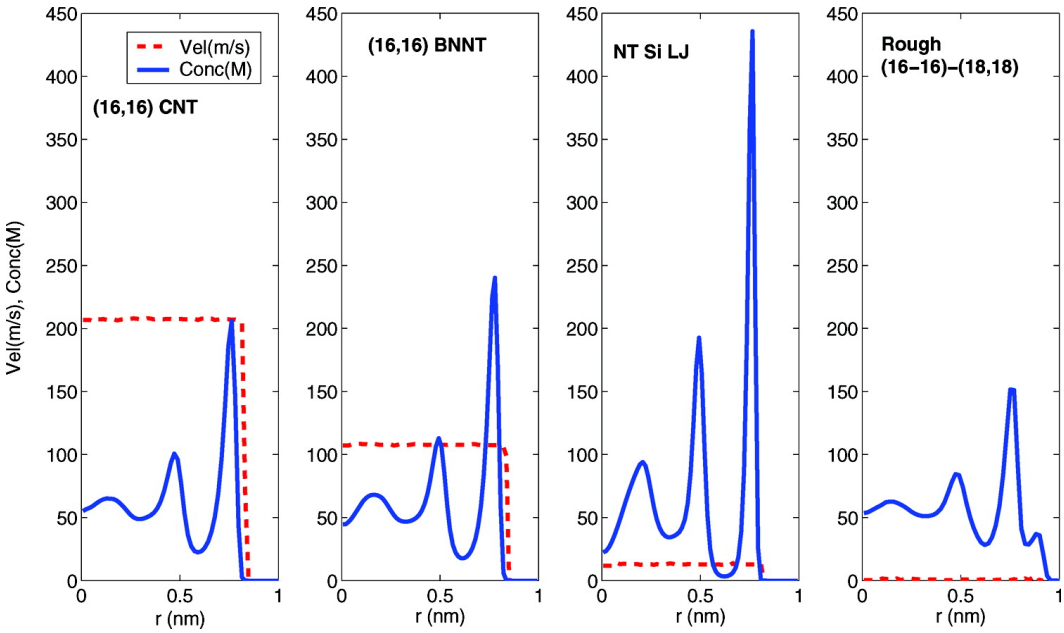

Figure 2.2: MD simulation of water velocity (red dash line) and water density (blue line) profiles as a function of the radius from the center of a (16, 16) CNT, (16, 16) BNNT, (16, 16) nanotube with silicon, and a rough surface (16, 16)/(18, 18) CNT combination. (Reproduced with permission from [64]. © *2008 American Chemical Society*)

nitride tube (BNNT), hydrophilic silicon nanotube (NT Si), and a hypothetical CNT with computationally-engineered rough surface [64]. Consequently, the flux enhancement for the other nanotubes considered in that study was significantly reduced. The study concluded that the origin of the remarkable flux enhancement in CNTs was a combination of the smoothness of the CNT surface and its hydrophobicity that reduced water molecule interactions with the tube surface.

The first experimental demonstrations of high water flux enhancement in CNT pores were reported shortly after the publication of the first computational predictions. Hinds group first demonstrated high rates of water transport through aligned MWNT membranes with 7 nm in diameter and reported remarkably long slip lengths [69] that indicated more than four orders of magnitude increase in water permeability compared with the Hagen-Poiseuille equation predictions. When they tested the flow of a variety of solvents, including hexane and ethanol, through MWNT membranes, the permeability decreased as the solvents became more hydrophobic. These findings emphasized again that it is not only the smoothness of the CNT surface but also its hydrophobic

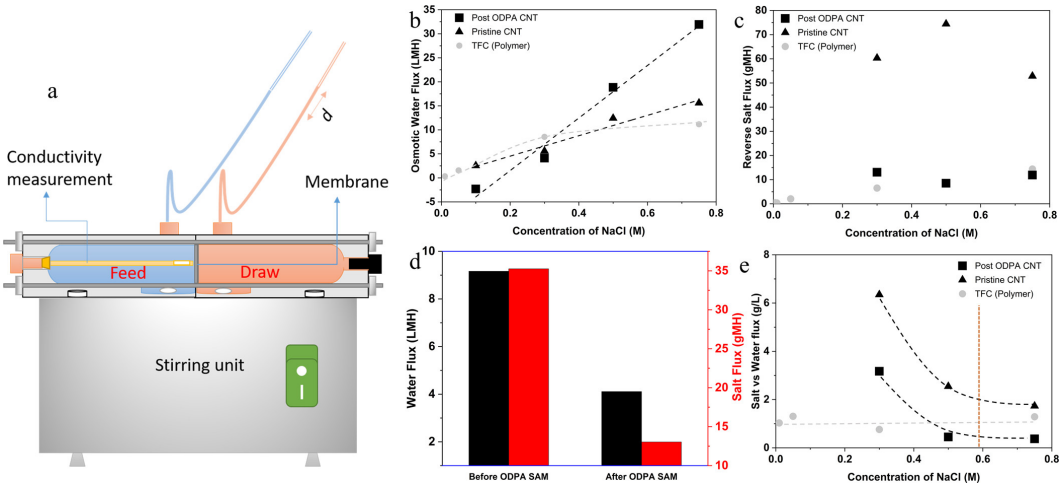

Figure 2.3: Osmotic water and salt transport across CNT/titanium dioxide membranes in forward osmosis (FO) setup. (a) Sketch of the FO diffusion cell to monitor osmotic water transfer using meniscus capillaries and salt transport using conductivity electrodes. (b, c, and d) Water flux and reverse salt flux through the membrane compared with commercial available polymer membranes and further modified CNT membranes. (e) Membrane performance comparison at different salt conditions. (Reproduced with permission from [71]. © *2018 American Chemical Society*)

nature that is responsible for high water velocity. Bakajin, Noy and coworkers also reported water fluxes in aligned sub-2-nm DWNT membranes under pressure-driven flow conditions that exceeded values calculated from continuum hydrodynamics models by more than three orders of magnitude [72]. Later on, Park group demonstrated osmotic water and salt transport across their CNT membranes in forward osmosis (FO) setup again reporting with high water fluxes (Figure 2.3) [71].

Measurements of water filling and flow in individual CNT pores revealed an even more complicated physical picture. Strano group measurements showed evidence of phase transitions between ice, liquid water, and gas phase water in CNTs at near room temperatures [73], providing an experimental evidence of water behavior that was previously predicted in MD simulations [74]. Bocquet group performed a scientific tour-de-force experiment where they were able to use their "nanojet" platform to observe exceptionally high water transport rates in single CNTs directly [70]. Remarkably, these measurements showed that the values of the slip length became divergent as the size of the carbon nanotubes became smaller and started to approach the "single-digit" nanopore regime (i.e. $d < 10$ nm). In contrast, boron nitride nanotubes (BNNTs) of

similar diameters showed very small values of slip length (Figure 2.4). Compared to CNTs, BNNTs have a similarly smooth, but much higher charged, surface, which interacts with water molecules quire strongly and slows down the water flow through the tube significantly.

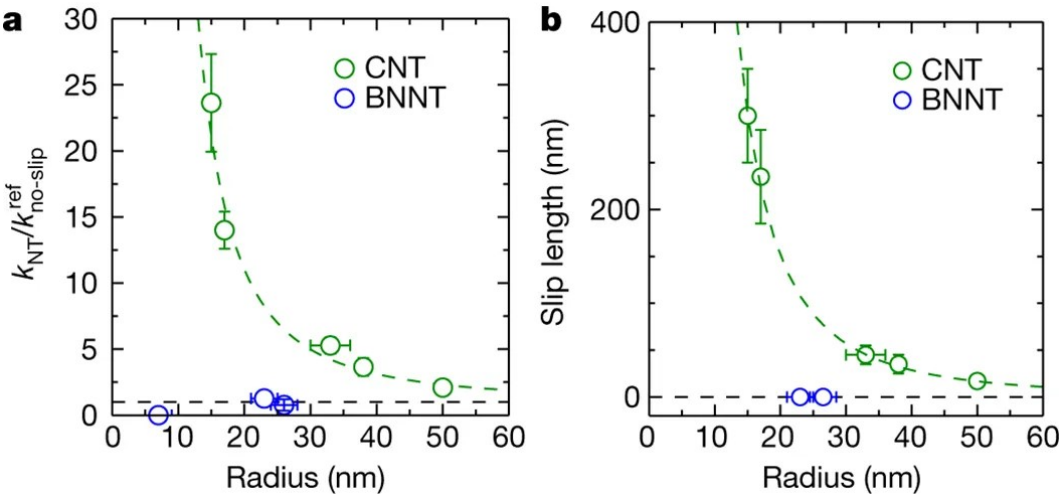

Figure 2.4: Water permeability and slip length of individual CNTs and BNNTs derived from the nanojet measurements. (a) Normalized permeability and (b) slip length of tubes as a function of nanotube radius. The horizontal dash lines indicate the no-slip prediction. (Reproduced with permission from [70]. © *2016 Nature Publishing Group*)

Another interesting comparison could be made with the water transport in aquaporins, which are biological membrane channels responsible for water transport. Very narrow (ca. 3Å) AQP channels, which are lined mostly with hydrophobic residues, enable extremely fast water transport and are considered the gold standard of membrane water channels. The Noy group compared water transport in two types of CNTPs with diameters of 0.8 and 1.5 nm with water transport in aquaporins [68]. While the 1.5 nm diameter CNTP showed bulk water-like transport with the fluxes significantly lower that of the AQP1 protein channels, the 0.8 nm diameter CNTP showed enhanced water flow rates that exceeded even those of AQP-1 (Figure 2.5). This remarkably strong performance was again attributed to a combination of several factors. Narrow diameter CNTPs benefit from the same physical phenomena that enhance water transport in wider CNTPs: the smoothness of the tube walls and their hydrophobic character. However, in addition to these factors, 0.8 nm CNTPs force water into a single-file configuration where a chain-like hydrogen bonding pattern leads to a further water transport efficiency enhancement.

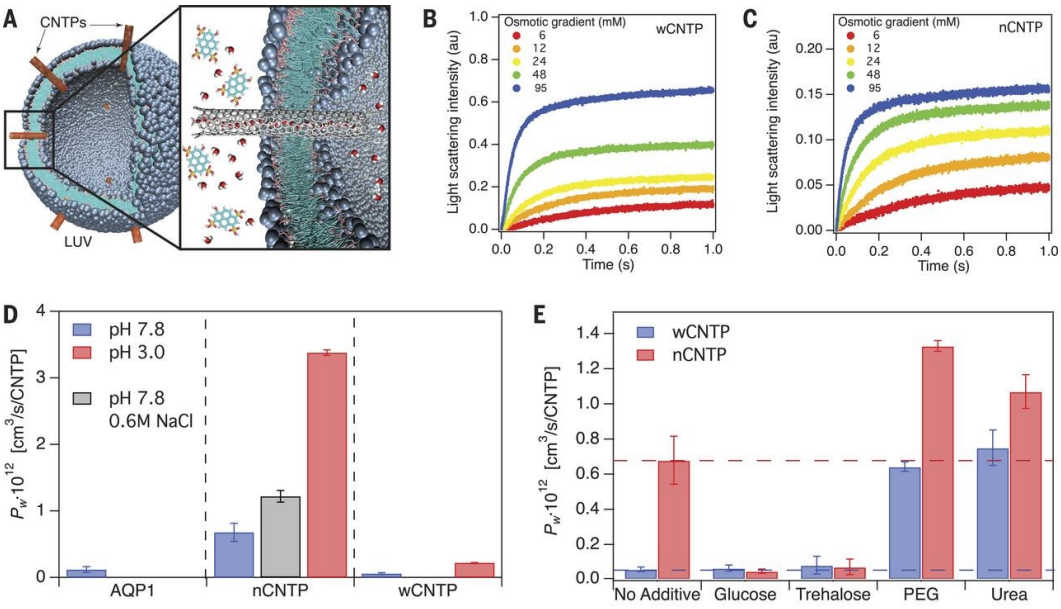

Figure 2.5: Water transport through 0.8 nm and 1.5 nm diameter CNTPs. (A) Sketch of CNTP in the lipid vesicle platform for water flux measurements under osmotic pressure. (B, C) Light scattering traces for lipid vesicle with CNTPs under various osmotic gradients. (D) Water permeability for 0.8 nm and 1.5 nm diameter CNTPs at pH 7.5 and pH 3.0, compared with AQP-1. (E) Water permeability changes with additives, which change water structure of water. (Reproduced with permission from [68]. © *2017 American Association for the Advancement of Science*).

2.9 Ion transport in CNTs

High water permeability makes carbon nanotubes an attractive materials platform for water treatment applications; however, the other, and arguably more important [76], property is ion selectivity and ion rejection. A number of physical mechanisms determine ion selectivity in membrane nanopores: size exclusion at the pore mouth, partial solute dehydration upon entry into the pore, and electrostatic exclusion due to the charges present at the pore mouth or along the pore surface (Figure 2.6). Constant diameter of the CNT pores makes their size exclusion properties fairly straightforward. Holt et. al. demonstrated sub-2-nm aligned double-wall carbon nanotube membranes excluded 2 nm gold colloids [72]. However, the diameters of carbon nanotubes are *a priori* still too large to make the pore exclude all ions based simply on their ionic radii. The situation becomes very different when we consider the

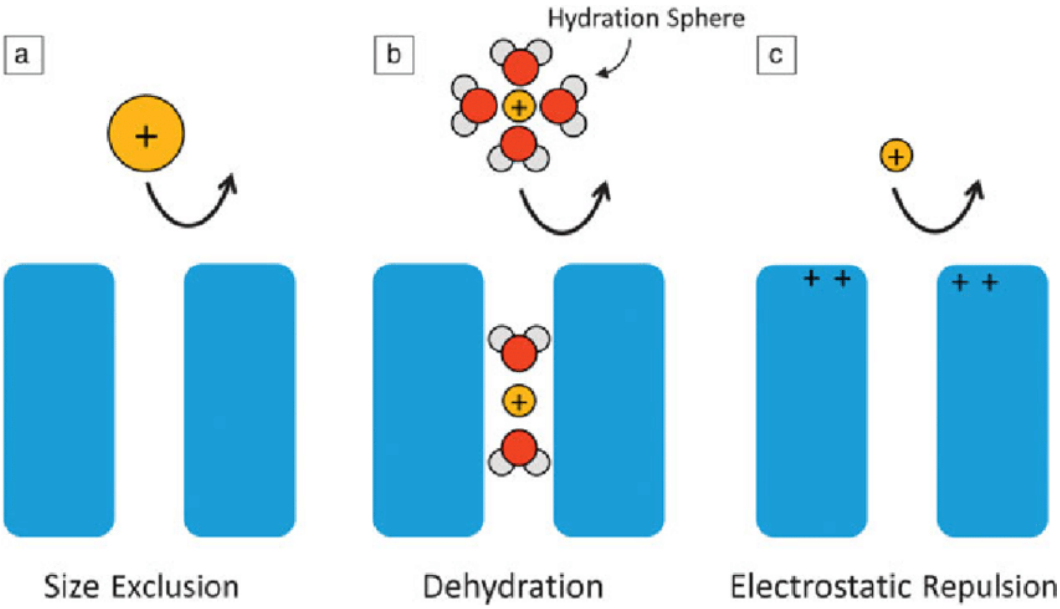

Figure 2.6: Mechanisms of ion selectivity and rejection for a nano channel, including (a) size exclusion, (b) dehydration barriers, and (c) electrostatic interactions. (Reproduced with permission from [75]. © *2017 Materials Research Society*)

hydrated radii of the ions, making the energy costs associated with the partial ion dehydration upon entry into the carbon nanotube pore another powerful mechanism for ion selectivity [77]. Electrostatic repulsion is potentially another powerful mechanism for conveying selectivity to the CNT pores. Generally, the range and the impact of the electrostatic effects is highly dependent on the electrostatic screening due to the presence of mobile charges in solution, which is described by the Debye length. Specifically, when the Debye length of the electrolyte is larger than the radius of the nanopore with charged ends or walls, the electric fields overlap and create a barrier for the ion passage. As the ion concentration increases and the Debye length drops, the electric fields contract and create an opening through which ions can pass. As the Debye length at seawater conditions is rather small, ca. 3 Å, we do not expect that pure electrostatic repulsion could represent the dominant rejection mechanism for these types of water feeds. Indeed, the effect of decreasing ion selectivity at higher ion concentration was observed experimentally for both aligned carbon nanotube membranes and carbon nanotube porin experimental platforms [68, 78].

The first observation of ion transport in CNT pores was reported by Hinds

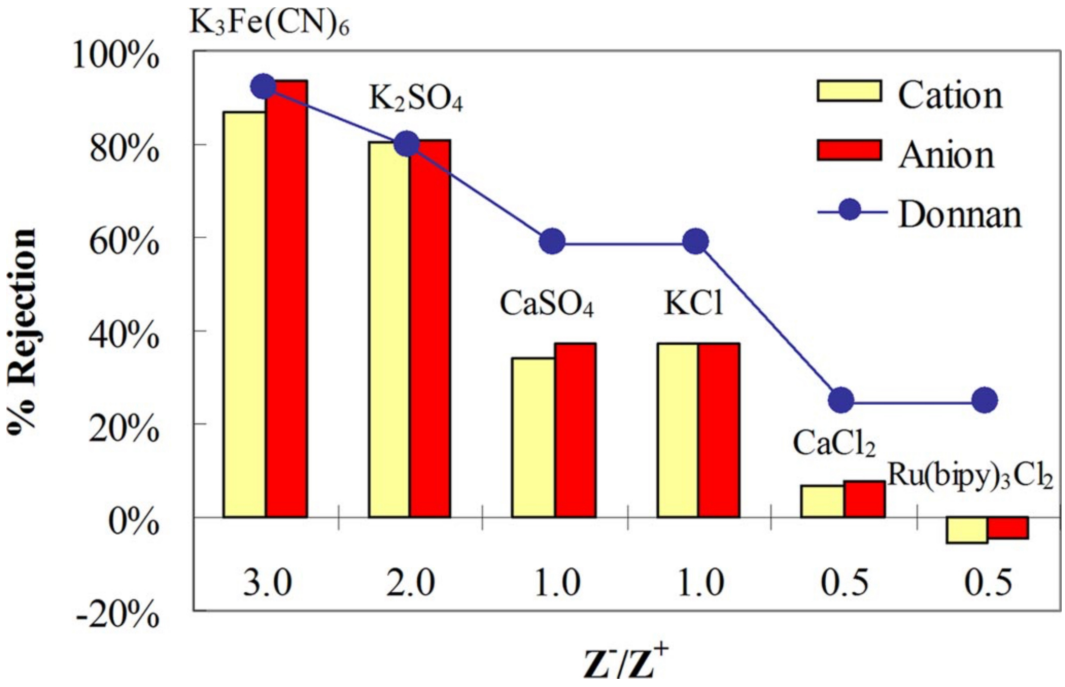

Figure 2.7: Rejection coefficients (bars) measured for six salt solutions that have the same equivalent concentration but different ion valence. Points (filled circles) indicate rejections calculated from the Donnan model. The calculation assumed charge density corresponding to approximately seven charged groups per nanotube. (Reproduced with permission from [78]. © *2008 The National Academy of Sciences of the USA*).

and co-workers in their seminal paper on aligned nanotube membranes [79], where they observed diffusion of $Ru(NH_3)_6^{3+}$ ions across the membrane. The same work demonstrated the possibility of using size exclusion/steric hindrance mechanism for modulating $Ru(NH_3)_6^{3+}$ ion flux by functionalizing the CNT pore entrances with biotin and subsequently attaching a bulky streptavidin molecule to the biotin [79]. Bakajin, Noy and co-workers studied transport of a variety of ionic compounds in smaller (1.6 nm) diameter aligned DWCNT membranes using pressure-driven reverse osmosis experiments and observed that salt rejection in these pore ranged from nearly 100% for $K_3Fe(CN)_6$ to very low for $CaCl_2$ [78]. The degree of rejection was also a strong function of the overall ionic strength of the solution, with KCl rejection ranging from 50% at low ion concentration to near zero at high concentration. These results provided a very strong evidence that the Donnan electrostatic exclusion was the dominant mechanism for the ion selectivity in CNT pores of this size.

Subsequent work by the same group traced the origin of this selectivity to the presence of charged COO^- groups at the rim of the carbon nanotube pores [80]. Interestingly, Marand group reported that membranes with CNTs functionalized with chain-like zwitterion molecules rejected essentially all ions, giving 98.6% of rejection rate on NaCl [81]. The researchers speculated that these bulky functional groups promoted size exclusion and provided multiple charges to enhance electrostatic repulsion.

Observations of ion transport in individual CNT channels took comparatively longer, with the first reports appearing only by 2010 [82, 83]. Both of these two studies that pioneered this sub-field used ultra-long CNTs incorporated into a microfluidic device platform. First, Lindsay and coworkers reported large electrophoretic current through single SWCNTs, where the measured current exceeded the value calculated from the CNT diameter and KCl bulk solution conductivity [82]. This enhancement was interpreted as another evidence for the friction-less transport inside CNT pores. Interestingly, this work noted that metallic CNTs exhibited larger ion current. Strano and coworkers investigated similar devices and reached a radically-different conclusion; they observed that the current through their devices that had ca. 1.5 nm diameter and 500 μm long CNT was largely protonic [83]. Moreover, this group observed that alkali metal ions could act as current blockers and create regular current oscillation [83]. A further systematic study of various CNTs with diameters that ranged from 0.94 nm to 2.01 nm showed varied dwell times and blocking currents, in which CNT diameter around 1.58 nm displayed the largest blocking current [84].

More recently a number of measurements reported ion and proton transport in individual CNT channels with length ranging from several micrometers [85] to ultra-short (10 nm) CNTPs [68, 86]. A study from the Noy group reported ultra-fast proton transport in 0.8 nm diameter CNTPs due to the single-file water arrangement inside that channel promoting proton transport via the Grotthuss hopping mechanism [86], confirming earlier MD simulations predictions [87]. Results from the Bocquet group showed intriguing CNT conductance dependence on salt concentration [85] when they examined KCl transport in CNT with 7 nm, 20 nm, 28 nm, and 70 nm diameters. All CNTs showed power law conductance scaling that transitioned from around linear at high salt concentration to 1/3 power law at low salt (Figure 2.8). The explanation advanced by Bocquet *et. al.* relied on an elegant model that assumed that the CNT inner surface carried some negative charge due to adsorption of the OH^- groups. This adsorption process, in turn, was subject to charge regulation at varying ionic strengths, with a combination of this charge regulation and preferential accumulation of the counterions inside the channel producing the observed 1/3 power law scaling of the ion conductance. Some of the main problems with this approach were that there was no direct evidence

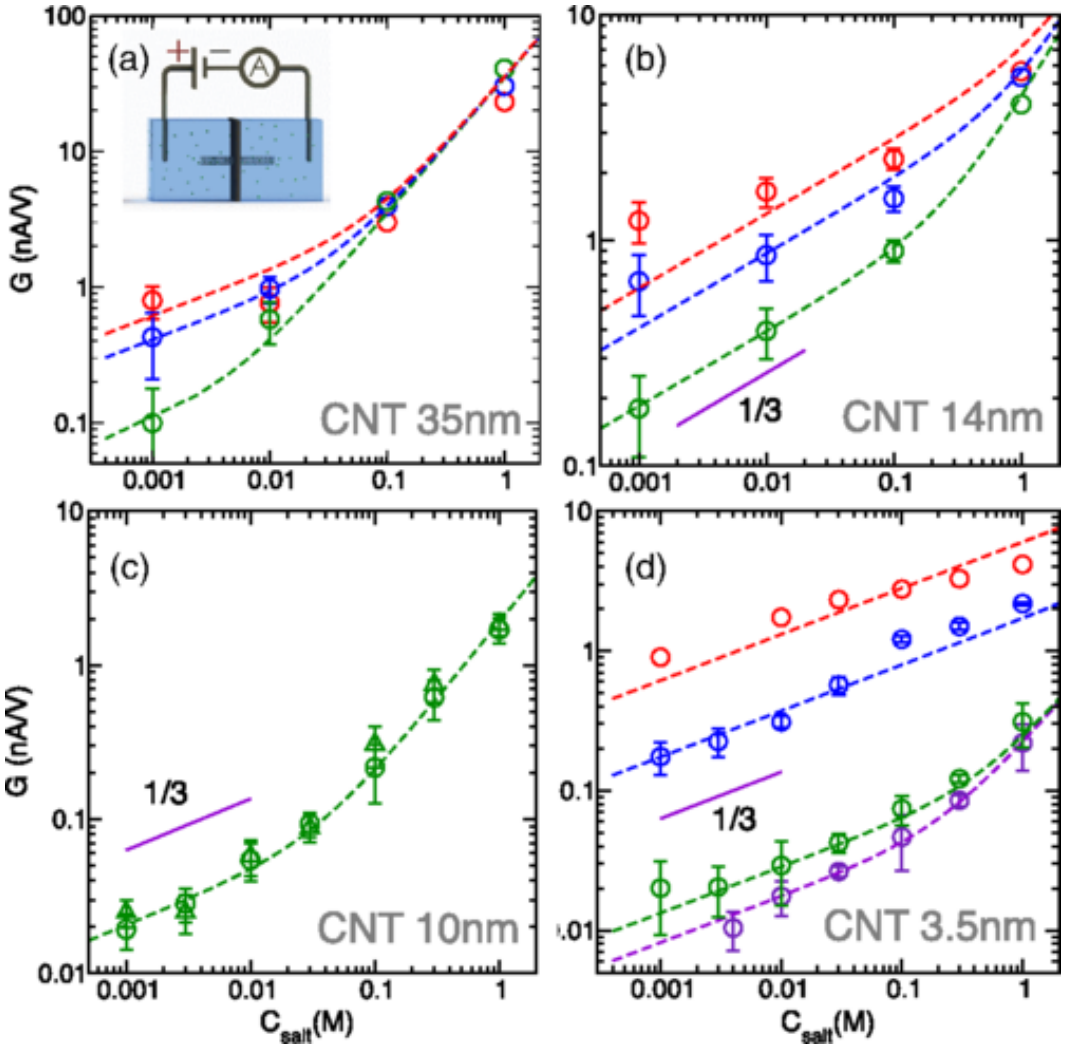

Figure 2.8: Conductance (G) scaling with a range of electrolyte concentrations measured through single CNTs with various diameters from 70 nm to 7 nm and pH from 10 to 4. (Reproduced with permission from [85]. ©*2016 American Physical Society*).

for the OH^- ions adsorption on the CNT surfaces and that such adsorption could potentially interfere with the fast transport and high water flux in the CNT pores.

The 1/3 power law behavior turns out not to be a universal scaling law in CNT pores. Nuckolls group reported non-linear concentration scaling for ion transport in 1.5 nm diameter CNT pores which followed 1/2 power law [88]. That team attributed the observed effects to the charge regulation of the COO^- groups at the pore entrances. Noy group reported an even richer set of behaviors in CNT porins of different diameters. For the ultra-narrow, 0.8 nm diameter CNTPs, the ion conductance initially followed the 1/2 exponent power law and then saturated at higher ionic strengths [68], mimicking the behavior of small diameter biological ion channels [89]. Ion conductance in larger diameter, 1.5 nm, CNTPs displayed yet another pattern of behavior, showing 2/3 power law and no saturation at high ion concentrations [90].

Extensive modeling efforts by several groups have clarified some of the origins of these reach set of scaling behaviors. Biesheuvel and Bazant presented an extensive analysis that showed how a solution to the Poisson-Nernst-Planck equations in combination with charge regulation can describe some of the scaling laws observed in the experiments [91], pointing out that in particular the 1/2 power law could be the evidence of the conductance following the "good co-ion exclusion" limit where the nanotube pore becomes exclusively selective to one kind of ions. Manghi and coworkers added another layer of complexity to the model by accounting for the possibility of strong fluid slip along the nanotube pore walls [92]. This interpretation in combination with the extensive modeling helped Noy, Aluru and coworkers to rationalize their observation of the 2/3 power law scaling in larger diameter CNT pores and attribute it to extremely strong electroosmotic coupling in these channels.

Strano group, Nuckolls group and Noy group all reported that CNT pores with negatively charged COO^- groups at the ends showed preferential cation selectivity. Nuckolls group compared the transport of KCl and $K_3Fe(CN)_6$) in 1.5 nm diameter CNTs and reported negligible effect on ion transport; however, when they replaced potassium with a bigger cation, tris(bipyridine)ruthenium(II), $[Ru(bpy)_3]^{2+}$, they observed significant reduction of conductance, which they attributed to the increased ion rejection of the larger cation at the nanotube entrance [88]. Noy group performed extensive characterization of ion selectivity in CNTPs using reversal potential measurements in single CNTP conductance experiments [68]. In these experiments CNTPs with 0.8 nm diameter showed near-perfect cation selectivity which started to roll off only at very high ionic strength above the seawater levels (Figure 2.9). This observation is remarkable as it indicates that at small enough diameters CNTPs exhibit monovalent salt rejection that is sufficient enough for seawater desalination. Not surprisingly, larger 1.5 nm diameter CNTPs do not have the same degree

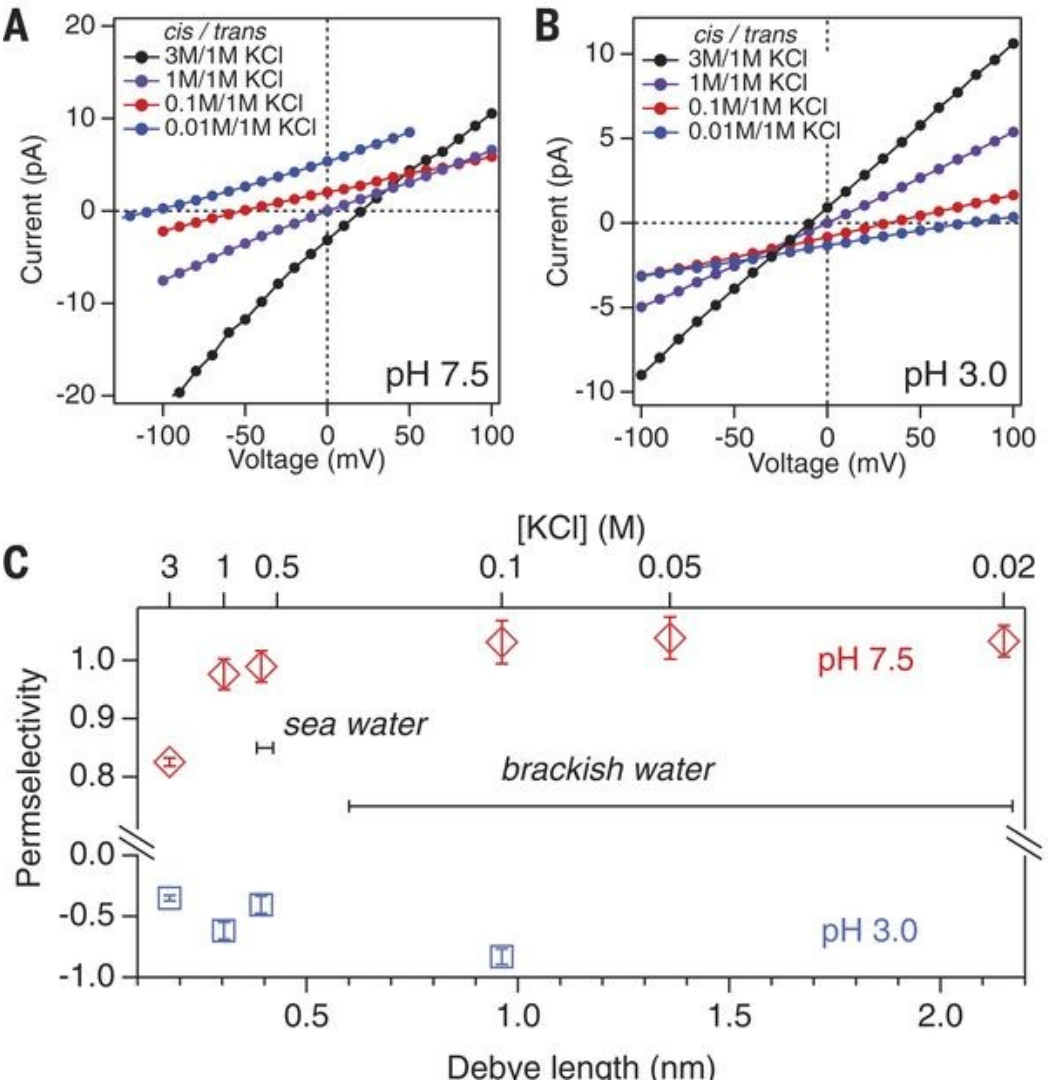

Figure 2.9: Ion selectivity between cation and anion in 0.8 nm diameter CNTPs. (A and B) Reversal potential measurements showing asymmetric I-V curves at pH 7.5 and pH 3.0. (C) Permselectivity values plotted as a function of the Debye length for higher concentration KCl electrolytes. (Reproduced with permission from [68]. © *2017 American Association for the Advancement of Science*).

of ion selectivity and instead have much weaker cation selectivity with the permselectivity of around 0.5 [90]. When the COO^- groups at the ends were neutralized by changing the pH to 3, CNTPs became even less selective, with their permselectivity dropping down to zero.

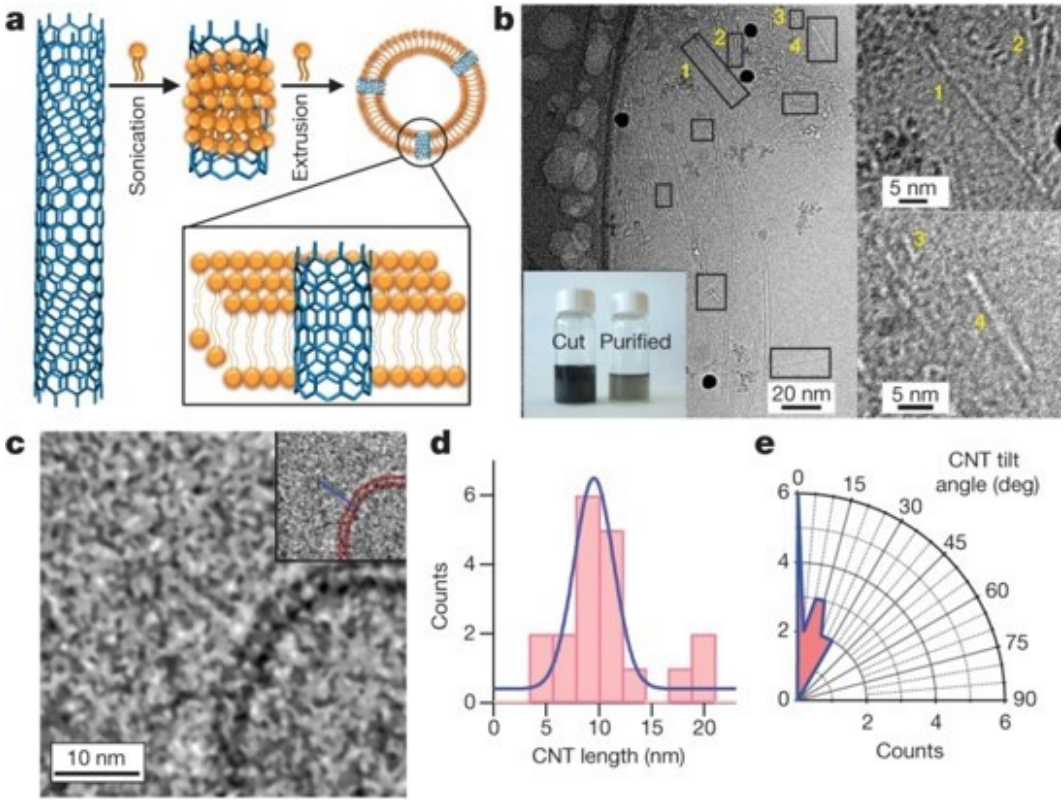

Figure 2.10: Synthesis and characterization of carbon nanotube porins (CNTPs). (a) Schematic of CNTP preparation and incorporation into lipid bilayer membranes. (b) TEM image of CNTPs. (c) Cryo-EM images of a CNTP inserted in a lipid vesicle. (d) Histogram of CNT length and angle distribution when inserted into the lipid membranes. (Reproduced with permission from [93]. © *2014 Nature Publishing Group*).

Overall, despite the significant progress reported in elucidating ion selectivity in CNTs our understanding of the ion rejection mechanisms in these nanochannels remains incomplete. For example, experimental data on CNTP conductance show linear I-V curves even for the smallest 0.8 nm pores, indicating that the barrier for entry into these tubes for at least the majority carrier species is quite low [68]. This observation directly contradicts the results of classical MD simulations that show that ion entry into a small diameter CNT

pore requires costly partial dehydration of the ion solvation shell [94]. An even more complicated questions include whether such partial desolvation and strong degree of confinement induce any unusual differential selectivity effects, correlated transport effects. Finally, we still do not have a good understanding of what the concentration polarization effects would look like in these pores.

2.10 Biomimetic carbon nanotube porin membrane pores

Noy group comes up with a different strategy to measure water and ion transport in CNT channels. Their platform, carbon nanotube porins (CNTPs), emulated membrane channels, with ultrashort CNTs 10-20 nm in length embedded in lipid or polymer membranes (Figure 2.10) [93, 95]. To fabricate CNTPs, commercially available, long CNTs were cut by tip-sonication into much shorter pieces [96]. Significantly, this procedure allowed to use CNT stocks of different diameter, producing CNTPs of different size. Specifically, the team made CNTPs with 0.8 and 1.5 nm diameter, allowing direct comparison of transport efficiency between channels with the same geometry but different pore sizes. Another key advantage of this biomimetic platform was that it allowed direct adoption of a number of protocols that were developed for measuring water and ion transport in biological membrane channels, including lipid vesicle and planar lipid bilayer platforms [68, 86].

References

(1) Iijima, S. *nature* **1991**, *354*, 56.

(2) Iijima, S.; Ichihashi, T. *nature* **1993**, *363*, 603.

(3) Bethune, D.; Kiang, C. H.; De Vries, M.; Gorman, G.; Savoy, R.; Vazquez, J.; Beyers, R. *Nature* **1993**, *363*, 605.

(4) Terrones, M. *Annual review of materials research* **2003**, *33*, 419–501.

(5) Thess, A.; Lee, R.; Nikolaev, P.; Dai, H.; Petit, P.; Robert, J.; Xu, C.; Lee, Y. H.; Kim, S. G.; Rinzler, A. G., et al. *Science* **1996**, *273*, 483–487.

(6) Journet, C.; Maser, W.; Bernier, P.; Loiseau, A.; de La Chapelle, M. L.; Lefrant, d. S.; Deniard, P.; Lee, R.; Fischer, J. *Nature* **1997**, *388*, 756.

(7) Dresselhaus, M. S.; Dresselhaus, G.; Eklund, P. C., *Science of fullerenes and carbon nanotubes: their properties and applications*; Elsevier: 1996.

(8) Dresselhaus, M. S.; Dresselhaus, G.; Avouris, P. *Topics in applied physics* **2001**, *80*, 113–146.

(9) Dekker, C. et al. *Physics today* **1999**, *52*, 22–30.

(10) McEuen, P. L. *Physics World* **2000**, *13*, 31.

(11) Dai, H. *Physics World* **2000**, *13*, 43.

(12) Dai, H. In *Carbon Nanotubes*; Springer: 2001, pp 29–53.

(13) Liang, W.; Bockrath, M.; Bozovic, D.; Hafner, J. H.; Tinkham, M.; Park, H. *Nature* **2001**, *411*, 665.

(14) Kong, J.; Yenilmez, E.; Tombler, T. W.; Kim, W.; Dai, H.; Laughlin, R. B.; Liu, L.; Jayanthi, C.; Wu, S. *Physical review letters* **2001**, *87*, 106801.

(15) Dresselhaus, M.; Dresselhaus, G.; Saito, R. *Physical Review B* **1992**, *45*, 6234.

(16) Saito, R.; Fujita, M.; Dresselhaus, G.; Dresselhaus, u. M. *Applied physics letters* **1992**, *60*, 2204–2206.

(17) Ebbesen, T. W. *Annual review of materials science* **1994**, *24*, 235–264.

(18) José-Yacamán, M.; Miki-Yoshida, M.; Rendón, L.; Santiesteban, J. G. *Applied Physics Letters* **1993**, *62*, 657–659.

(19) Cheng, H.; Li, F.; Sun, X.; Brown, S.; Pimenta, M.; Marucci, A.; Dresselhaus, G.; Dresselhaus, M. *Chemical Physics Letters* **1998**, *289*, 602–610.

(20) Kong, J.; Soh, H. T.; Cassell, A. M.; Quate, C. F.; Dai, H. *Nature* **1998**, *395*, 878.

(21) Hafner, J. H.; Bronikowski, M. J.; Azamian, B. R.; Nikolaev, P.; Rinzler, A. G.; Colbert, D. T.; Smith, K. A.; Smalley, R. E. *Chemical Physics Letters* **1998**, *296*, 195–202.

(22) Satishkumar, B.; Govindaraj, A.; Sen, R.; Rao, C. *Chemical Physics Letters* **1998**, *293*, 47–52.

(23) Nikolaev, P.; Bronikowski, M. J.; Bradley, R. K.; Rohmund, F.; Colbert, D. T.; Smith, K.; Smalley, R. E. *Chemical physics letters* **1999**, *313*, 91–97.

(24) Su, M.; Zheng, B.; Liu, J. *Chemical Physics Letters* **2000**, *322*, 321–326.

(25) Colomer, J.-F.; Stephan, C.; Lefrant, S.; Van Tendeloo, G.; Willems, I.; Konya, Z.; Fonseca, A.; Laurent, C.; Nagy, J. B. *Chemical Physics Letters* **2000**, *317*, 83–89.

(26) Kasuya, A.; Sasaki, Y.; Saito, Y.; Tohji, K.; Nishina, Y. *Physical Review Letters* **1997**, *78*, 4434.

(27) Dai, H. *Accounts of chemical research* **2002**, *35*, 1035–1044.

(28) Yamada, T.; Namai, T.; Hata, K.; Futaba, D. N.; Mizuno, K.; Fan, J.; Yudasaka, M.; Yumura, M.; Iijima, S. *Nature nanotechnology* **2006**, *1*, 131.

(29) Dresselhaus, M. S.; Dresselhaus, G.; Eklund, P.; Rao, A. In *The physics of fullerene-based and fullerene-related materials*; Springer: 2000, pp 331–379.

(30) Endo, M.; Takeuchi, K.; Igarashi, S.; Kobori, K.; Shiraishi, M.; Kroto, H. W. *Journal of Physics and Chemistry of Solids* **1993**, *54*, 1841–1848.

(31) Tersoff, J.; Ruoff, R. *Physical Review Letters* **1994**, *73*, 676.

(32) Mintmire, J.; White, C. *Carbon* **1995**, *33*, 893–902.

(33) Yakobson, B. I.; Brabec, C.; Bernholc, J. *Physical review letters* **1996**, *76*, 2511.

(34) Treacy, M. J.; Ebbesen, T.; Gibson, J. *nature* **1996**, *381*, 678.

(35) Lourie, O.; Wagner, H. *Journal of Materials Research* **1998**, *13*, 2418–2422.

(36) Schadler, L.; Giannaris, S.; Ajayan, P. *Applied physics letters* **1998**, *73*, 3842–3844.

(37) Saito, R.; Dresselhaus, G.; Dresselhaus, M. *Chemical physics letters* **1992**, *195*, 537–542.

(38) Mintmire, J. W.; Dunlap, B.; White, C. *Physical review letters* **1992**, *68*, 631.

(39) Hamada, T.; Furuyama, M.; Tomioka, T.; Endo, M. *Journal of materials research* **1992**, *7*, 1178–1188.

(40) Harigaya, K. *Chemical physics letters* **1992**, *189*, 79–83.

(41) Tanaka, K.; Okahara, K.; Okada, M.; Yamabe, T. *Chemical Physics Letters* **1992**, *191*, 469–472.

(42) Saito, R.; Dresselhaus, G.; Dresselhaus, M. S., *Physical Properties of Carbon Nanotubes*; PUBLISHED BY IMPERIAL COLLEGE PRESS and DISTRIBUTED BY WORLD SCIENTIFIC PUBLISHING CO.: 1998.

(43) Wilder, J. W.; Venema, L. C.; Rinzler, A. G.; Smalley, R. E.; Dekker, C. *Nature* **1998**, *391*, 59.

(44) Sattler, K. *Carbon* **1995**, *33*, 915–920.

(45) Kong, J.; Franklin, N. R.; Zhou, C.; Chapline, M. G.; Peng, S.; Cho, K.; Dai, H. *Science* **2000**, *287*, 622–625.

(46) Collins, P. G.; Bradley, K.; Ishigami, M.; Zettl, A. *Science* **2000**, *287*, 1801–1804.

(47) Sumanasekera, G. U.; Adu, C. K. W.; Fang, S.; Eklund, P. C. *Phys. Rev. Lett.* **2000**, *85*, 1096–1099.

(48) Chen, R. J.; Franklin, N. R.; Kong, J.; Cao, J.; Tombler, T. W.; Zhang, Y.; Dai, H. *Applied Physics Letters* **2001**, *79*, 2258–2260.

(49) Zhou, C.; Kong, J.; Dai, H. *Phys. Rev. Lett.* **2000**, *84*, 5604–5607.

(50) Hamada, N.; Sawada, S.-i.; Oshiyama, A. *Phys. Rev. Lett.* **1992**, *68*, 1579–1581.

(51) Blase, X.; Benedict, L. X.; Shirley, E. L.; Louie, S. G. *Phys. Rev. Lett.* **1994**, *72*, 1878–1881.

(52) Dresselhaus, M.; Dresselhaus, G.; Eklund, P.; Saito, R. *Physics World* **1998**, *11*, 33–38.

(53) Kouwenhoven, L. *Science* **1997**, *275*, 1896–1897.

(54) Tans, S. J.; Verschueren, A. R.; Dekker, C. *Nature* **1998**, *393*, 49.

(55) Bockrath, M.; Cobden, D. H.; McEuen, P. L.; Chopra, N. G.; Zettl, A.; Thess, A.; Smalley, R. E. *Science* **1997**, *275*, 1922–1925.

(56) Tans, S. J.; Devoret, M. H.; Dai, H.; Thess, A.; Smalley, R. E.; Geerligs, L.; Dekker, C. *Nature* **1997**, *386*, 474.

(57) Tans, S. J.; Devoret, M. H.; Groeneveld, R. J.; Dekker, C. *Nature* **1998**, *394*, 761.

(58) Kaiser, A. B.; Düsberg, G.; Roth, S. *Phys. Rev. B* **1998**, *57*, 1418–1421.

(59) Hone, J.; Ellwood, I.; Muno, M.; Mizel, A.; Cohen, M. L.; Zettl, A.; Rinzler, A. G.; Smalley, R. E. *Phys. Rev. Lett.* **1998**, *80*, 1042–1045.

(60) Jishi, R.; Venkataraman, L.; Dresselhaus, M.; Dresselhaus, G. *Chemical Physics Letters* **1993**, *209*, 77–82.

(61) Richter, E.; Subbaswamy, K. R. *Phys. Rev. Lett.* **1997**, *79*, 2738–2741.

(62) Saito, R.; Takeya, T.; Kimura, T.; Dresselhaus, G.; Dresselhaus, M. S. *Phys. Rev. B* **1998**, *57*, 4145–4153.

(63) Dresselhaus, M.; Dresselhaus, G.; Pimenta, M.; Eklund, P. *Analytical Applications of Raman Spectroscopy* **1999**.

(64) Joseph, S.; Aluru, N. R. *Nano Letters* **2008**, *8*, PMID: 18189436, 452–458.

(65) Hummer, G.; Rasaiah, J. C.; Noworyta, J. P. *Nature* **2001**, *414*, 188–190.

(66) Kalra, A.; Garde, S.; Hummer, G. *Proceedings of the National Academy of Sciences of the United States of America* **2003**, *100*, 10175–80.

(67) Qiao, R.; Aluru, N. R. *The Journal of Chemical Physics* **2003**, *118*, 4692–4701.

(68) Tunuguntla, R. H.; Henley, R. Y.; Yao, Y.-C.; Pham, T. A.; Wanunu, M.; Noy, A. *Science* **2017**, *357*, 792–796.

(69) Majumder, M.; Chopra, N.; Andrews, R.; Hinds, B. *Nature* **2005**, *438*, 44.

(70) Secchi, E.; Marbach, S.; Niguès, A.; Stein, D.; Siria, A.; Bocquet, L. *Nature* **2016**, *537*, 210–213.

(71) Lokesh, M.; Youn, S. K.; Park, H. G. *Nano Letters* **2018**, *18*, PMID: 30339023, 6679–6685.

(72) Holt, J. K.; Park, H. G.; Wang, Y.; Stadermann, M.; Artyukhin, A. B.; Grigoropoulos, C. P.; Noy, A.; Bakajin, O. *Science* **2006**, *312*, 1034–1037.

(73) Agrawal, K. V.; Shimizu, S.; Drahushuk, L.; Kilcoyne, D.; Strano, M. *Nature Nanotechnology* **2016**, *12*, DOI: 10.1038/nnano.2016.254.

(74) Pascal, T. A.; Goddard, W. A.; Jung, Y. *Proc. Natl. Acad. Sci. USA* **2011**, *108*, 11794–11798.

(75) Corry, B. *MRS Bulletin* **2017**, *42*, 306–310.

(76) Werber, J. R.; Deshmukh, A.; Elimelech, M. *Environmental Science & Technology Letters* **2016**, *3*, 112–120.

(77) Song, C.; Corry, B. *The Journal of Physical Chemistry B* **2009**, *113*, PMID: 19419185, 7642–7649.

(78) Fornasiero, F.; Park, H.-G.; Holt, J. K.; Stadermann, M.; Grigoropoulos, C.; Noy, A.; Bakajin, O. *Proc. Natl. Acad. Sci. USA* **2008**, *105*, 17250–17255.

(79) Hinds, B. J.; Chopra, N.; Rantell, T.; Andrews, R.; Gavalas, V.; Bachas, L. G. *Science* **2004**, *303*, 62–65.

(80) Fornasiero, F.; In, J. B.; Kim, S.; Park, H. G.; Wang, Y.; Grigoropoulos, C. P.; Noy, A.; Bakajin, O. *Langmuir* **2010**, *26*, 14848–14853.

(81) Chan, W.-F.; Chen, H.-y.; Surapathi, A.; Taylor, M. G.; Shao, X.; Marand, E.; Johnson, J. K. *ACS Nano* **2013**, *7*, PMID: 23705642, 5308–5319.

(82) Liu, H.; He, J.; Tang, J.; Liu, H.; Pang, P.; Cao, D.; Krstic, P.; Joseph, S.; Lindsay, S.; Nuckolls, C. *Science* **2010**, *327*, 64–67.

(83) Lee, C.; Choi, W.; Han, J.-H.; Strano, M. *Science (New York, N.Y.)* **2010**, *329*, 1320–4.

(84) Choi, W.; Ulissi, Z.; Shimizu, S.; Bellisario, D.; Ellison, M.; Strano, M. *Nature communications* **2013**, *4*, 2397.

(85) Secchi, E.; Niguès, A.; Jubin, L.; Siria, A.; Bocquet, L. *Physical Review Letters* **2016**, *116*, DOI: 10.1103/PhysRevLett.116.154501.

(86) Tunuguntla, R.; Allen, F.; Kim, K.; Belliveau, A.; Noy, A. *Nature Nanotechnology* **2016**, *11*, 338a.

(87) Dellago, C.; Naor, M. M.; Hummer, G. *Physical Review Letters* **2003**, *90*, 105902.

(88) Amiri, H.; Shepard, K. L.; Nuckolls, C.; Hernández Sánchez, R. *Nano Letters* **2017**, *17*, PMID: 28103039, 1204–1211.

(89) Nelson, P. H. *J. Chem. Phys.* **2002**, *117*, 11396–11403.

(90) Yao, Y.-C.; Taqieddin, A.; Alibakhshi, M. A.; Wanunu, M.; Aluru, N. R.; Noy, A. *ACS nano* **2019**, *13*, 12851–12859.

(91) Biesheuvel, P. M.; Bazant, M. Z. *Phys. Rev. E* **2016**, *94*, 050601.

(92) Manghi, M.; Palmeri, J.; Yazda, K.; Henn, F.; Jourdain, V. *Physical Review E* **2017**, *98*, DOI: 10.1103/PhysRevE.98.012605.

(93) Geng, J.; Kim, K.; Zhang, J.; Escalada, A.; Tunuguntla, R.; Comolli, L.; Allen, F.; Shnyrova, A.; Cho, K.; Munoz, D.; Wang, Y.; Grigoropoulos, C.; Ajo-Franklin, C.; Frolov, V.; Noy, A. *Nature* **2014**, *514*, 612–615.

(94) Corry, B. *The Journal of Physical Chemistry B* **2008**, *112*, PMID: 18163610, 1427–1434.

(95) Sanborn, J.; Chen, X.; Yao, Y.-C.; Hammons, J.; Tunuguntla, R.; Zhang, Y.; Newcomb, C.; Soltis, J.; Yoreo, J.; Buuren, A.; Parikh, A.; Noy, A. *Advanced Materials* **2018**, *30*, 1870392.

(96) Tunuguntla, R. H.; Escalada, A.; Frolov, V. A.; Noy, A. *Nature protocols* **2016**, *11*, 2029.

Chapter 3

Carbon Nanotube Porins Synthesis and Characterization

Carbon nanotube porins (CNTPs) are a convenient membrane-based model system for studying nanofluidic transport that replicates a number of key structural features of biological membrane channels. We present a generalized approach for CNTP synthesis using sonochemistry-assisted segmenting of carbon nanotubes. Prolonged tip-sonication in the presence of lipid molecules debundles and fragments long carbon nanotube aggregates into stable and water-soluble individual CNTPs with lengths in the range of 5-20 nm. We discuss the main parameters that determine the efficiency and the yield of this process, describe the optimized conditions for high-yield CNTP synthesis, and demonstrate that this methodology can be adapted for synthesis of CNTPs of different diameters. We also present the optical properties of CNTPs and show that a combination of Raman and UV-Vis-NIR spectroscopy can be used to monitor the quality of the CNTP synthesis. Overall, CNTPs represent a versatile nanopore building block for creating higher-order functional biomimetic materials.

3.1 Introduction

Extreme spatial confinement and internal hydrophobicity inherent to inner pores of carbon nanotubes (CNTs) are highly reminiscent of a number of defining characteristics of biological pore channels [1–3], and give rise to unique transport properties including ultra-fast transport of water and gases

This chapter is adapted with permission from "Tunuguntla, R.H., Chen, X., Belliveau, A., Allen, F.I. and Noy, A., **2017**. High-yield synthesis and optical properties of carbon nanotube porins. *The Journal of Physical Chemistry C* , 121(5), pp. 3117-3125".

[4–6]. Thus, it was inevitable that researchers turned to CNTs as a platform for building model biomimetic nanopores, and initial transport measurements quickly confirmed many theoretical predictions of fast transport in CNT pores [7–9]. However, these experimental platforms were a poor approximation of biological transport since they mostly relied on CNT membranes built from macroscopically-long CNT arrays embedded in a solid polymer or ceramic matrix [7, 9], where the aspect ratios of CNT pores were drastically different from those of biological pore channels. A successful strategy for synthesizing a much closer analog of biological ion channels from bulk CNT material has to accomplish two main goals: (i) solubilize the CNTs to make them compatible with the biological environments , and (ii) segment the CNTs to bring the average lengths to the values that are close to the thickness of lipid membranes, which is a prerequisite for membrane insertion [10]. These two goals are largely intertwined, as unmodified CNTs tend to aggregate in aqueous solutions to form tight bundles, making dispersion and effective cutting much more difficult.

Despite progress in creating CNT suspensions in organic solvents [11–15], aqueous dispersions remain a more elusive target. Researchers have previously used two main methods to disperse CNTs – covalent oxidative functionalization and non-covalent adsorption of dispersants on the CNT surfaces. The carboxylation of CNT surfaces, accomplished by oxidation of CNTs followed by carbodiimide chemistry [16–18], still remains the most popular covalent functionalization method. Strong acids such as sulfuric acid and nitric acid used for the oxidative functionalization break the π-conjugated network on nanotubes and functionalize them with carboxylic acid groups and phenols [19]. This procedure leaves many defects behind and can be detrimental to the optical, electrical and mechanical properties of CNTs. A second approach is based on noncovalent functionalization of CNTs with surfactants [20–22], polymers [23–26], biomolecules [27, 28] or polyaromatic compounds [19]. The noncovalent interaction relies mainly on either hydrophobic [29] or $\pi - \pi$ interactions [30, 31], which preserve the integrity of the π network of the CNTs and their intrinsic properties. For applications that involve subsequent incorporation of CNTs into the lipid bilayer systems, an additional challenge is to use a biocompatible dispersant, as most surfactants are known to disrupt the bilayer integrity [32, 33].

Previous efforts to shorten the carbon nanotubes used either an acid attack in a concentrated sulfuric-nitric acid mixture [34–36], which produced CNT lengths between 100 - 300 nm, or a fluorination-pyrolysis method, which gives ca. 50 nm CNT segments [37]. These rather aggressive treatments introduce a significant number of defects, yet the nanotube fracturing yields fragments that are still 1-2 orders of magnitude longer that what is required to mimic biological entities. A much more successful strategy for creating ultrashort CNTs is based on sonochemical cutting, and was investigated by Dai et al. [38],

who used horn-cup sonication of CNTs solubilized by PEG polymers to cut CNTs into a range of lengths that included the ultrashort 8-16 nm segments. However, this procedure is a multi-step process that requires washing in highly basic solutions to apply a final lipid coating. More recently, Wu et al. [39] obtained 5-10 nm length CNTs by bath-sonicating longer CNTs for 48 hours in concentrated sulphuric/nitric acid and subsequently separating out the shorter fragments by size exclusion chromatography. Even though the resulting CNT segments were suitably short, they were unstable in aqueous solutions and difficult to incorporate into lipid bilayers without the use of microinjection techniques [39].

In our previous work, we showed that short (5-20 nm length) CNT fragments stabilized with lipid surfactants—CNT porins (CNTPs)— represent the first iteration of a biomimetic ion channel that could self-insert into a lipid bilayer [40, 41]. We also demonstrated that extreme water confinement in the CNTP cavity enables ultra-fast proton permeability [42] that is analogous to that of biological proton flux channels. Here, we present an optimized synthetic approach that provides a refined, facile, and practical route to creating CNTPs by using phospholipid functionalization and tip ultrasonication. This approach produces robust, water-soluble CNTPs of different diameters that self-assemble into biological membranes with minimal effort.

We also report characterization approaches that can assess the stability, structural integrity, and activity of CNTPs. Currently, transmission electron microscopy (TEM) and atomic force microscopy (AFM) are the commonly used imaging techniques for carrying out morphological characterization of the carbon nanotubes. Unfortunately, these methods necessitate meticulous sample preparation or even alteration and are inherently restricted to imaging only a small fraction of the sample. In this study, we use fluorescence based assays and ratiometric Raman spectroscopy analysis to determine CNTP density and transport activity. These simpler methods would enable routine optimization, characterization, and allow development of *in vivo* or *in vitro* applications using CNTPs.

3.2 CNTP synthesis and purification

Synthesis and purification of ultrashort CNTs

1,2-dioleoyl-sn-glycero-3-phosphocholine lipid (DOPC) used in this study was obtained from Avanti Polar Lipids. 1.5 nm diameter CNTs were obtained from Nano-Lab Inc. (Cat. No. D1.5L1-5-S) and 0.8 nm diameter CNTs were obtained from Sigma-Aldrich, Inc. (Cat. No. 773735). For a typical CNTP preparation procedure, 28 or 36 mg of DOPC lipid, for 0.8 nm or 1.5 nm

CNTP synthesis, respectively, was added to a 20 mL glass scintillation vial from DOPC lipid stock solution (25 mg/mL DOPC, in chloroform) and the solvent was evaporated using a rotary evaporator (RotaVap, BUCHI) for 10 min. Trace solvent in the vial was further evaporated in a vacuum desiccator overnight. Then, 0.7 (for 0.8 nm CNTs) or 1 mg (for 1.5 nm CNTs) was purified in a thermogravimetric (TGA) analysis system. The maximum baking temperature for 0.8 nm CNTs and 1.5 nm CNTs was set to 474.3 °C and 461.5 °C, respectively. 14 mL of Milli-Q water was added to the purified CNTs and that mixture was added to the corresponding dried lipid film. The CNT/lipid mixture was first bath-sonicated for 20 min (Emerson Electric Co., Model Branson 1510) to disperse the CNTs in lipid solution. This is followed by probe-sonication using a 1/4 inch sonicator micro-tip (QSonica) at 203 W power for 16 hrs. The sonicator was run in 3-second pulses with 1-second pause between each pulse. The QSonica ultrasonication converter head needs to be cooled to avoid overheating during operation. To prevent overheating of this component, we directed a constant stream (∼15 psi) of cool, dry air directly onto the convertor head. In order to keep the sample from overheating, we placed the sample vial into a copper water circulating block that constantly cycles 30 °C coolant through the block to maintain a constant chamber/sample temperature during the 16-hr sonication procedure.

To purify the shortened CNTPs from the uncut CNTs, the sonication-processed solution was transferred to a 15mL conical centrifuge tube and centrifuged at 10300 xg for 1hr at 20 °C followed by a 28000 xg spin for 10 min at 20 °C. After centrifugation, the light-grey colored supernatant containing the CNTP solution was carefully aspirated with a glass pipette and stored at 4 °C. The pellet fraction was discarded.

Liposome and CNT-liposome preparation.

Liposomes were prepared using 1,2-dioleoyl-sn-glycero-3-phosphocholine (DOPC, Avanti Polar Lipids). 2 mg of lipids, dissolved in chloroform, were aliquoted into glass vials and the solvent was evaporated under a stream of argon gas or air and further dried overnight in a vacuum desiccator chamber.

Dye-entrapped liposomes were prepared by adding 1 mL of buffer containing 10 mM pyranine dye, 8-Hydroxypyrene-1,3,6-Trisulfonic Acid (HPTS, Life Technologies), 10 mM HEPES, 150 mM NaCl, 30 mM KCl, pH 7.51 to the dried lipid film to obtain a final lipid concentration of 2 mg/mL. This solution was hydrated at room temperature for 30 minutes. To ensure formation of unilamellar liposomes, the samples underwent 10 cycles of freeze-thaw treatment where the liposomes were flash-frozen in liquid nitrogen and subsequently thawed at 50°C. Liposomes were then extruded 21 times through a 200 nm pore-sized polycarbonate membrane using a mini-extruder (Avanti Po-

lar Lipids). Excess unencapsulated free dye was removed using size exclusion chromatography with a column containing Sepharose CL-6B (Sigma-Aldrich, St. Louis, MO) agarose, and buffer exchanged using 10 mM HEPES, 150 mM NaCl, and 30 mM KCl pH 7.51 buffer as an eluent.

To incorporate CNTPs into the liposomes filled with pyranine dye, we first dried 2 mL of the appropriate DOPC/CNTP complex solution overnight in a vacuum desiccator to remove the solvent. The dried DOPC/CNTP complex was hydrated with 1 mL of dye-buffer (10 mM pyranine, 10 mM HEPES, 150 mM NaCl, 30 mM KCl, pH 7.51) and bath-sonicated to ensure the complex is completely solubilized and detached from the glass vial. This dye-containing DOPC/CNT complex was then used to rehydrate a dried lipid film (2 mg DOPC) to obtain a final lipid concentration of 2 mg/mL. These CNT-liposomes underwent 10 cycles of freeze-thaw treatment as previously described, and were then extruded through a polycarbonate membrane filter using a mini-extruder (Avanti Polar Lipids). Here again, excess unencapsulated dye was removed using size exclusion chromatography with a column containing Sepharose CL-6B (Sigma-Aldrich, St. Louis, MO) agarose, using 10 mM HEPES, 150 mM NaCl, and 30 mM KCl pH 7.51 buffer as an eluent.

CNTP synthesis.

The successful CNTP synthesis procedure needs to break up the bundled CNT aggregates into individual nanotubes, cut them down to biologically compatible dimensions (10-15 nm), and keep them stable in aqueous suspensions. To minimize the level of contamination of the final sample, it is also important to start with a CNT feedstock that is free of amorphous carbon and other impurities. Since these impurities typically oxidize at lower temperatures than the pure CNTs, we used thermogravimetric analysis (TGA) to determine the onset oxidizing temperatures that help to bake off the impurities from the CNT material. We found these temperatures to be 461.6 and 474.3 °C for the 1.5 and 0.8 nm diameter CNT starting material, respectively. Even though the onset temperatures are fairly close for the two CNT source materials that we explored, using a TGA apparatus minimizes the oxidative damage to the CNT material. The purified CNT material is then easily solubilized under gentle sonication in the presence of DOPC lipid molecules, which adsorb on the CNT surface and serve as a surfactant.

The main step in the synthesis procedure is the CNT scission using tip-based ultrasonication (Figure 3.1, inset schematic). Prolonged micro-tip sonication induces cavitation and collapse of microbubbles near the CNT surface and progressively fractures the macroscopic nanotubes into shorter segments, a process that repeats throughout the sonication period [43, 44]. To monitor the kinetics of this process and to determine the sonication time required

to produce the desired CNT lengths we extracted aliquots of the sample at various intervals throughout the procedure and measured the distribution of hydrodynamic sizes in these samples using dynamic light scattering (DLS). The kinetics (Figure 3.1) show a continuous reduction in the average particle size in these samples up until the 16-hour time point, after which we did not observe any significant size changes; therefore, we concluded that the cutting was largely complete by the 16-hour mark. As reported in our previous studies [40, 42], analysis of the length distributions of these nanotubes from the preparations of both the wide (1.5 nm) and narrow (0.8 nm) porins by TEM indicated that the cutting procedure typically produces CNTP lengths of 5-20 nm independent of the diameter of the CNT raw material. We speculate that at these lengths the ultrasound bubble cavitation is no longer able to break apart the CNTs; that may be why ultrasonication past 16 hours does not induce further segmentation.

The subsequent ultra-centrifuge purification step removes the larger uncut CNTs and aggregated CNT bundles (and perhaps also some aggregated CNTPs). The resulting CNTP solution is light grey and remains stable for at least 6 months at 4°C (Figure 3.2). Moreover, we were able to dry the CNTP stock solution completely, and then resuspend it in aqueous solution by simple bath sonication. This behavior indicates that the cut CNTs are well stabilized by the lipid coating. The mechanism of stabilization of surfactant-coated nanotube colloids often relies on electrostatic repulsion between surfactant molecules coating adjacent nanotubes [45]. We assume that the lipid coating offers the same stabilization in our samples. This behavior is also consistent with our recent observation of ordered lipid coatings on CNT surfaces [46].

3.3 Characterization of CNTP batch incorporation yield

Stepwise titration with 1 μL of 1 M HCl in the extravesicular medium led to reductions in the intravesicular pH and in fluorescence emission from entrapped pH-sensitive pyranine dye (8-Hydroxypyrene-1,3,6-trisulfonic acid, trisodium salt); the resulting step changes in fluorescence with pH are used to create a calibration curve to convert the fluorescence emission data to lumenal pH in further experiments. Over the 7.5-6.9 pH range used in this study, the relative fluorescence emission was linearly proportional to the solution pH. For a typical batch activity measurement, 2 mL of buffer (10 mM HEPES, 150 mM NaCl, 30 mM KCl) at pH 6.9 was added to a cuvette and placed in a Fluoromax-4 fluorimeter (Jobin-Yvon) at room temperature for at least 5 minutes with constant stirring until a steady baseline measurement reading is

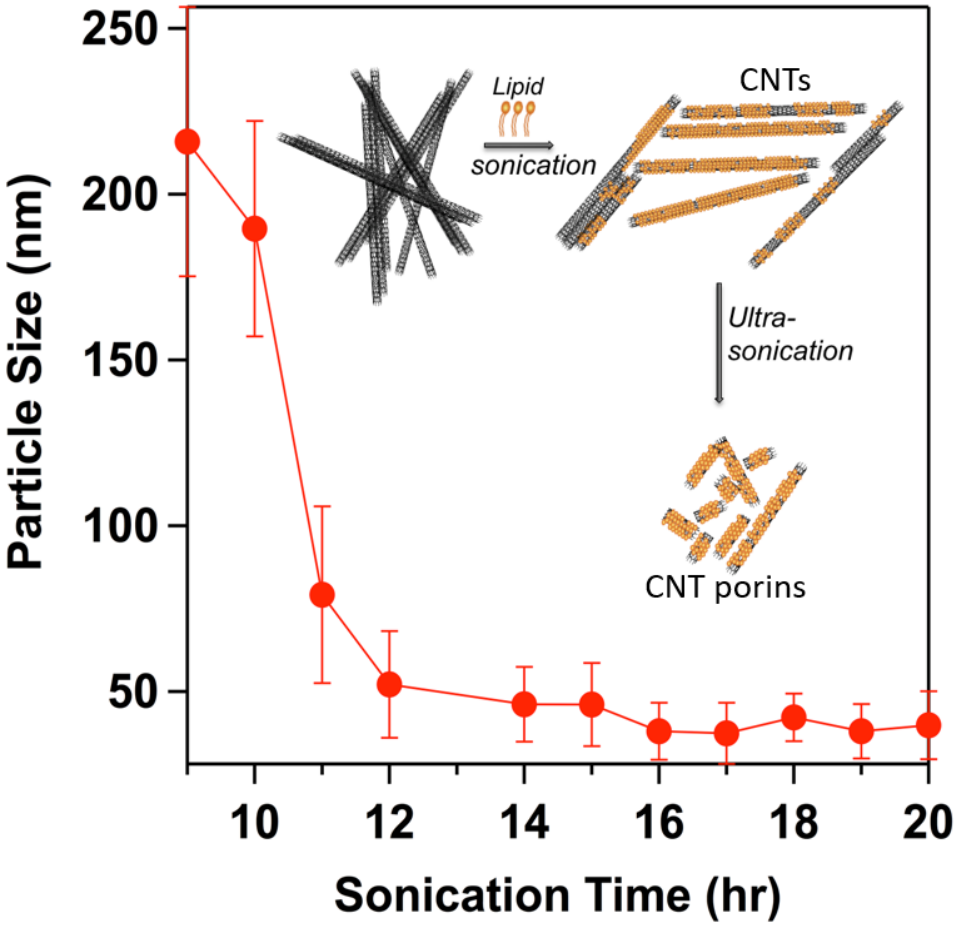

Figure 3.1: CNT cutting by ultrasonication. A plot of the average particle size measured by DLS as a function of sonication time. Inset: Schematics of the ultrasonication cutting procedure.

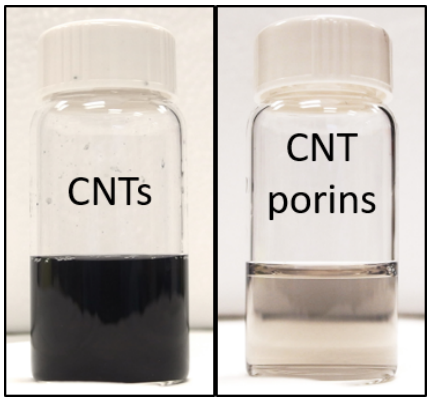

Figure 3.2: Photographs of the CNT dispersion before (left) and after (right) cutting and separation by centrifugation.

reached. We then quickly added 70 μL (pH 7.51) of the LUVs or CNTP-LUVS depending on the experiment, to the cuvette containing a stirrer bar with constant stirring through the entire duration of the experiment. Changes in fluorescence intensity of entrapped pyranine in response to the transmembrane pH gradient dissipation were monitored as a function of time using excitation and emission wavelengths of 450 and 514 nm, respectively. All measurements took place in dark conditions with constant stirring.

CNTP synthesis yield.

We then turned to the optimization of the CNTP synthesis. Several key parameters influence the efficiency and the yield of the sonochemical cutting procedure: solution temperature, sonication power, and lipid-to-CNT mass ratio. The first two parameters should be important for the kinetics of the cutting process, while the mass ratio of the lipid-to-CNT components should have a significant impact on the overall yield since this parameter largely controls the solubilization of the final CNTPs. Our initial assumption was that increasing the lipid-to-CNT ratio would result in increasing favorable interactions between the hydrocarbon lipid chains and the CNT surface, thereby improving the solubility of the material and promoting greater cutting efficiency. To test this assumption, we performed the synthesis protocol using lipid doses ranging from 8 to 60 mg of DOPC lipid per mg of CNT material. We then analyzed the products using the CNTP proton permeability assay [42] as a benchmark of the CNTP activity. This measurement is analogous to an activity-based assay commonly used to characterize protein batches. As a transport-based assay, it is preferable to other approaches that could determine

the concentration of shortened CNTPs, such as small-angle neutron scattering [47, 48], atomic force microscopy [49–52], visible/infrared absorption [53–55], or photoluminescence spectroscopy [29, 56, 57].

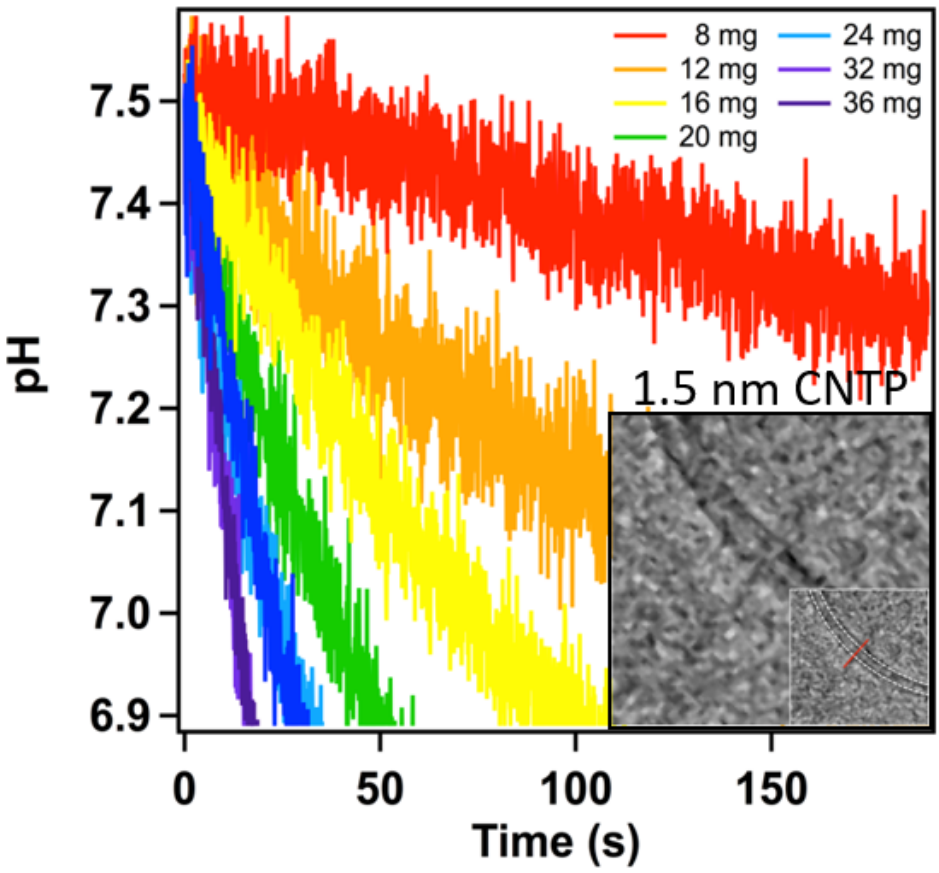

Figure 3.3: CNTP proton permeability assay showing the kinetics of pH change in the lumen of the liposomes containing 1.5 nm diameter CNTPs after rapid acidification of the external solution for different lipid doses used during the CNTP synthesis procedure. Faster kinetics is an indication of a larger number of CNTPs incorporated into the liposome, and thus a higher yield from the synthetic procedure. Insets: Cryo-TEM images of CNTPs in lipid vesicles.

To determine the CNTP activity, we reconstituted a fixed aliquot from a CNTP batch into liposomes containing a pH-sensitive fluorescent pyranine dye, lowered the pH outside the vesicles, and then monitored the luminal dye fluorescence to determine the kinetics of the pH gradient equilibration through the CNTP pores (Figure 3.3,3.4,3.5,3.6). Extracting the slope of each curve from the transport assay, we can plot the bulk transport activity of

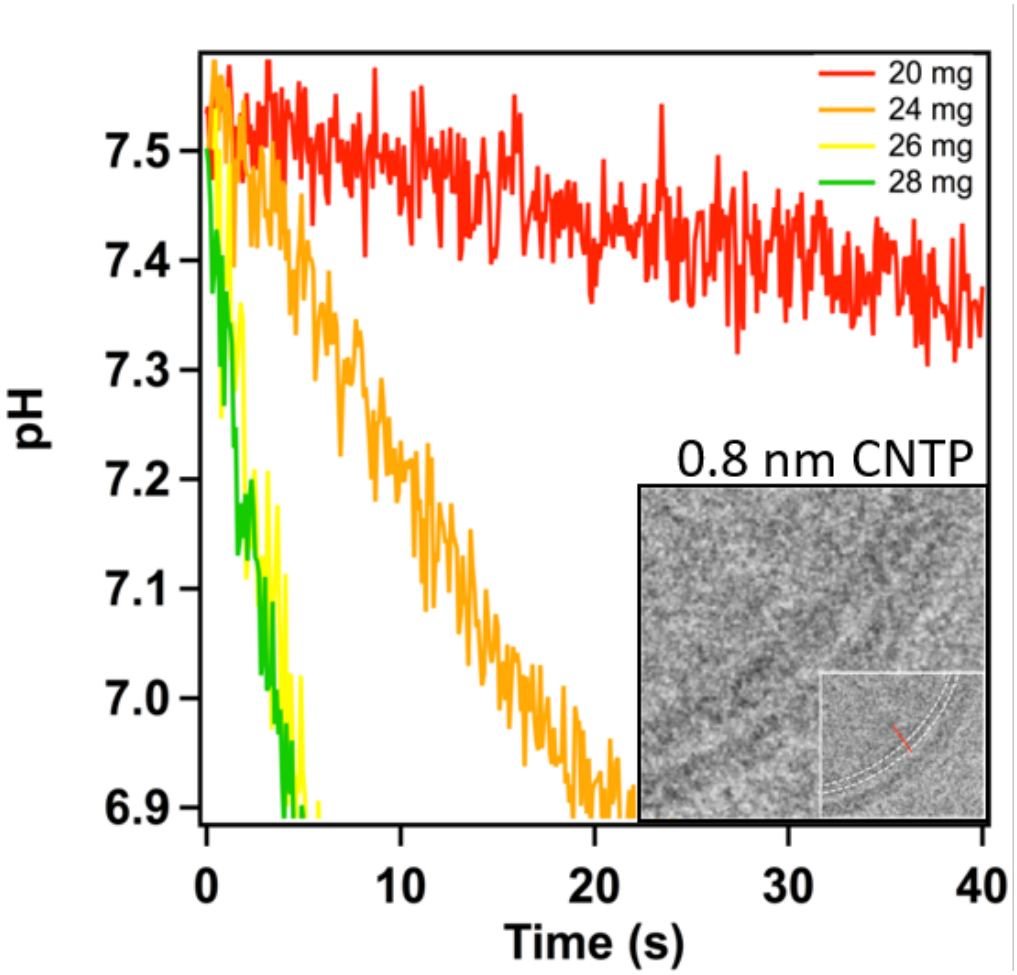

Figure 3.4: CNTP proton permeability assay showing the kinetics of pH change in the lumen of the liposomes containing 0.8 nm diameter CNTPs after rapid acidification of the external solution for different lipid doses used during the CNTP synthesis procedure. Faster kinetics is an indication of a larger number of CNTPs incorporated into the liposome, and thus a higher yield from the synthetic procedure. Insets: Cryo-TEM images of CNTPs in lipid vesicles.

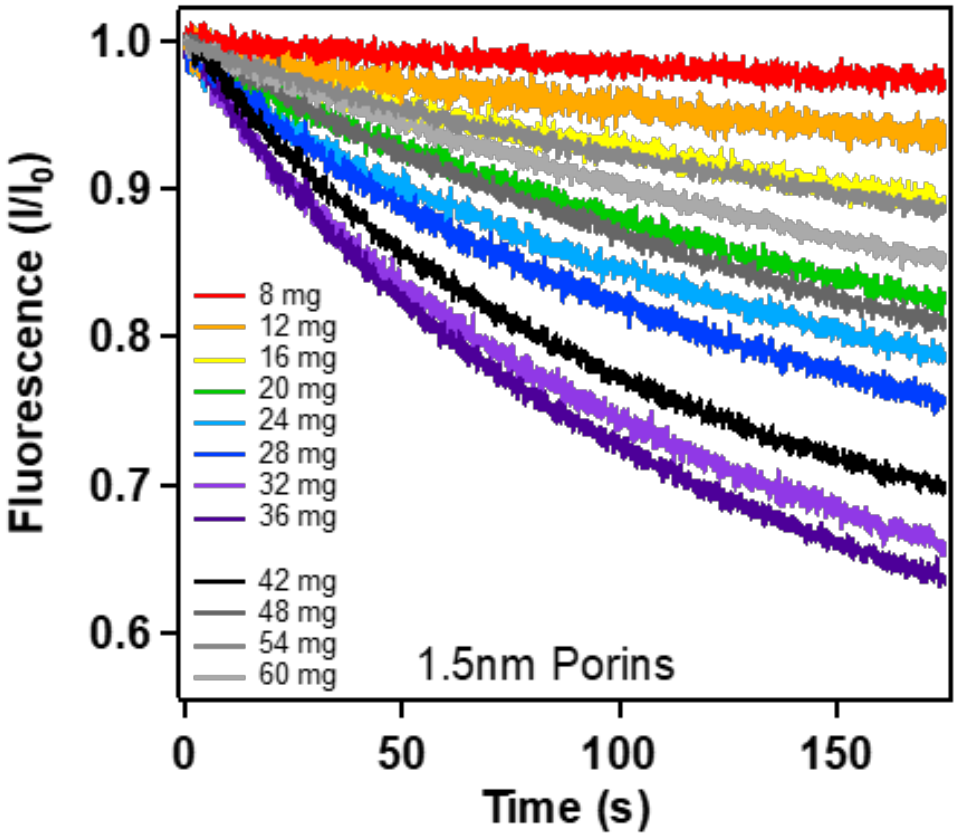

Figure 3.5: Kinetics of the HPTS dye fluorescence intensity as a function of time after rapid acidification of the solution in the cuvette. 1.5 nm CNTPs used in this assay were prepared using lipid dosage as indicated in the plots.

the 1.5 or 0.8 nm porins embedded in liposomes as the rate of pH change within the vesicles (dpH/dt) with respect to lipid dosage (Figure 3.7). We can convert the measured proton permeability into the number of CNTPs per vesicle using the unitary proton permeability of CNTPs as described in our previous work (1.80×10^{-7} and 3.30×10^{-7} nS per 1.5 nm and 0.8 nm CNTP, respectively) [42]. Initially, the observed trend followed our hypothesis — increasing the lipid-to-CNT mass ratio (L:C) in the CNT/lipid mixture before sonication increased the yield of CNTPs in the final product for both 1.5 nm and 0.8 nm CNTPs. Surprisingly, this trend was not monotonic: samples from the batches with L:C mass ratios greater than 40 started to exhibit reduced activity values that quickly dropped down to less than one CNTP per vesicle. Thus, the data clearly point to the existence of the optimal lipid-CNT ratio (36.7 and 41.5 for 1.5 and 0.8 nm diameter CNTPs, respectively)

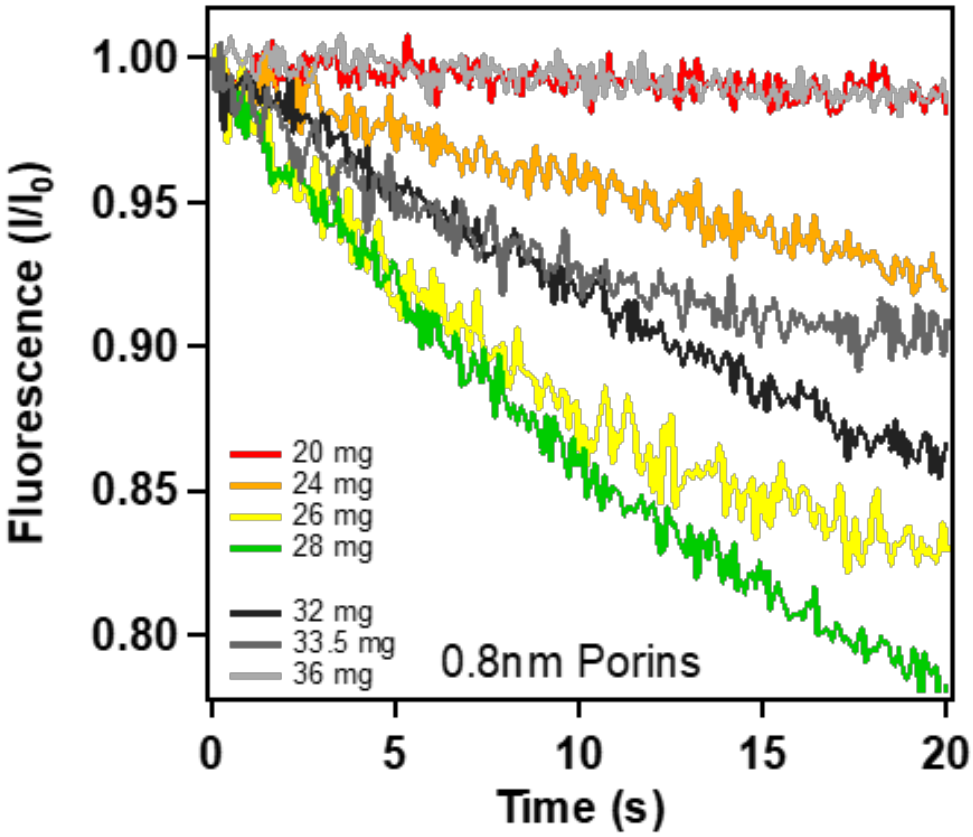

Figure 3.6: Kinetics of the HPTS dye fluorescence intensity as a function of time after rapid acidification of the solution in the cuvette. 0.8 nm CNTPs used in this assay were prepared using lipid dosage as indicated in the plots.

that maximizes the yield of CNTP synthesis. We hypothesize that increasing lipid dosage initially improves the surface coverage on the CNTs, resulting in better solubilization and easier access to the cavitation events produced during sonication. The decrease of the synthesis efficiency observed at higher lipid-to-CNT ratios perhaps indicates that excess DOPC molecules form multilamellar structures on the CNTP, or exist as excess free liposomes in solution that may shield the nanotube surface from the ultrasonic energy required to fracture CNTs.

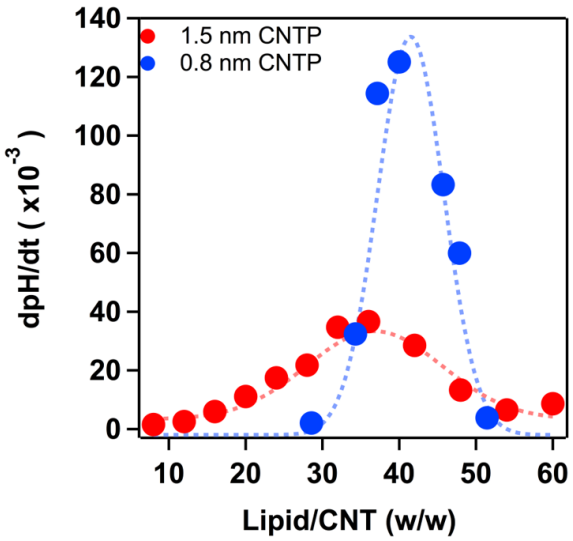

Figure 3.7: Lipid dose variations change CNTP synthesis yield. Plot of the vesicle interior pH change rate (dpH/dt) measured in the proton transport assay as a function of the mass ratio of lipid to CNT used in the synthesis.

3.4 Optical properties

Dynamic light scattering (DLS) measurements.

DOPC and CNTP-DOPC liposome diameters were characterized using a dynamic light scattering (DLS) instrument (Zetasizer Nano-ZS90, Malvern Instruments, UK). Typically, 70 μL of the liposome sample was added to a disposable small volume cuvette (BRAND GmbH & Co. KG, Germany) and light scattering intensity of the liposomes was measured. Each size reading was obtained from an average of 10 individual measurements.

Cryogenic transmission electron microscopy (Cryo-TEM) imaging of CNTP-LUVs.

Samples of CNTP-LUVs for Cryo-TEM were prepared on glow-discharged holey-carbon 200-mesh copper grids (HC-200Cu, EMS) by plunge freezing (Leica EM GP automatic plunge-freezer) into liquid ethane held at liquid nitrogen temperature and blotting both sides of the grids for 3-5 seconds. These samples were continuously stored under liquid nitrogen. Imaging was performed using a Zeiss Libra 120 TEM operating at 120kV using zero-loss filtering with an energy-slit width of 20eV. All the images were acquired under

low-dose conditions (∼10 electrons/Å^2 per image) using a high-sensitivity 4K × 4K Gatan Ultrascan CCD camera at a nominal magnification of typically 50,000x with no binning to give an image pixel size of 0.24nm at the specimen and the defocus values ranged from minimum contrast to 1 μm underfocus.

Dispersion of CNTs and CNTPs for Fluorescence Spectroscopy.

To prepare solutions for fluorescence spectroscopy, 0.5 mg of raw uncut CNT material was dissolved in 1 mL of a 1% SDS in D_2O solution and bath-sonicated for 1 hr, followed by horn-tip sonication at 21 W power for 30 mins. To purify the sample and remove aggregates, the solution was centrifuged at 9000 RPM for 30 mins. We carefully decanted the supernatant and used the resulting CNT dispersion to obtain an emission scan. For measurements on 16 hr sonication-processed CNT porin samples, the dispersion solution contained DOPC phospholipid and D_2O. A typical measurement of 0.8 nm CNTPs used an excitation wavelength range of 500-800 nm, an emission range of 900-1450 nm, a 4 nm slit width, and an integration time of 30 sec on a NanoLog Spectrofluorometer instrument. We note that the limited range of the emission detector of our instrument did not allow for fluorescence analysis of the 1.5 nm sample.

Optical properties of CNTPs.

Encapsulation in amphiphilic lipid molecules preserves most of the optical properties of single-walled CNTs in solution. Absorption spectra of all lipid-CNT complexes (Figure 3.8, 3.9) showed characteristic E22 and E11 optical transitions corresponding to electronic state densities of semiconducting SWCNTs [58]. Researchers have shown that as nanotube lengths approach several nanometers, decreased exciton lifetime can cause spectral peak broadening [59, 60]. We observed peak broadening in the spectra our 1.5 nm CNTP samples compared to the spectra of raw CNT material, but no significant broadening was seen for 0.8 nm porins (Figure 3.8, 3.9). Additionally, Sun et al. [38] reported that for shorter CNT lengths increasing quantum confinement along the CNT axis causes blue shift of the absorbance. We have also observed this blue shift in the UV-Vis-NIR absorption spectra of our 1.5 nm and 0.8 nm CNTPs (Figure 3.8, 3.9), confirming that sonication resulted in significant shortening of the nanotubes.

Since most of the raw CNT material contains a mixture of different CNT structures and chiralities, it is important to characterize the heterogeneity of the starting CNT materials as well as that of the final CNTP product. Two-dimensional photoluminescence (2D PL) excitation/emission spectroscopy map-

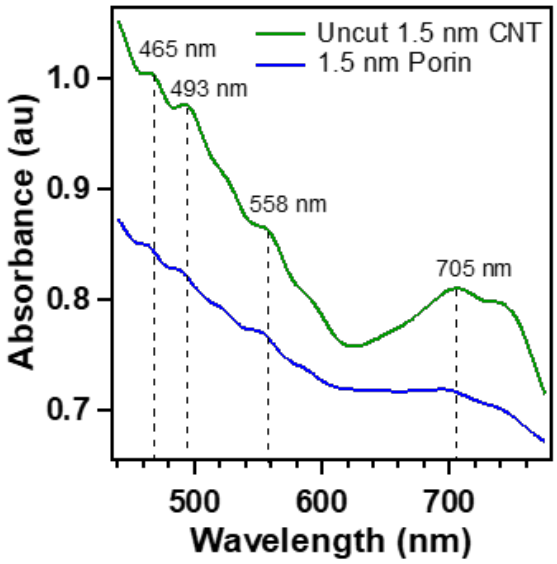

Figure 3.8: UV-Vis-NIR absorption spectra of 1.5 nm diameter CNTs and CNTPs. Dashed lines indicate the locations of major spectral features.

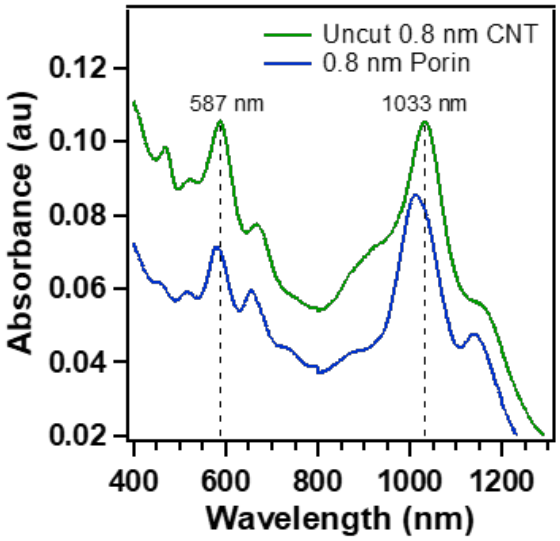

Figure 3.9: UV-Vis-NIR absorption spectra of 0.8 nm diameter CNTs and CNTPs. Dashed lines indicate the locations of major spectral features.

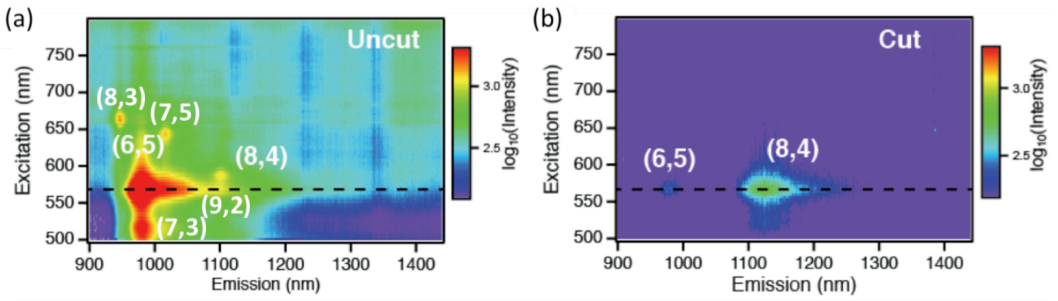

Figure 3.10: 2D fluorescence excitation/emission spectra. (a) 0.8 nm diameter CNT source material sample before sonication processing reveals multiple chiralities and (b) post sonication CNTP sample shows predominance of (8,4) CNT species after cutting.

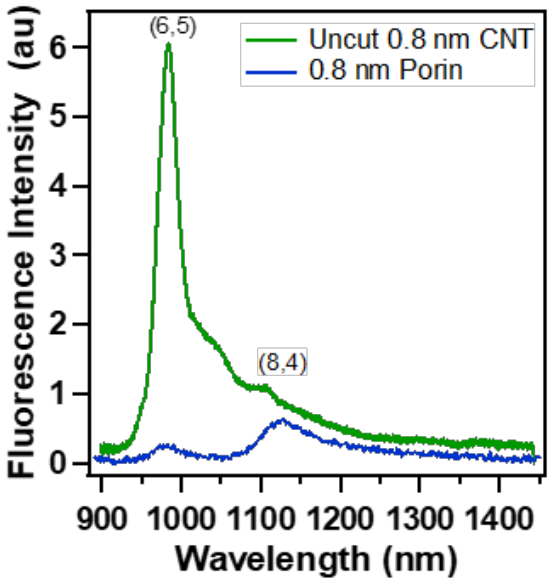

Figure 3.11: Fluorescence emission spectra of 0.8 nm diameter CNTs before and after cutting (λ_{ex} = 568 nm). The shift in relative intensities of the emission peaks indicates that the predominant CNT chirality changes from (6,5) to (8,4) after cutting procedures. Similar analysis of the 1.5 nm diameter porins was not possible because the emission peaks in that sample fall outside the detection range of our instrument.

ping showed six distinct CNT species (Figure 3.10 (a)) for the 0.8 nm CNT samples before sonication, which we assigned to distinct chiral (n, m) indices according to procedures described by Bachilo et al. [61] 2D fluorescence spectra of the samples before and after sonication processing revealed a shift in the predominant CNTP chirality from (6,5) to (8,4) species (Figure 3.10 (b)); a line scan at the excitation wavelength of 568 nm (Figure 3.11), obtained from the 2D plots, clearly shows the change in relative intensities of these two CNT populations. This observation suggests that sonication processing can have strong selectivity towards certain CNT chiralities. A possible explanation of this phenomenon comes from an assessment of the mechanical strength of the different (n, m) species in the sample. For instance, near-armchair configurations are weakest in the longitudinal direction [62] and therefore would be prone to length-wise unzipping during fracture of the CNTs [63, 64], producing graphene flakes. Thus, the initially abundant (6,5) species is largely destroyed during ultrasonication and the more resilient (8,4) (closer to zig-zag configuration) species persist, giving a final CNTP product that largely consists of a single chirality CNT species. These observations suggest that this preferential removal of the armchair-like CNTs could be used as a tool to select certain CNT chiralities in the sample; at the same time, it points to the additional challenges for developing the process for producing CNTPs with armchair-like structure.

3.5 Raman spectroscopy signature

The Raman spectra were measured using a Nicolet Almega XR micro-raman spectrometer at laser wavelengths of 633 nm and 473 nm. The laser power was kept below 100 W/cm^2 for the study of CNT porins to avoid heating the samples. To prepare the samples for Raman analysis, equal aliquots of aqueous dispersions of the CNTP batches were dried on glass slides in a vacuum desiccator for 3-4 hours to form a greasy film spot on the slide and subsequently measured in the spectrometer. The Raman spectra were normalized to the G-band intensity to allow comparison across the varying samples.

Raman spectroscopy analysis of the cut CNTP batches confirms the key role that CNT-lipid interactions play in stabilizing the final product. CNTs exhibit several characteristic peaks in the Raman spectra [65], with the key features in the spectra being the radial breathing modes (RBM), and G-, D-, and G′-bands, each arising from different phonon resonance modes [66]. The comparison between the RBM region spectra of our CNT samples prior to and after the cutting procedure verifies that 16 hours of high-powered, high-frequency ultrasonication did not induce significant changes in the nanotube diameter (Figure 3.12). The RBM region (100-300 cm^{-1}) reveals a bimodal

diameter distribution in the narrow 0.8 nm uncut CNT material with peaks at 290.7 cm^{-1} and 331.2 cm^{-1} (Figure 3.12, red dashed spectrum), corresponding to (8,4) and (6,5) chiralities that were observed in the fluorescence spectra (Figure 3.11). In contrast, the RBM region spectrum of the 0.8 nm porin sample indicates that only the (8,4) chirality has survived the sonication (Figure 3.12, red solid spectrum), which correlates well with our observations from the fluorescence spectrum for these 0.8 nm nanotubes. In the case of the 1.5 nm CNTs, the uncut material contains two peaks (149.9 cm^{-1} and 209.7 cm^{-1}) (Figure 3.12, blue dashed line) that persist in the porin sample (Figure 3.12, blue solid line), however with different relative intensities, perhaps providing further evidence of preferential CNT species removal.

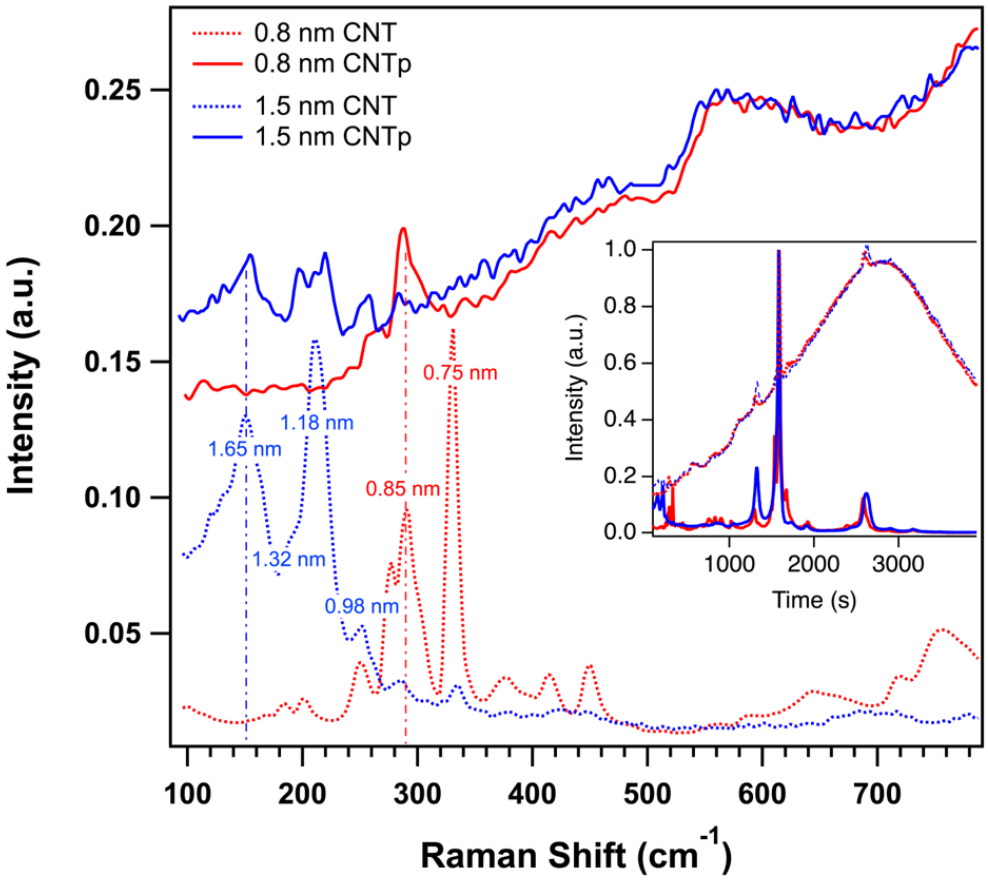

Figure 3.12: Raman spectra of uncut CNTs (dashed lines) and the final product CNTP (solid lines) for 0.8 nm (red) and 1.5 nm (blue) CNTPs. Main panel shows the magnified radial breathing mode (RBM) region of the spectra; Inset shows the whole spectral range.

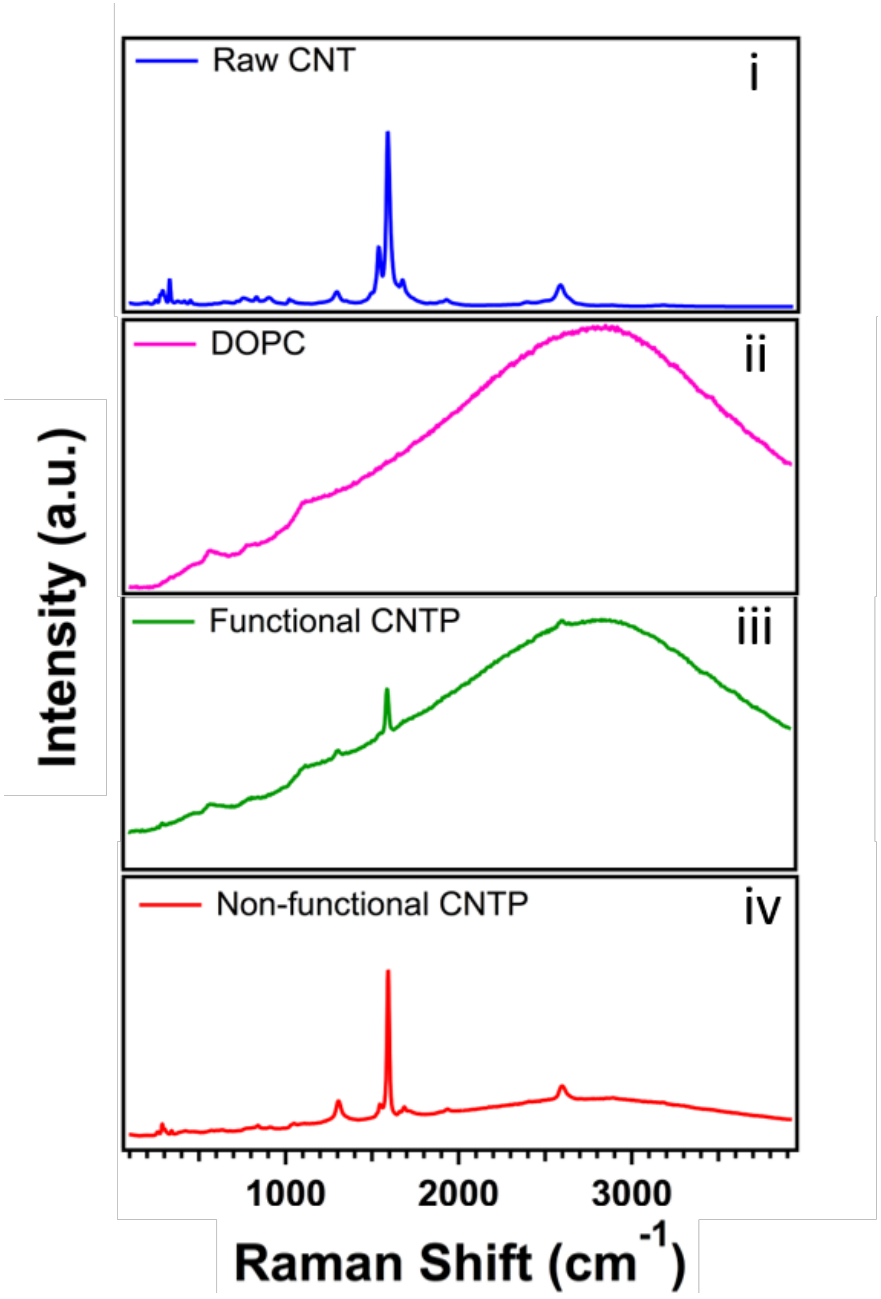

Figure 3.13: Raman spectra of the (i) purified source CNT material, (ii) DOPC lipid, (iii) high-yield CNTP batch, and (iv) low-yield CNTP batch.

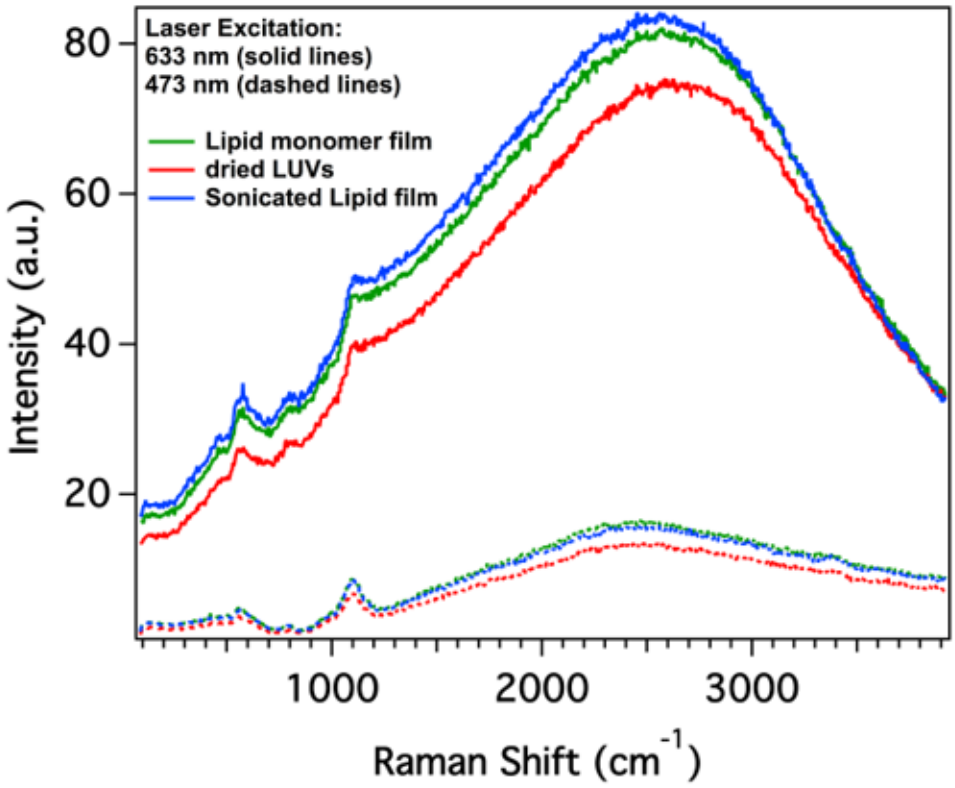

Figure 3.14: Raman spectra of DOPC lipid films. DOPC films prepared from stock DOPC solution (green), dried DOPC LUVs (red), and DOPC after 16-hour sonication (blue). All samples show similar Raman spectral feathers under laser excitation of 633 nm (solid lines) and 473 nm (dashed lines).

Raw CNT material (Figure 3.13 (i)) showed the characteristic signals of the G-band at 1590 cm^{-1}, G′-band at 2600 cm^{-1}, and D-band at 1310 cm^{-1}. Raman spectrum of the DOPC lipid exhibited a broad signal over the entire range of the spectrum with the peak (L-band) signal at the 2800 cm^{-1} (Figure 3.13 (ii)), a feature previously observed for similar lipid monolayer films [67] where the region between 2800-3100 cm^{-1} maps to C-H bond stretching. To exclude the possibility of fluorescence emission contributing to the broad signal, we measured the Raman signal at two different laser excitation wavelengths (473 and 633 nm) and verified that the Raman spectrum contained similar spectral features at both wavelengths (Figure 3.14). Based on these observations we used the broad peak at 2800 cm^{-1} as a signature lipid signal.

A comparison between the Raman spectra of the CNTP batches that exhibited varying levels of porin incorporation efficiency (I.E. - derived from the

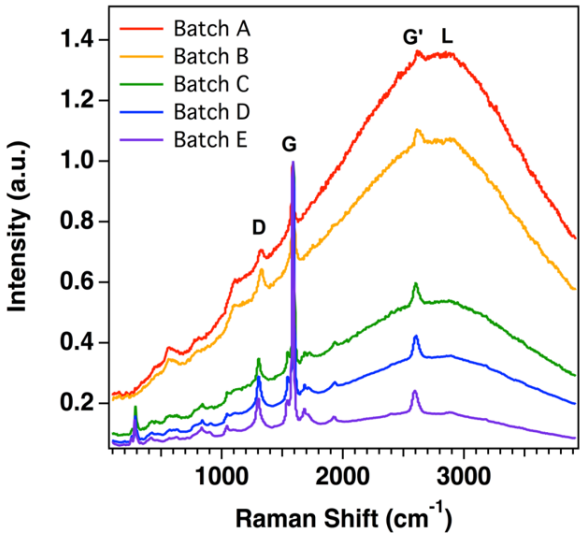

Figure 3.15: Raman spectra of five different CNTP batches (Batch A-E).

Batch	Characteristic peak ratios		
	Lipid/G	D/G′	I.E.
A	1.35	0.52	25.6
B	1.08	0.59	20.9
C	0.54	0.59	3.3
D	0.35	0.68	0.2
E	0.17	0.89	0.1

Table 3.1: Raman ratiometric parameters of different CNTP batches. Raman spectra peak ratios and corresponding incorporation efficiencies for the five bathes shown in Figure 3.15.

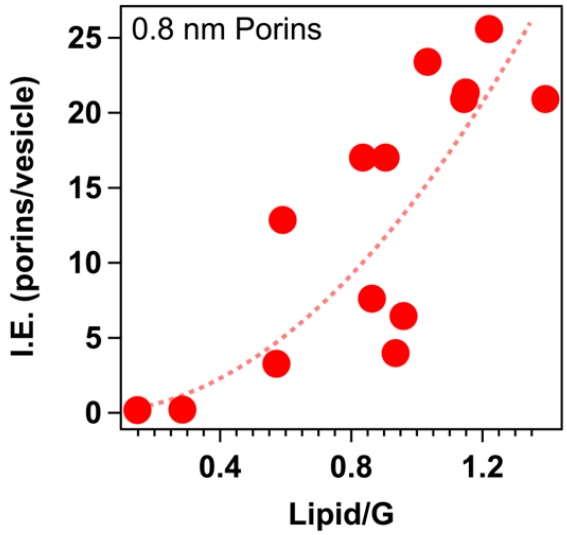

Figure 3.16: Quality parameters for CNTP yield analysis. The CNTP batch yield can be characterized by two parameters derived from the Raman spectra peak ratios. Plots of the incorporation efficiency (I.E.) as a function of the ratio of lipid:G for 0.8 nm CNTP. Raman peak intensities from batches with varying synthesis yield indicate a threshold for producing samples with increasing numbers of porins and CNTP incorporation efficiency.

proton transport assay and reported as the number of CNTPs per 200 nm diameter vesicle) (Figure 3.13 (iii, iv)) immediately reveals significant differences between the two kinds. The L-band intensity corresponding to the Raman signal of the lipid molecules is much stronger for the highly active CNTP batch than for the inactive CNTP batch. Since the processed and centrifuged CNTP sample should contain little free lipid (in the form of micelles or liposomes), the L peak in the high-activity batch spectrum must arise from the lipid that is adsorbed on the nanotube surface. Thus it appears that a highly-active CNTP batch should contain porins that are well coated and solubilized; conversely, a smaller lipid shoulder intensity coupled with a strong G-band suggests a poor lipid coating resulting in reduced CNTP activity (i.e. incorporation efficiency, Figure 3.15, Table 3.1). This observation is consistent with our hypothesis and prior observations that effective solubilization with the lipid is the primary determinant of the CNTP synthesis success and the activity of the synthesized CNTPs.

A more detailed look at the Raman spectral data from all of our CNTP batches allowed us to extract quantitative metrics to address the solubilization and dispersion quality, and also the CNTP yield. We found that the sample

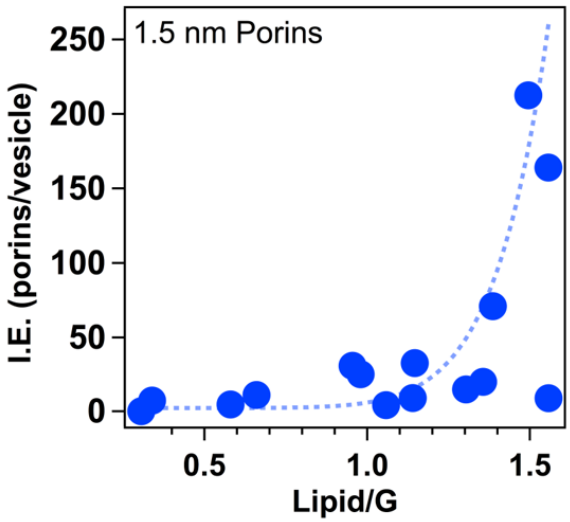

Figure 3.17: Quality parameters for CNTP yield analysis. The CNTP batch yield can be characterized by two parameters derived from the Raman spectra peak ratios. Plots of the incorporation efficiency (I.E.) as a function of the ratio of lipid:G for 1.5 nm CNTP. Raman peak intensities from batches with varying synthesis yield indicate a threshold for producing samples with increasing numbers of porins and CNTP incorporation efficiency.

quality could be characterized by two parameters derived from the Raman spectra: the L:G and G′:D peak ratios (Figure 3.16 - 3.19). The L:G peak ratio measures the relative amount of lipid per graphitic carbon in the CNTP sample and the G′:D peak ratio measures the quality of the graphitic walls of the CNTPs (the second-order G′-band does not require an elastic defect-related scattering process, and is observable only for defect-free sp^2 carbons [68]). Samples that exhibited the highest activity also showed the highest L:G signal ratio, again underscoring the importance of lipid-mediated solubilization for the CNTP synthesis. Interestingly, higher CNTP activity also showed strong correlation with a higher G′:D ratio, indicating perhaps that effective solubilization with lipid protects the CNT walls from excessive defect formation during the sonication cutting.

Overall, the 0.8 nm CNTP samples with a L:G ratio ≥ 0.8 (Figure 3.16) and a G′:D ratio ≥ 1.8 (Figure 3.18), were well solubilized, readily incorporated into lipid bilayers, and performed well in the proton transport assays. In the case of 1.5 nm diameter CNTP samples, an L: G ratio ≥ 1.2 (Figure 3.17) and a G′: D ratio ≥ 1.6 (Figure 3.19) were indicative of a highly functional batch. Even though these metrics are semi-quantitative, they can be an effective,

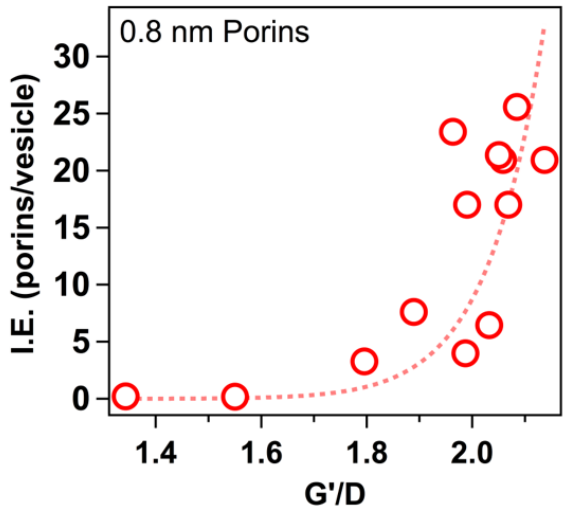

Figure 3.18: Quality parameters for CNTP yield analysis. The CNTP batch yield can be characterized by two parameters derived from the Raman spectra peak ratios. Plots of the incorporation efficiency (I.E.) as a function of the ratio of G′:D for 0.8 nm CNTP. Raman peak intensities from batches with varying synthesis yield indicate a threshold for producing samples with increasing numbers of porins and CNTP incorporation efficiency.

quick, and relatively convenient measures of CNT dispersion and sonication cutting yields; thus, we propose that they can serve as benchmarks for the evaluation of CNTP synthesis procedures.

3.6 Conclusions

Detailed analysis of the sonication-based procedure for CNTP synthesis and comprehensive characterization of the optical properties of the product CNTPs that we have presented shows that only those samples in which the cut CNTs are well solubilized with lipid coating exhibit high CNTP activity. The yield of the CNTPs varies non-monotonically with the added amounts of the lipid, and we report the optimized synthesis conditions for the production of CNTPs of different diameters. Our data indicate that the ultrasonication-based cutting process is highly complicated and could result in preferential removal of several types of the CNT species, necessitating detailed characterization of the product CNTPs. Finally, we present semi-quantitative metrics that can characterize the efficiency of the CNTP synthesis and the quality of the product CNTPs. These metrics give researchers a quick means of compar-

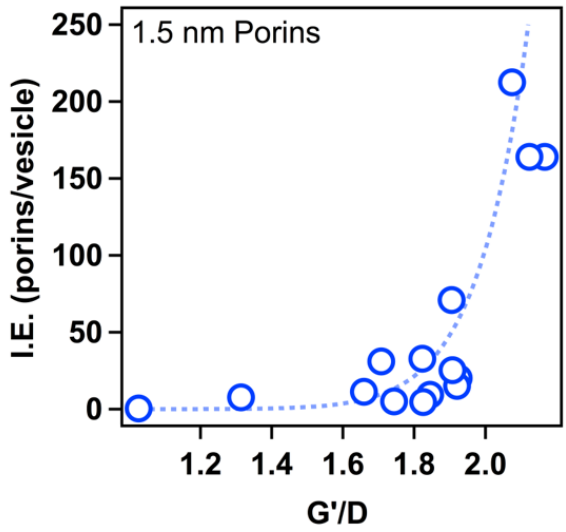

Figure 3.19: Quality parameters for CNTP yield analysis. The CNTP batch yield can be characterized by two parameters derived from the Raman spectra peak ratios. Plots of the incorporation efficiency (I.E.) as a function of the ratio of G′:D for 1.5 nm CNTP. Raman peak intensities from batches with varying synthesis yield indicate a threshold for producing samples with increasing numbers of porins and CNTP incorporation efficiency.

ing the batches produced from different sources, and also give them the tools to use in further optimization efforts. Similar approaches could also be used in the future development of functionally diverse CNTPs for a wide range of applications in biomimetic and biological systems.

References

(1) Chernyshev, A.; Armstrong, K. M.; Cukierman, S. *Biophysical journal* **2003**, *84*, 238–250.

(2) Agre, P.; Bonhivers, M.; Borgnia, M. J. *Journal of Biological Chemistry* **1998**, *273*, 14659–14662.

(3) Doyle, D. A.; Cabral, J. M.; Pfuetzner, R. A.; Kuo, A.; Gulbis, J. M.; Cohen, S. L.; Chait, B. T.; MacKinnon, R. *science* **1998**, *280*, 69–77.

(4) Hummer, G.; Rasaiah, J. C.; Noworyta, J. P. *Nature* **2001**, *414*, 188.

(5) Hummer, G. *Molecular Physics* **2007**, *105*, 201–207.

(6) Noy, A.; Park, H. G.; Fornasiero, F.; Holt, J. K.; Grigoropoulos, C. P.; Bakajin, O. *Nano today* **2007**, *2*, 22–29.

(7) Hinds, B. J.; Chopra, N.; Rantell, T.; Andrews, R.; Gavalas, V.; Bachas, L. G. *Science* **2004**, *303*, 62–65.

(8) Majumder, M.; Chopra, N.; Andrews, R.; Hinds, B. J. *Nature* **2005**, *438*, 44.

(9) Holt, J. K.; Park, H. G.; Wang, Y.; Stadermann, M.; Artyukhin, A. B.; Grigoropoulos, C. P.; Noy, A.; Bakajin, O. *Science* **2006**, *312*, 1034–1037.

(10) Jensen, M. Ø.; Mouritsen, O. G. *Biochimica et Biophysica Acta (BBA)-Biomembranes* **2004**, *1666*, 205–226.

(11) Chen, J.; Hamon, M. A.; Hu, H.; Chen, Y.; Rao, A. M.; Eklund, P. C.; Haddon, R. C. *Science* **1998**, *282*, 95–98.

(12) Dumonteil, S.; Demortier, A.; Detriche, S.; Raes, C.; Fonseca, A.; Rühle, M.; Nagy, J. *Journal of nanoscience and nanotechnology* **2006**, *6*, 1315–1318.

(13) Shigeta, M.; Kamiya, K.; Uejima, M.; Okada, S. *Japanese Journal of Applied Physics* **2015**, *54*, 035101.

(14) Jagadish, K.; Srikantaswamy, S.; Byrappa, K.; Shruthi, L.; Abhilash, M. R. *Journal of Nanomaterials* **2015**, *16*, 320.

(15) Kharissova, O. V.; Kharisov, B. I.; de Casas Ortiz, E. G. *Rsc Advances* **2013**, *3*, 24812–24852.

(16) Bahr, J. L.; Tour, J. M. *Journal of Materials Chemistry* **2002**, *12*, 1952–1958.

(17) Banerjee, S.; Hemraj-Benny, T.; Wong, S. S. *Journal of nanoscience and nanotechnology* **2005**, *5*, 841–855.

(18) Tasis, D.; Tagmatarchis, N.; Bianco, A.; Prato, M. *Chemical reviews* **2006**, *106*, 1105–1136.

(19) Gooding, J. J. *Electrochimica Acta* **2005**, *50*, 3049–3060.

(20) Melbourne, J.; Clancy, A.; Seiffert, J.; Skepper, J.; Tetley, T. D.; Shaffer, M. S.; Porter, A. *Biomaterials* **2015**, *55*, 24–32.

(21) Matarredona, O.; Rhoads, H.; Li, Z.; Harwell, J. H.; Balzano, L.; Resasco, D. E. *The Journal of Physical Chemistry B* **2003**, *107*, 13357–13367.

(22) Yang, K.; Yi, Z.; Jing, Q.; Yue, R.; Jiang, W.; Lin, D. *Chinese science bulletin* **2013**, *58*, 2082–2090.

(23) Kim, O.-K.; Je, J.; Baldwin, J. W.; Kooi, S.; Pehrsson, P. E.; Buckley, L. J. *Journal of the American Chemical Society* **2003**, *125*, 4426–4427.

(24) Murphy, R.; Coleman, J. N.; Cadek, M.; McCarthy, B.; Bent, M.; Drury, A.; Barklie, R. C.; Blau, W. J. *The Journal of Physical Chemistry B* **2002**, *106*, 3087–3091.

(25) O'Connell, M. J.; Boul, P.; Ericson, L. M.; Huffman, C.; Wang, Y.; Haroz, E.; Kuper, C.; Tour, J.; Ausman, K. D.; Smalley, R. E. *Chemical physics letters* **2001**, *342*, 265–271.

(26) Ju, S.-Y.; Doll, J.; Sharma, I.; Papadimitrakopoulos, F. *Nature nanotechnology* **2008**, *3*, 356.

(27) Zheng, M.; Jagota, A.; Semke, E. D.; Diner, B. A.; McLean, R. S.; Lustig, S. R.; Richardson, R. E.; Tassi, N. G. *Nature materials* **2003**, *2*, 338.

(28) Zheng, M.; Jagota, A.; Strano, M. S.; Santos, A. P.; Barone, P.; Chou, S. G.; Diner, B. A.; Dresselhaus, M. S.; Mclean, R. S.; Onoa, G. B., et al. *Science* **2003**, *302*, 1545–1548.

(29) O'connell, M. J.; Bachilo, S. M.; Huffman, C. B.; Moore, V. C.; Strano, M. S.; Haroz, E. H.; Rialon, K. L.; Boul, P. J.; Noon, W. H.; Kittrell, C., et al. *Science* **2002**, *297*, 593–596.

(30) Chen, R. J.; Zhang, Y.; Wang, D.; Dai, H. *Journal of the American Chemical Society* **2001**, *123*, 3838–3839.

(31) Peng, X.; Komatsu, N.; Bhattacharya, S.; Shimawaki, T.; Aonuma, S.; Kimura, T.; Osuka, A. *Nature Nanotechnology* **2007**, *2*, 361.

(32) Nagawa, Y.; Regen, S. L. *Journal of the American Chemical Society* **1991**, *113*, 7237–7240.

(33) Nazari, M.; Kurdi, M.; Heerklotz, H. *Biophysical journal* **2012**, *102*, 498–506.

(34) Ziegler, K. J.; Gu, Z.; Peng, H.; Flor, E. L.; Hauge, R. H.; Smalley, R. E. *Journal of the American Chemical Society* **2005**, *127*, 1541–1547.

(35) Chen, Z.; Kobashi, K.; Rauwald, U.; Booker, R.; Fan, H.; Hwang, W.-F.; Tour, J. M. *Journal of the American Chemical Society* **2006**, *128*, 10568–10571.

(36) Liu, J.; Rinzler, A. G.; Dai, H.; Hafner, J. H.; Bradley, R. K.; Boul, P. J.; Lu, A.; Iverson, T.; Shelimov, K.; Huffman, C. B., et al. *Science* **1998**, *280*, 1253–1256.

(37) Gu, Z.; Peng, H.; Hauge, R.; Smalley, R.; Margrave, J. *Nano Letters* **2002**, *2*, 1009–1013.

(38) Sun, X.; Zaric, S.; Daranciang, D.; Welsher, K.; Lu, Y.; Li, X.; Dai, H. *Journal of the American Chemical Society* **2008**, *130*, 6551–6555.

(39) Liu, L.; Yang, C.; Zhao, K.; Li, J.; Wu, H.-C. *Nature communications* **2013**, *4*, 2989.

(40) Geng, J.; Kim, K.; Zhang, J.; Escalada, A.; Tunuguntla, R.; Comolli, L. R.; Allen, F. I.; Shnyrova, A. V.; Cho, K. R.; Munoz, D., et al. *Nature* **2014**, *514*, 612.

(41) Kim, K.; Geng, J.; Tunuguntla, R.; Comolli, L. R.; Grigoropoulos, C. P.; Ajo-Franklin, C. M.; Noy, A. *Nano letters* **2014**, *14*, 7051–7056.

(42) Tunuguntla, R. H.; Allen, F. I.; Kim, K.; Belliveau, A.; Noy, A. *Nature nanotechnology* **2016**, *11*, 639.

(43) Pagani, G.; Green, M. J.; Poulin, P.; Pasquali, M. *Proceedings of the National Academy of Sciences* **2012**, *109*, 11599–11604.

(44) Chew, H. B.; Moon, M.-W.; Lee, K.; Kim, K.-S. *Proceedings of the Royal Society A: Mathematical, Physical and Engineering Sciences* **2010**, *467*, 1270–1289.

(45) White, B.; Banerjee, S.; O'Brien, S.; Turro, N. J.; Herman, I. P. *The Journal of Physical Chemistry C* **2007**, *111*, 13684–13690.

(46) Tran, I. C.; Tunuguntla, R. H.; Kim, K.; Lee, J. R.; Willey, T. M.; Weiss, T. M.; Noy, A.; Van Buuren, T. *Nano letters* **2016**, *16*, 4019–4024.

(47) Yurekli, K.; Mitchell, C. A.; Krishnamoorti, R. *Journal of the American Chemical Society* **2004**, *126*, 9902–9903.

(48) Zhou, W.; Islam, M.; Wang, H.; Ho, D.; Yodh, A.; Winey, K. I.; Fischer, J. E. *Chemical Physics Letters* **2004**, *384*, 185–189.

(49) Nicolosi, V.; Cathcart, H.; Dalton, A. R.; Aherne, D.; Dieckmann, G. R.; Coleman, J. N. *Biomacromolecules* **2008**, *9*, 598–602.

(50) Cathcart, H.; Quinn, S.; Nicolosi, V.; Kelly, J. M.; Blau, W. J.; Coleman, J. N. *The Journal of Physical Chemistry C* **2007**, *111*, 66–74.

(51) Furtado, C.; Kim, U.; Gutierrez, H.; Pan, L.; Dickey, E.; Eklund, P. C. *Journal of the American Chemical Society* **2004**, *126*, 6095–6105.

(52) Bergin, S. D.; Nicolosi, V.; Cathcart, H.; Lotya, M.; Rickard, D.; Sun, Z.; Blau, W. J.; Coleman, J. N. *The Journal of Physical Chemistry C* **2008**, *112*, 972–977.

(53) Bergin, S. D.; Nicolosi, V.; Giordani, S.; de Gromard, A.; Carpenter, L.; Blau, W. J.; Coleman, J. N. *Nanotechnology* **2007**, *18*, 455705.

(54) Grossiord, N.; van der Schoot, P.; Meuldijk, J.; Koning, C. E. *Langmuir* **2007**, *23*, 3646–3653.

(55) Moore, V. C.; Strano, M. S.; Haroz, E. H.; Hauge, R. H.; Smalley, R. E.; Schmidt, J.; Talmon, Y. *Nano letters* **2003**, *3*, 1379–1382.

(56) Okazaki, T.; Saito, T.; Matsuura, K.; Ohshima, S.; Yumura, M.; Iijima, S. *Nano letters* **2005**, *5*, 2618–2623.

(57) McDonald, T. J.; Engtrakul, C.; Jones, M.; Rumbles, G.; Heben, M. J. *The Journal of Physical Chemistry B* **2006**, *110*, 25339–25346.

(58) Bachilo, S. M.; Strano, M. S.; Kittrell, C.; Hauge, R. H.; Smalley, R. E.; Weisman, R. B. *science* **2002**, *298*, 2361–2366.

(59) Chang, E.; Bussi, G.; Ruini, A.; Molinari, E. *Physical review letters* **2004**, *92*, 196401.

(60) Spataru, C. D.; Ismail-Beigi, S.; Benedict, L. X.; Louie, S. G. *Physical Review Letters* **2004**, *92*, 077402.

(61) Weisman, R. B.; Bachilo, S. M. *Nano Letters* **2003**, *3*, 1235–1238.

(62) Belytschko, T.; Xiao, S.; Schatz, G. C.; Ruoff, R. *Physical Review B* **2002**, *65*, 235430.

(63) Zhang, H.; Zhao, M.; He, T.; Zhang, X.; Wang, Z.; Xi, Z.; Yan, S.; Liu, X.; Xia, Y.; Mei, L. *Physical Chemistry Chemical Physics* **2010**, *12*, 13674–13680.

(64) Kosynkin, D. V.; Higginbotham, A. L.; Sinitskii, A.; Lomeda, J. R.; Dimiev, A.; Price, B. K.; Tour, J. M. *Nature* **2009**, *458*, 872.

(65) Dresselhaus, M.; Dresselhaus, G.; Jorio, A.; Souza Filho, A.; Saito, R. *Carbon* **2002**, *40*, 2043–2061.

(66) Saito, R.; Jorio, A.; Hafner, J.; Lieber, C.; Hunter, M.; McClure, T.; Dresselhaus, G.; Dresselhaus, M. *Physical Review B* **2001**, *64*, 085312.

(67) Opilik, L.; Bauer, T.; Schmid, T.; Stadler, J.; Zenobi, R. *Physical Chemistry Chemical Physics* **2011**, *13*, 9978–9981.

(68) Costa, S.; Borowiak-Palen, E.; Kruszynska, M.; Bachmatiuk, A.; Kalenczuk, R. *Materials Science-Poland* **2008**, *26*, 433–441.

Chapter 4

Carbon Nanotube Porins in Amphiphilic Block Copolymers

Biological membranes provide a fascinating example of a separation system that is multifunctional, tunable, precise, and efficient. Biomimetic membranes, which mimic the architecture of cellular membranes, have the potential to deliver significant improvements in specificity and permeability. Here, a fully synthetic biomimetic membrane is reported that incorporates ultra-efficient 1.5 nm diameter carbon nanotube porin (CNTPs) channels in a block-copolymer matrix. It is demonstrated that CNTPs maintain high proton and water permeability in these membranes. CNTPs can also mimic the behavior of biological gap junctions by forming bridges between vesicular compartments that allow transport of small molecules.

4.1 Introduction

Energy-efficient molecular separations are fundamental to a number of modern industrial, environmental, and biomedical processes including large-scale water treatment, water desalination, kidney dialysis, sterile filtration, and manufacturing of pharmaceuticals [1–3]. Although synthetic polymeric membranes have come to dominate this application landscape, ever increasing demands continue to fuel the search for energy-efficient membranes that can provide both high selectivity and high permeability in the critical ca. 1 nm pore size.

This chapter is adapted with permission from "Sanborn, J.R., Chen, X., Yao, Y.C., Hammons, J.A., Tunuguntla, R.H., Zhang, Y., Newcomb, C.C., Soltis, J.A., De Yoreo, J.J., Van Buuren, A. and Parikh, A.N., **2018**. Carbon Nanotube Porins in Amphiphilic Block Copolymers as Fully Synthetic Mimics of Biological Membranes. *Advanced Materials*, 30(51), p.1803355". Copyright 2018 Wiley publishing.

To this end, biological membranes represent an attractive alternative. To achieve high levels of selectivity and permeability for separation and transport of nanometer-scale solutes, cellular membranes adopt a structural paradigm that is fundamentally different from conventional polymer membrane materials. Cellular membranes use a solute-impermeable, amphiphilic bilayer matrix that incorporates a variety of highly specific nanopore proteins (e.g., porins, gated ion-channels, connexins, etc.), which shuttle molecular or ionic solutes across the cellular or sub-cellular boundaries and enable highly selective material exchange between the cells and their surroundings [4, 5].

Taking inspiration from biology, researchers made several efforts to pursue robust and scalable synthetic membranes that either incorporate or inherently emulate functional biological transport units. Recent studies demonstrated successful lipid bilayer incorporation of a number of artificial nanopores based on dendritic dipeptide scaffold [6], G-quadruplexes [7], and self-assembled pillar arenes [8]s Other notable classes of artificial membrane nanopores include peptide-based nanopores, 3D membrane cages [9], and large and complex DNA origami nanopores [10–12]. We have recently introduced another class of artificial membrane nanopores based on carbon nanotube scaffolds: carbon nanotube porins (CNTPs) [13]. CNTPs are short segments of lipid-coated, single-wall carbon nanotubes produced by sonication-cutting [14] that can insert into lipid membranes and form defined ca. 1 nm diameter membrane pores with atomically smooth hydrophobic walls that support transport of protons and water [15, 16]. In addition, larger 1.5 nm diameter CNTPs enable transport of ions, macromolecular polymers, or ssDNA. CNTPs are unique among biomimetic nanopores because carbon nanotubes are robust and highly chemically resistant, which make them amenable for use in a wider range of separation processes including those that requiring harsh environments. Unfortunately, the lipid bilayer matrix, into which the CNTPs are embedded, almost completely negates these advantages since it is fragile and disassembles in non-aqueous environments or upon exposure to air.

A robust and flexible membrane matrix is thus another critical component of an artificial membrane. Many amphiphilic block copolymers form bilayer motifs (i.e., polymersomes) in their dilute suspensions [17–21], making them a leading alternative to lipid-based liposomal membranes. Compared to liposomes, polymersomes are mechanically more robust, and offer a wider range of membrane elasticities and degrees of passive membrane permeability [17]. For instance, higher bending moduli of polymer vesicles, 40-460 k_BT (compared to 10-30 k_BT for lipid vesicles) make them less prone to bending deformations and their lower stretching moduli (80-100 versus 250-1000 mN m^{-1} for vesicles) render them more resistant to strain-induced fractures, allowing them to withstand volume expansion/compression under osmotic stresses [22–24]. Moreover, compared to lipid membranes, single component, homogeneous

polymer membranes in their fluid state have lower water permeabilities (0.7-10 versus 15-150 μm s^{-1}) [25, 26] and reduced lateral fluidities (0.1-0.01 versus 1-4 μm^2 s^{-1}) [27–29]. Furthermore, a thicker hydrophobic core in polymer membranes (8-10 versus 3-4 nm for lipid bilayers) should provide a better match and consequently higher degree of stabilization for the average CNTP length of 10-12 nm (we also note that, due to the nature of the sonication-cutting procedure used to synthesize CNTPs, they show a wide-size distribution [13], and thus a portion of CNTPs incorporated into polymersome membrane is still expected to protrude beyond the membrane).

Here, we report integration of CNTP channels into poly(butadiene)-poly(ethylene oxide) (PBD_{22}-PEO_{14}) polymer membranes, mimicking the structure, architecture, and basic functionality of biological membranes in an all-synthetic architecture. Proton and water transport measurements show that carbon nanotube porins maintain their high permeability in the polymer membrane environment. In a significant expansion of the CNTP platform capabilities, we also demonstrate that CNTPs embedded in polymersomes can transport small-molecule reagents between vesicular compartments opening new opportunities for delivery molecular reagents to vesicular compartments to initiate confined chemical reactions and mimic the sophisticated transport-mediated behaviors of biological gap junctions.

4.2 Materials preparation

materials

We used 1.5 nm diameter P2 CNTs (Carbon Solutions Inc.) to produce CNTPs. P2 CNTs contain a higher concentration of defects than the raw CNT stock that we used in previous studies [14, 15] (as indicated by an increased D-band signal in the Raman spectra, see Figure 4.1) and we found that these defects resulted in more efficient cutting and an increased yield of CNTPs. 1,2-dioleoyl-sn-glycero-3-phosphocholine (DOPC) and Rhodamine B 1,2-dioleoyl-sn-glycero-3-phosphoethanolamine (Rhodamine B DOPE) were obtained from Avanti Polar Lipids. PBD-PEO 1800 polymer (P10191) was obtained from Polymer Source Inc. Horseradish peroxidase (HRP, P6782), 8-Hydroxypyrene-1,3,6-trisulfonic acid trisodium salt (HPTS, H1529), luminol sodium salt (A4685), calcium chloride, hydrogen peroxide (216763), phosphate buffered saline (P4417), 4-(2-Hydroxyethyl)piperazine-1-ethanesulfonic acid (HEPES, RDD002), hydrochloric acid solution (H9892), sodium chloride (S7653), potassium chloride (P9333), and deuterium oxide (151882) were obtained from Sigma-Aldrich. Fluo-4 pentapotassium salt (F14200) was obtained from Thermo Fisher Scientific Inc. Pre-assembled extruders with 200 and 400

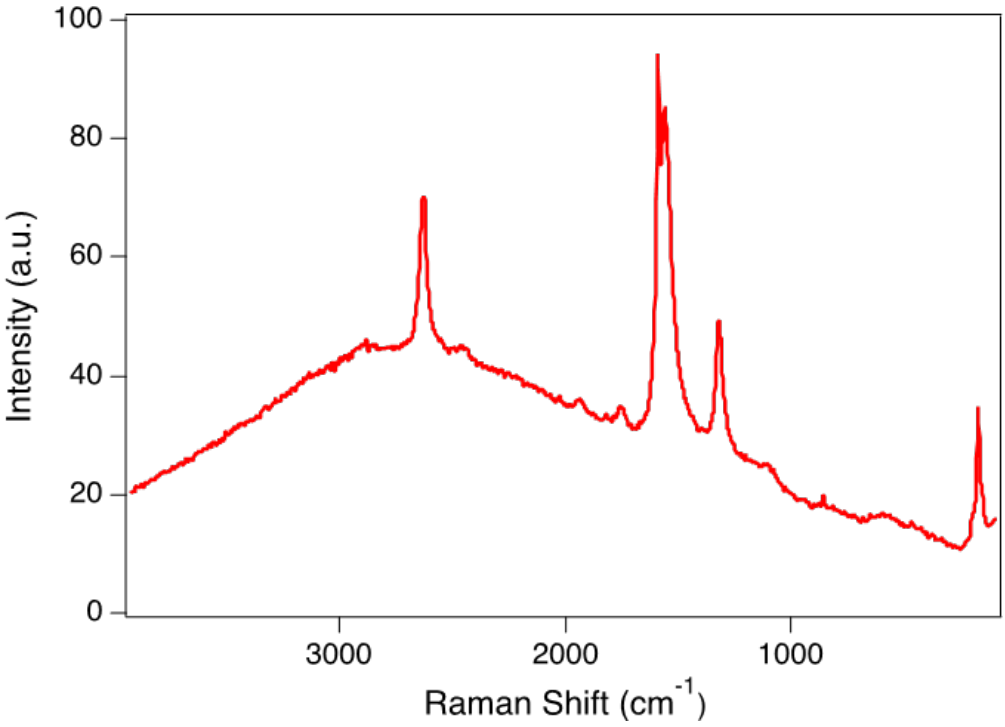

Figure 4.1: Raman spectrum collected from CNTPs. The major RBM peak is located at 176 cm^{-1} and indicates that the dominant CNT fractions have a diameter of 1.5 nm.

nm pore sizes were obtained from T&T Scientific Inc.

vesicle preparation

PBD-PEO diblock-copolymer vesicle were made following previously described protocols with minor changes [29]. Briefly, 5 mg of PBD-PEO 1800 suspended in chloroform was deposited in a glass vial and dried under vacuum overnight to remove all traces of chloroform. The film was resuspended in buffer and heated to 70 °C for 30 min before stirring at 200 RPM for an additional 30 min to form multilamellar vesicles. To convert them into unilamellar vesicles, the solution was subjected to 10 freeze-thaw cycles and then heated to 70 °C prior to mechanical extrusion through 400 or 200 nm tract-etched membranes. To incorporate 1.5 nm diameter CNTPs into the polymersomes, we adapted the protocols developed for incorporating CNTPs into lipid vesicles [30]. We first dehydrated 0.5-1.5 mL of the appropriate CNTP solution for 30 min in a rotating desiccator heated to 50 °C. Dried film was hydrated with buffer (see the next section for details) and briefly bath-sonicated to ensure

complete solubilization. This DOPC/CNT complex was then used to hydrate a dried PBD-PEO film to obtain a final polymer concentration of 5 mg·mL^{-1}. The solution was then heated to 70 °C and stirred for 1 h, then it underwent 10 cycles of the freeze-thaw treatment, followed by extrusion through a 400 nm polycarbonate filter. Finally, polymersomes were separated from unincorporated CNTPs with size-exclusion chromatography on an 8 cm long Sepharose CL-6B column. Purified vesicles were characterized with dynamic light scattering (Zetasizer Nano-ZS90, Malvern Instruments) with each measurement containing an average of at least 10 individual runs. DOPC and DOPC-CNTP liposomes were made as described previously [30].

Direct estimation of diblock copolymer/phospholipid concentration by a colorimetric assay.

The amount of membrane amphiphile present in samples was measured using a colorimetric assay that was used previously for lipids [31] and diblock copolymers [32]. Briefly, 200 μL aliquots of samples were dried for 15 min in a rotating desiccator heated to 50 °C. The dried samples were then solubilized with 2 mL of chloroform, followed by the addition of 2 mL ammonium ferrothiocyanate. This solution was vortexed vigorously for 1 min and allowed to separate on the bench top. The bottom chloroform layer was carefully extracted with a Pasteur pipette and the absorbance was measured at 510 nm (488 nm) to quantify the polymer (lipid) mass. This analysis used a calibration curve prepared from samples of known lipid and polymer concentrations.

4.3 CNTP incorporation and characterization.

We chose PBD_{22}-PEO_{14} (PBD-PEO 1800) diblock co-polymer (MW PBD:PEO of 1200:600) as a membrane matrix since it forms 10-12 nm thick polymer bilayers that provide an ideal match for CNTP length. Block-copolymer membranes were previously used to incorporate a variety of membrane proteins, such as aquaporin Z [33], ATP synthase [34], GPCRs [35], and OmpF porins [36]; therefore, we expected that CNTPs would also incorporate into this membrane (Figure 4.2). To insert CNTPs into the block-copolymer membranes, we modified previously developed procedures for inserting CNTPs into lipid matrices [14, 30], by adding elevated temperatures and constant stirring necessary for PBD-PEO 1800 to form vesicles.

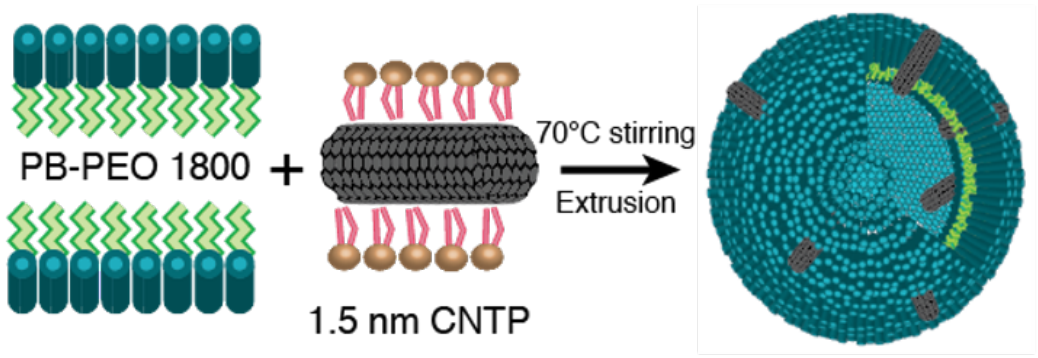

Figure 4.2: Schematic of the CNTP incorporation into PB-PEO 1800 polymersomes.

Cryogenic TEM measurements of CNTP-polymersomes

Specimens were prepared for cryogenic (cryo) TEM specimens by placing a 3 μL drop of sample onto a 200 mesh copper TEM grid coated with lacey carbon film (EMS). Grids were glow discharged prior to use (EasiGlow, Ted Pella). Grids were inserted into an FEI Vitrobot Mark IV (FEI, Hillsboro, OR) maintained at room temperature and 70% relative humidity and blotted with filter paper [blot time: 1 s, relaxation time: 1 s, blotting force: 1 (unitless parameter)]. The grid was then rapidly plunged into liquid ethane. All specimens were stored and handled under liquid nitrogen after vitrification. Specimens were imaged under low-dose conditions in an FEI Titan 80-300 Environmental TEM equipped with a field emission electron gun and operated at 300 kV. Specimens were transferred into the TEM while maintaining cryogenic conditions (-176 °C) by using a Gatan 626 cryo-TEM holder. Images were captured with an UltraScan 1000 2k × 2k charge capture device (CCD) camera (Gatan, Inc.) operated via Digital Micrograph (Gatan, Inc). Once recorded, images that were processed using ImageJ.

Small angle X-ray scattering.

In order to determine whether the lipid and copolymer phase-separate in the CNTP-polymersomes, we collected small angle X-ray scattering (SAXS) from: pure polymersomes, pure liposomes, and CNTP-polymersomes in solution with concentration of 10, 10, and 12.9 mg mL^{-1}, respectively. Each suspension was pipetted into a capillary tube at beamline 4-2 at the Stanford Synchrotron Radiation Laboratory [37] and exposed to 12.5 keV X-rays. The scattered intensity from the vesicles was collected in the q-range: 0.02 Å^{-1} $< q <$ 1.5Å^{-1}, where q is defined as the magnitude of the scattering

vector [38]. Sixty frames (1s each) were collected using a beam size of 0.3 mm × 0.3 mm whilst oscillating the solution to thwart beam damage. There was little difference between the 60 different SAXS frames collected from each sample. Therefore, all frames were averaged to increase the signal-to-noise ratio of the data.

NIR absorption

Near-IR (NIR) absorption was measured using a Cary 4000 UV-vis/NIR spectrometer (Agilent). Briefly, 100 μL of vesicles were aliquoted into glass vials and dehydrated in a rotary evaporator set to 55 °C until completely dry. Dried film was then resuspended with 200 μL of D_2O water and bath-sonicated until the sample solution appeared uniformly turbid. The absorbance was measured from 1800 to 200 nm at a scanning rate of 600 nm s^{-1} and a time interval of 0.1 s. The absorbance in the S_{22} regime (900-1100 nm) [39] was selected and subtracted from measurements of polymer or lipid vesicles alone to determine the peak absorbance.

High-speed atomic force microscopy imaging of supported block-copolymer bilayers

All AFM imaging used a 1.5 mm diameter mica disk substrate glued on a glass rod of the HS-AFM sample stage. Mica surfaces were freshly cleaved prior to sample deposition and a small aliquot of vesicles was placed on the sample with a pipette and incubated for 30 min at 70 °C. High-speed atomic force microscopy (HS-AFM) images of CNTPs were acquired in tapping mode at room temperature using an HS-AFM instrument (RIBM, Japan) equipped with ultrashort AFM cantilevers with custom-produced high-density carbon/diamond-like carbon tips (USC-F1.2-k0.15, NanoWorld, tip radius < 10 nm). The electron beam deposited carbon tips (radius < 10 nm) were also fabricated on the AFM cantilevers with the Zeiss Crossbeam 1540. For all imaging studies the HS-AFM fluid cell was filled with 120 μL of phosphate buffered saline. 128 × 128 pixel images were collected from a 200 × 200 nm area at a scan rate of 2 frames per second. The home-built Matlab2015 (MathWorks, Natick, MA) code was used to convert the raw HS-AFM images to ImageJ (National Institutes of Health, Bethesda, MD) stacks for further processing.

Raman spectroscopy of CNTPs.

Raman spectra of dried CNTP aliquots were collected using a Nicolet Almega XR micro-Raman spectrometer at laser wavelengths of 633 nm and

laser power was kept below 100 W cm^{-1} to avoid heating the samples.

proton permeability

Polymersomes and CNT-polymersome proton transport measurements followed the protocols previously described for measuring proton transport in DOPC-CNTP liposomes [15]. Briefly, polymersome-CNTP vesicles containing 10×10^{-3}M of the pH-sensitive HPTS dye in buffer (150×10^{-3}M NaCl, 30×10^{-3}M KCl, and 10×10^{-3}M HEPES, pH of 7.5). Separately, 2 mL of the same buffer adjusted to pH 6.9 was placed in a cuvette inside a fluorimeter (Fluoromax 4, Horiba) and equilibrated to room temperature for at least 5 min with constant stirring. 70 μL vesicle aliquots were added to the cuvette and the instrument recorded a time trace of the HTPS fluorescence (Em/Ex: 450/514 nm). Proton permeability was determined from these kinetics as described previously [15].

water transport

Water permeabilities of CNTP-polymersomes or control polymersomes were determined using a stopped-flow instrument (SFM2000, BioLogic) and previously described protocols [16]. Briefly, vesicles were rapidly mixed in the stopped-flow instrument with a hypertonic buffer solution composed of 10×10^{-3}M HEPES (pH 7.5) and varying concentrations of HPTS (from 6.25 to 40×10^{-3}M) or poly(diallyldimethylammonium chloride (PDADMAC) (0.5%-4% (w/v)). The osmolarity of each buffer was verified with a freezing-point osmometer (Osmomat 3000, Gonotec) prior to the experiment. Light scattering data were acquired in the time interval between 50 and 500 μs, at 90°C scattering angle, and a measured dead time of 0.7 ms. For each osmolyte concentration, we averaged at least three individual runs and the resulting kinetics were used to calculate the water permeability as described previously [16]. The reported value for water permeability was calculated from an average of three different vesicle preparations.

Chemiluminescence assay.

CNTP-polymersomes containing 50 U mL^{-1} of HRP (final encapsulation efficiency 1.3%) were formed in a 10×10^{-3}M HEPES buffer at pH 7.8. To prevent damage to the enzyme, we used four freeze-thaw cycles in the vesicle preparation instead of the 10 listed above. Once extruded and separated from unencapsulated protein with size exclusion chromatography, vesicle fractions were collected, combined, and used immediately. In a typical experiment, 100 μL of CNTP-polymersomes loaded with HRP were added to a cuvette

containing 1.8 mL of 10×10^{-3}M HEPES, pH 7.8. After 5 min, 40 μL of 200×10^{-3}M luminol sodium salt and 66.7 μL of 30% hydrogen peroxide was added, in separate steps, to begin the reaction and luminol chemiluminescence signal at 432 nm was recorded in a Fluoromax-4 fluorometer with the excitation pathway blocked and under constant stirring.

Ca^{2+} vesicle docking assay.

CNTP-polymersomes were formed in a 10×10^{-3}M HEPES buffer, pH 7.2, that also contained 100×10^{-6}M of calcium indicator dye Fluo-4 pentapotassium salt (final encapsulation efficiency 6.7%). DOPC liposomes that incorporated 60×10^{-3}M $CaCl_2$ were formed. After extrusion and size-exclusion chromatography purification both types vesicles were kept in a water bath at 23.6 °C. In a typical experiment, 100 μL of polymersome and liposome vesicles were pipetted into 2.8 mL of 10×10^{-3}M HEPES pH 7.2 in a cuvette in a fluorimeter (Fluoromax-4, Horiba), and Fluo-4 fluorescence kinetics (Ex:494/Em:514) was recorded under constant stirring and strict temperature control.

Vesicle fusion assay.

CNTP-polymersomes, CNTP-liposomes, pure polymersomes, and pure liposomes were formed in 10×10^{-3}M HEPES buffer, pH 7.2. Pure polymersomes and liposomes contained 5% (w/w) rhodamine B DOPE such that rhodamine B fluorescence is self-quenched. In a typical experiment 100 μL of pure liposomes and 100 μL of CNTP-liposomes were added to a cuvette with 1.8 mL 10×10^{-3}M HEPES buffer (pH 7.2). Kinetics of membrane exchange was evaluated by observing dequenching of rhodamine B fluorescence (Ex./Em.: 543/565 nm) under constant stirring.

4.4 Results and discussion

Cryogenic TEM (cryoTEM) images of CNTP-polymersomes (Figure 4.3) contain linear features within the polymersome membrane that likely correspond to CNTPs inserted in the membrane. These images also share broad similarity with the cryoTEM images that we reported previously for CNTPs inserted into lipid bilayers [13], although the overall contrast between the nanotube and polymer matrix was significantly weaker (See Figure 4.4). Since CNTPs were synthesized using lipid-assisted sonication cutting, a small amount of DOPC lipid was introduced into the polymersomes with the CNTPs. Although lipids and block copolymers readily form mixed membranes, we have performed SAXS studies to test whether this additional lipid component was

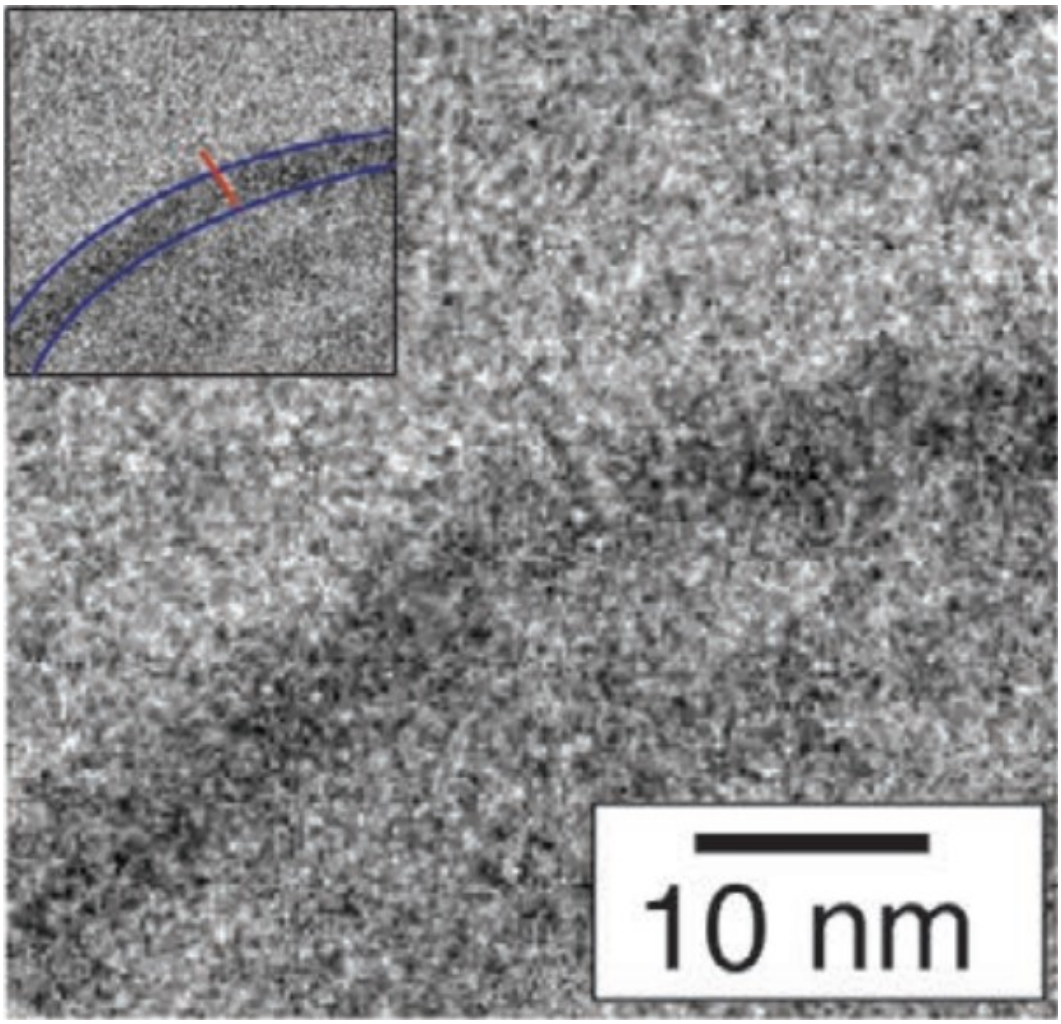

Figure 4.3: Cryogenic TEM image of a polymersome wall with CNTPs. Inset highlights the location of the CNTP in the image.

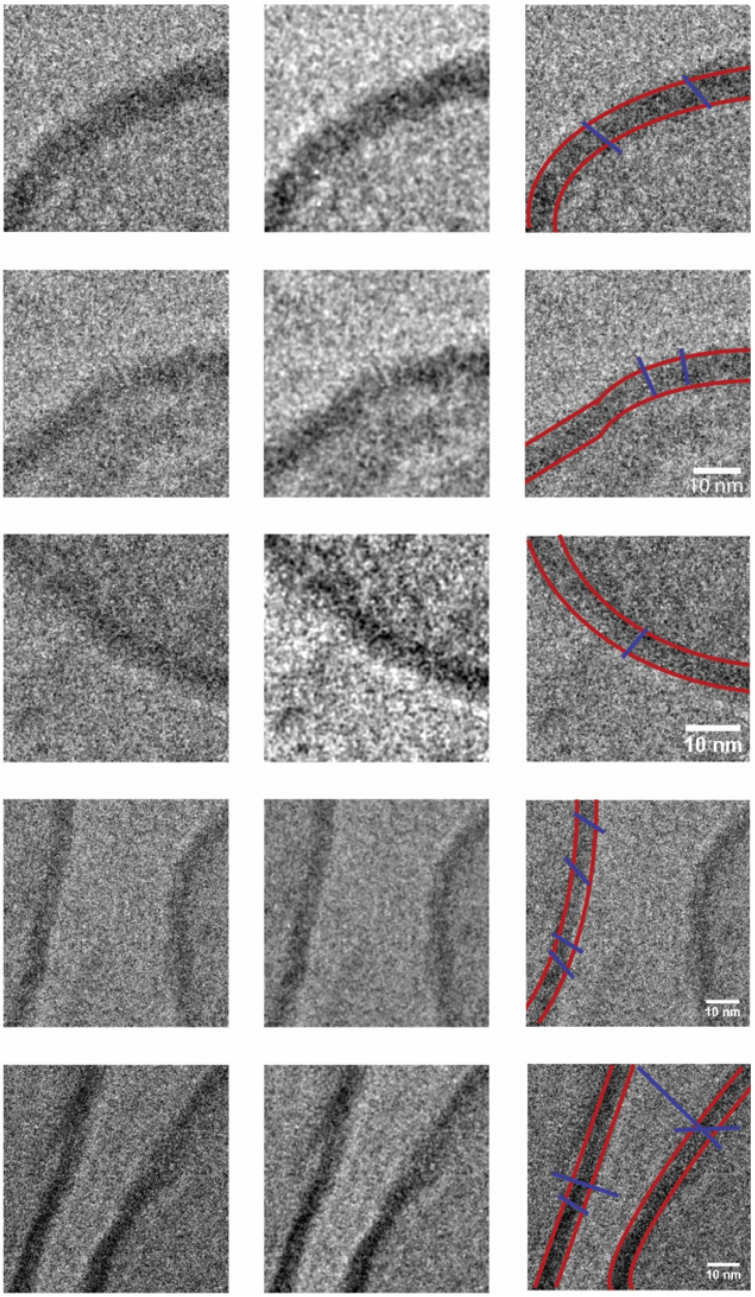

Figure 4.4: Cryogenic TEM image of CNTPs in polymersome membranes from different vesicles. The raw images are in the left column, images in the middle column were processed with a smoothing algorithm and then contrast was adjusted in ImageJ. Right column highlights the boundaries of the bilayers (red) and CNTPs (blue).

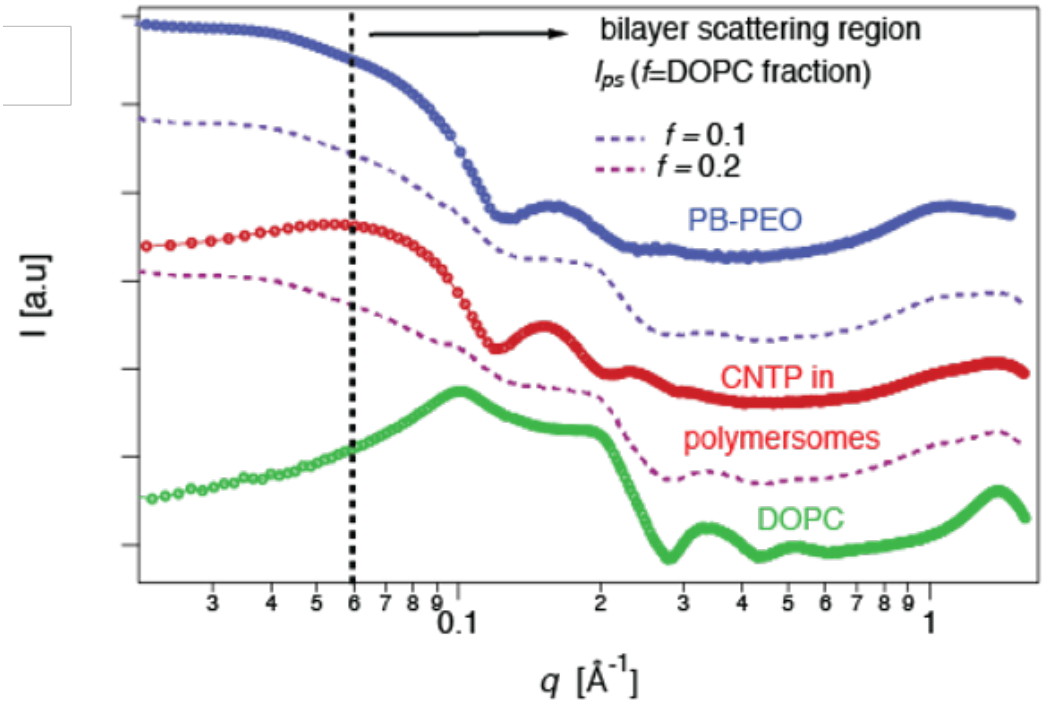

Figure 4.5: A log-log plot of the SAXS profiles for PB-PEO polymersomes (blue), DOPC liposomes (green) and CNTP-polymersomes (red). Dashed lines show predicted SAXS profiles for phase-separated PB-PEO and DOPC bilayers for lipid fraction of f = 0.2 (dark purple) and f = 0.1 (violet).

forming phase-separated lipid domains in the membrane that could sequester CNTPs.

SAXS profile of the CNTP-polymersome vesicles was clearly distinct from the profiles of the vesicles created with pure PB-PEO or DOPC (Figure 4.5). Moreover, as the scattered intensity from non-interacting phases should be additive, we can expect the scattered intensity from vesicles containing phase-separated PB-PEO and DOPC bilayers should represent a linear combination of the scattering signals of each component in the q-range where the characteristic sizes of each of the bilayers scatter (this assumption would not be valid at lower range of q-values that would reflect the overall size of each phase). The SAXS profile obtained for CNTP polymersomes was distinctly different from those of pure polymer or lipid vesicles and cannot be obtained from a linear combination of those profiles (Figure 4.14, dashed lines), arguing that in our samples PB-PEO and DOPC bilayer phases do not phase-separate into distinct polymer and lipid domains.

To characterize the morphology and dynamics of CNTPs in the polymer-

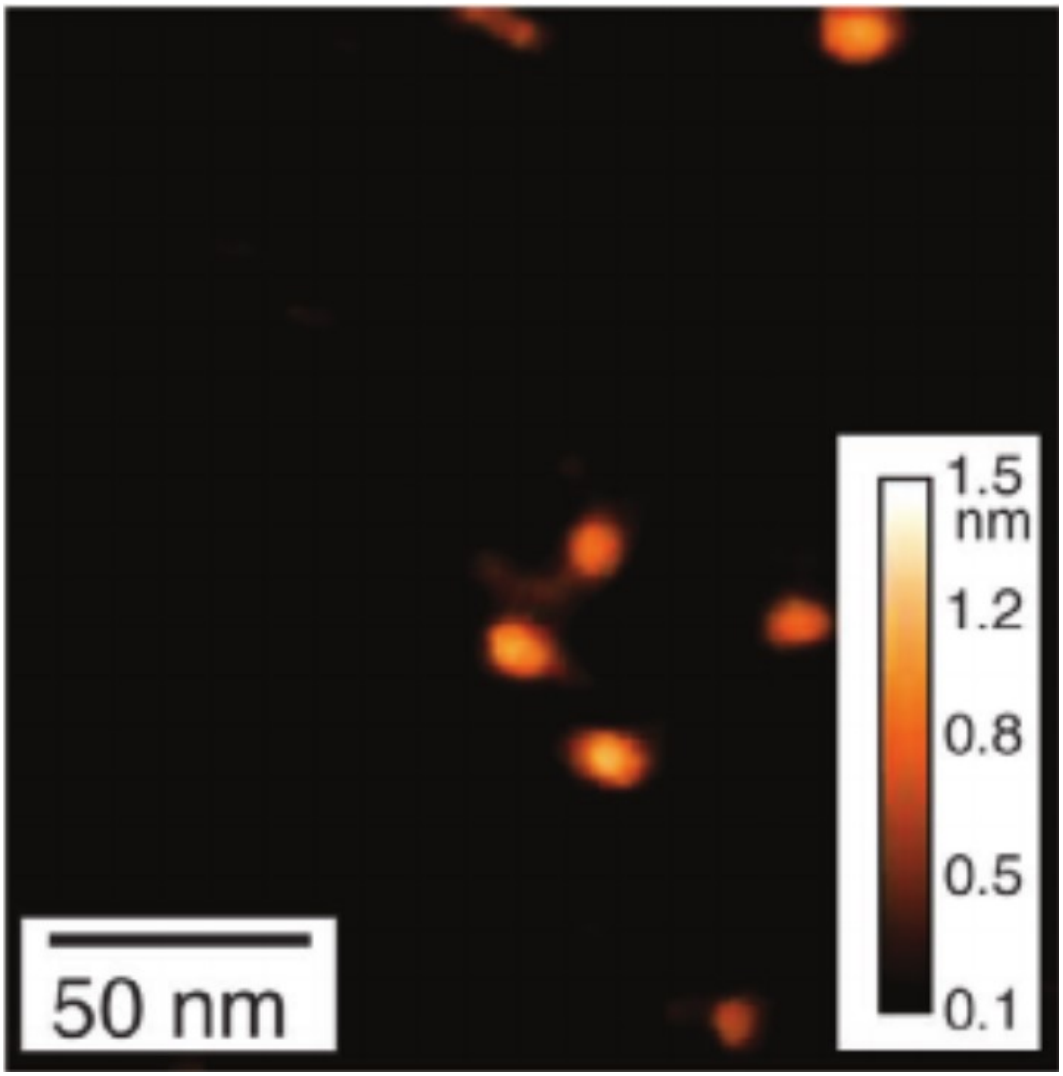

Figure 4.6: A frame from a HS-AFM movie of the CNTP/polymersome membrane fused onto a mica surface. Image shows several CNTPs protruding above the polymersome membrane plane.

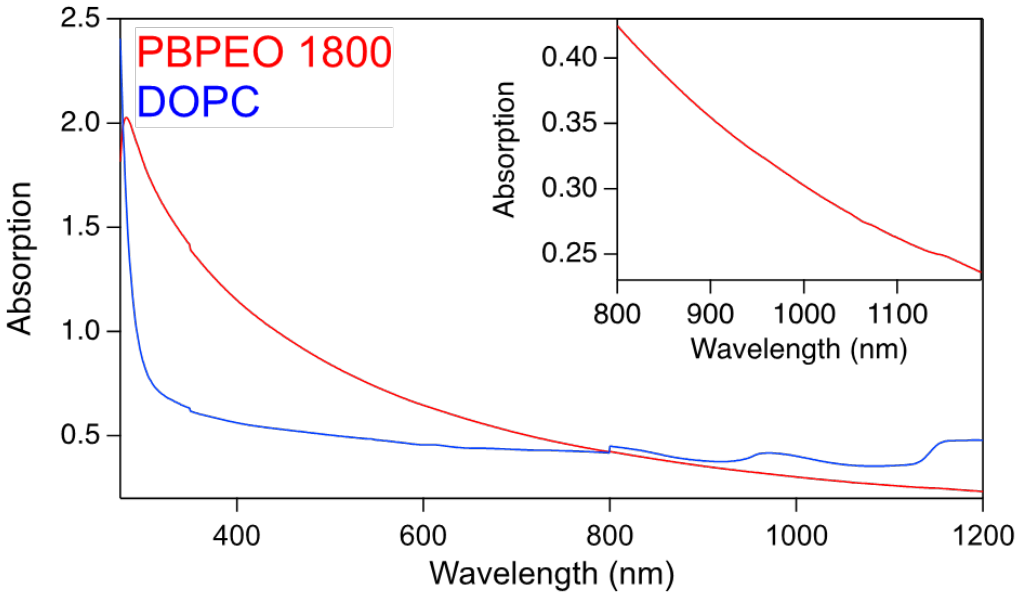

Figure 4.7: Visible and near infrared absorption obtained from PBPEO 1800 copolymer and DOPC vesicles. The presence of higher absorption at lower wavelengths in PBPEO 1800 (red) is also in agreement for absorbance spectra obtained from lipid vesicle samples (blue). The inset highlights that polymersomes do not show any characteristic peaks in the spectral region that is important for identifying S_{22} signals from CNTPs.

some membrane further, we fused the CNTP-containing polymersomes to a mica surface and imaged the resulting supported bilayer with HS-AFM. We previously showed that HS-AFM not only can visualize CNTPs in lipid bilayers, but also can capture real-time dynamics of CNTP diffusion in the bilayer plane [40]. HS-AFM movies of control polymersome layers showed flat layer morphology devoid of any sharp features. These movies and other AFM images indicated that polymersome bilayers had smooth morphology and were approximately 9 nm thick, which agrees with the ca. 7-11 nm thicknesses observed in the cryo-TEM images. In contrast, HS-AFM images of CNTP-containing polymersomes reveal multiple sharp features protruding by on average 1-2 nm above the membrane plane, which we attribute to the CNTPs (Figure 4.6).

To quantify the CNTP content in CNTP-polymersome samples, we measured the NIR absorbance in the 1050 nm region, which corresponds to the S_{22} transitions in carbon nanotubes. This spectral region is convenient because water and block copolymers that we used have minimal signal in this range (See Figure 4.7), simplifying background subtraction. CNTP-polymersome

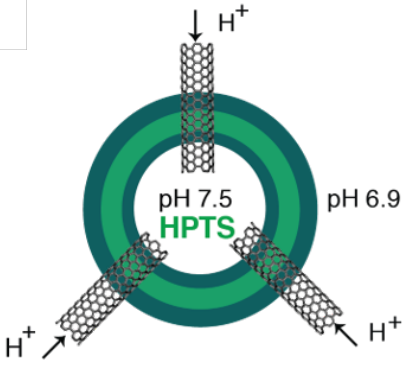

Figure 4.8: Schematic of the proton transport through CNTPs in polymersome membranes experiment.

samples showed a clear adsorption peak in this region, which was absent in control samples; moreover, the magnitude of the S_{22} peak increased with the increased loading of CNTPs into the polymersomes, confirming that this signal originated from the CNTPs. To quantify the number of CNTPs in the polymer membrane we compared the magnitude of the S_{22} signal with the similar measurement performed on previously calibrated vesicle samples that contained CNTPs inserted into pure lipid bilayers. We then used this ratio of NIR signals (corrected for the difference in surface area of liposomes and polymersomes) to calculate the number of CNTPs present in polymersomes. Surprisingly, this comparison revealed that polymersome samples had 4 times more CNTPs compared to lipid samples formed under the same conditions. We attribute this effect to a better match between CNTPs length and the polymersome bilayer thickness. Furthermore, lower stretching moduli of polymer bilayers, compared to their lipid counterparts, may also contribute to favorable CNTP insertion. We also note that polymersome layers were previously shown to support nearly close-packed arrangement of artificial membrane channels [8], suggesting that future work could potentially increase the CNTP loading.

Proton conductance measurements provide another way to characterize the number of CNTPs present in the polymersome membranes. When CNTPs-polymersomes were loaded with pH-sensitive HPTS dye in their lumen and exposed to a small pH gradient (Figure 4.8), we observed rapid pH equilibration (Figure 4.9) confirming that CNTPs in the polymer membrane serve as efficient proton transport conduits. Control polymersomes without CNTPs exhibited much slower pH equilibration kinetics; this is similar to our previous measurements of proton transport in CNTPs in lipid bilayers [15] and indi-

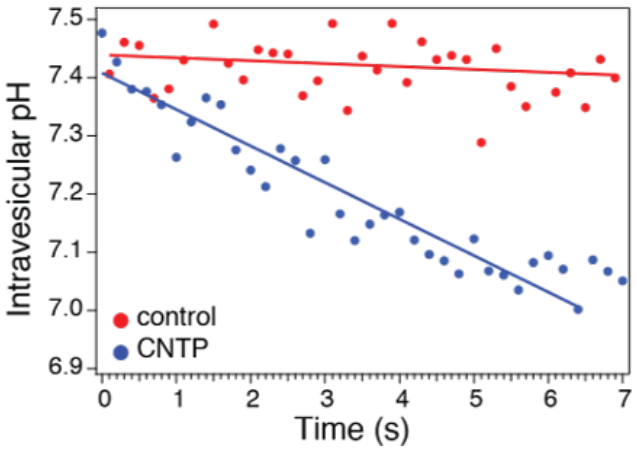

Figure 4.9: Proton transport through CNTPs in polymersome membranes. Initial time traces of the lumen pH values of polymersomes after pH of the outside solution decreased from 7.5 to 7.0.

cates that the bulk of the proton flux in this system indeed flows through the CNTPs. Thus, it was not surprising that increased CNTP loading, quantified by an increase in S_{22} adsorption (Figure 4.10), produced a corresponding increase in the proton flux through the CNTP polymersomes (Figure 4.11). The unitary CNTP proton conductance $0.73{\times}10^{-7} \pm 0.41 \times 10^{-7}$ nS determined from these measurements (as the slope of the linear fit through the data on the Figure 4.9) is within a factor of 3 of the unitary proton conductance value of $1.80{\times}10^{-7} \pm 0.69 \times 10^{-7}$ nS of CNTPs in lipid bilayers [15]. This result could be expected, as the proton conductance rate primarily reflects the arrangement of the water hydrogen bonding pattern in the nanotube, but also can reflect the different nature of the surrounding membrane matrix.

Our previous stopped-flow measurements of water transport through CNTPs embedded in lipid membranes showed that they were highly efficient water conductors [16]. Here, we used similar protocols to investigate water transport through CNTPs in polymersomes (Figure 4.12 - 4.14). Like lipid vesicles, polymersome membranes are susceptible to complex osmotically induced shape changes, as has been previously reported for diblock polymersomes [41]. Thus, subtraction of the background water permeability of the polymersomes is not trivial in this case. Indeed, stopped-flow kinetics recorded after we subjected PBD-PEO 1800 polymersomes to an osmotic gradient (Figure 4.13) revealed that instead of following a single-exponential kinetics characteristic of gradual volume change, light scattering traces showed two distinct single-exponential kinetics regions, separated by a "shoulder" region (Figure 4.13). Similar

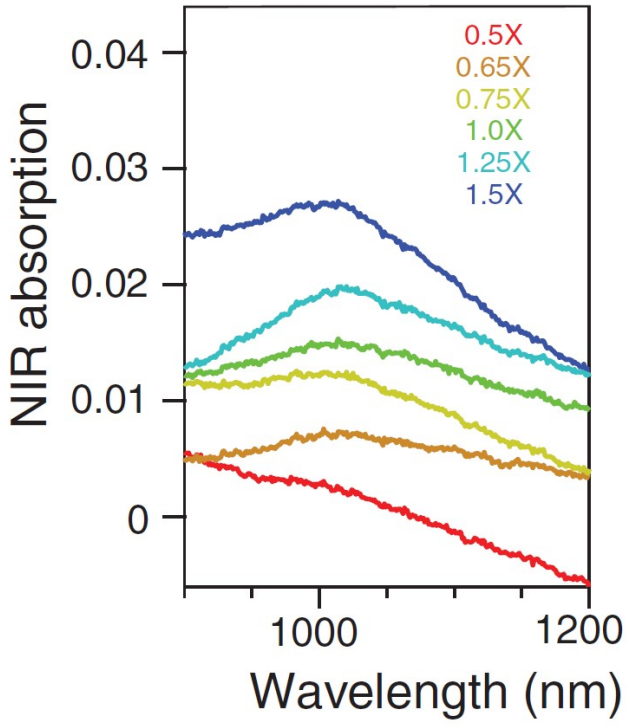

Figure 4.10: Optical properties of CNTPs. NIR absorption spectra in the S_{22} regime for increasing CNTP loading (as indicated in the legend) in CNTP-polymersomes.

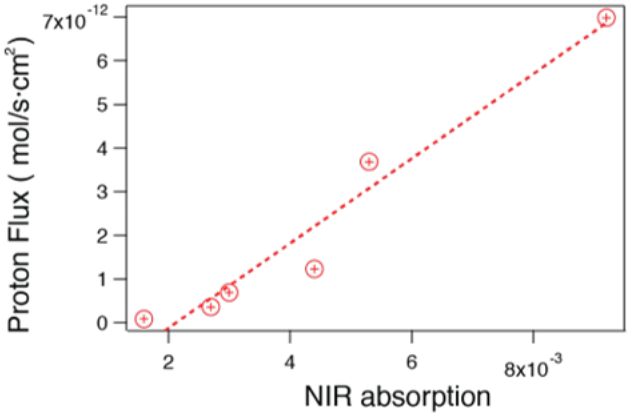

Figure 4.11: A plot of proton flux in CNTP-polymersomes as a function of S_{22} NIR absorption. Dashed line indicates a linear fit through the data.

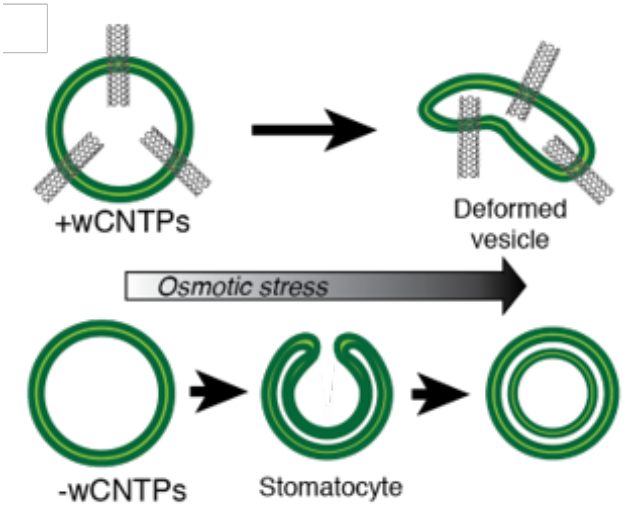

Figure 4.12: Schematics showing different polymersome response to osmotic stress depending on the presence of CNTPs.

stopped-flow kinetic traces have also been previously recorded for DODAB vesicles [42]. As the osmotic stress increases, the location of the inflection point of the shoulder region shifts to earlier times (see Figure 4.15, 4.16). Following the models described in the literature, we speculated that osmotic response of polymersomes involved initial shrinkage followed by a structural transition to a deformed shape-most likely a variant of the "stomatocyte" shape-which then shrinks further as water transport across the membrane equalizes the osmotic imbalance (Figure 4.12). Thus, we chose to use the first exponential region of the kinetic trace to extract the background polymersome water permeability. Our measured vesicle water permeability of ca. 30 μm s^{-1} is within the range of water permeability values reported for diblock copolymers, 2.5 [43]-189.7 μm s^{-1} [44], even though a direct comparison with other studies may be complicated because the water permeability may be influenced by differences in aqueous buffer conditions and polymer chemistry.

When the polymersomes containing CNTPs were subjected to different levels of osmotic stresses, they showed much faster shrinkage kinetics and no clear shoulder was observed in the stopped-flow curves (Figure 4.13, 4.14) with only the lowest osmotic stress traces showing hints of the "stomatocyte" transition behavior. These results suggest that in the presence of a large number of CNTPs, which enable much faster water escape from the vesicle lumen, the "stomatocyte" shape transition is kinetically suppressed. We speculate that the transport behavior of CNTP-laden polymersomes is governed by a topolog-

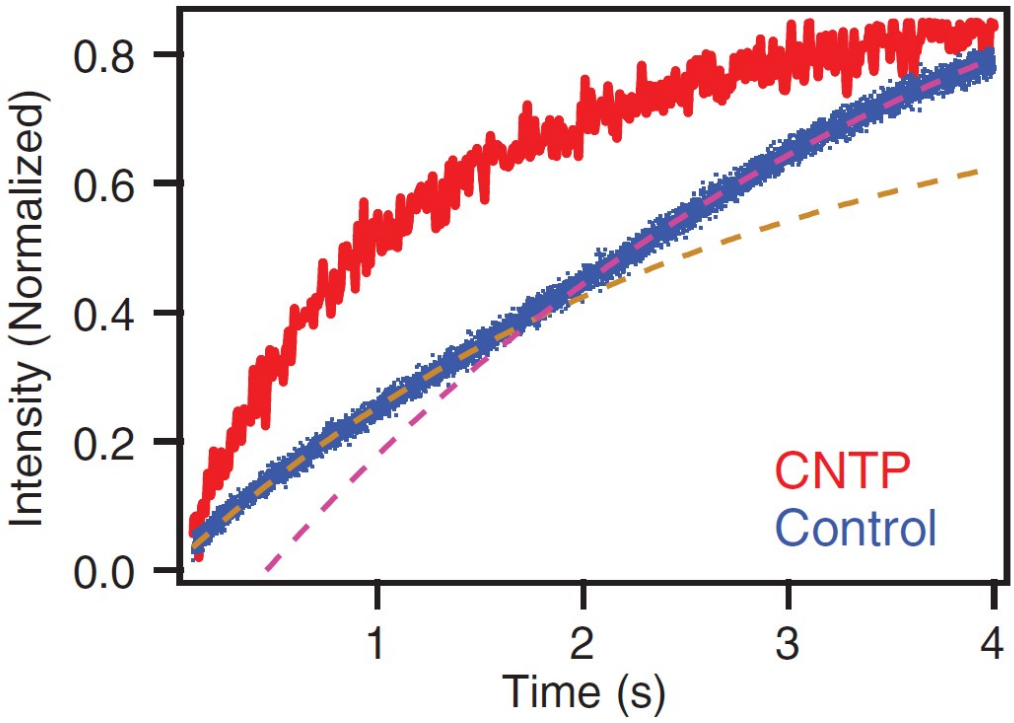

Figure 4.13: Water transport through CNTPs in polymersome membranes. Comparison of water transport kinetics from light scattering traces of hyperosmotic shocks of 0.5% PDADMAC acting on polymer vesicles with CNTPs and control vesicles without CNTPs, with two different fits (dashed lines) that approximate the general shape in the control trace.

ical transformation, characterized by division of polymersome compartments consistent with continuous shrinkage that we observe. Such proposed mechanism is consistent with the previous observations and an elastic model proposed by Boroske and co-workers [45]. Specifically, the enhanced water flow can generate positive spontaneous curvature, thus providing conditions for the budding and fission of small, daughter vesicles.

Factors driving shape deformations of liposomes and polymersomes subject to hypertonic stresses are largely understood in terms of minimal bending energy configurations of vesicles under conditions of reduced volume, $v = \frac{V}{4\pi R_0^3/3} < 1$ where R_0 corresponds to the radius of an equivalent sphere of area $S = 4\pi R_0^2$ [46, 47]. These treatments implicitly assume that the vesicles adopt equilibrium shapes, which correspond to the smallest possible value of the membrane bending energy [48] and produce shape diagrams depicting shape morphologies (e.g., oblate, prolate, dumbbell, and stomatocytes) as a function of reduced volume [49]. Experimentally however, significant devia-

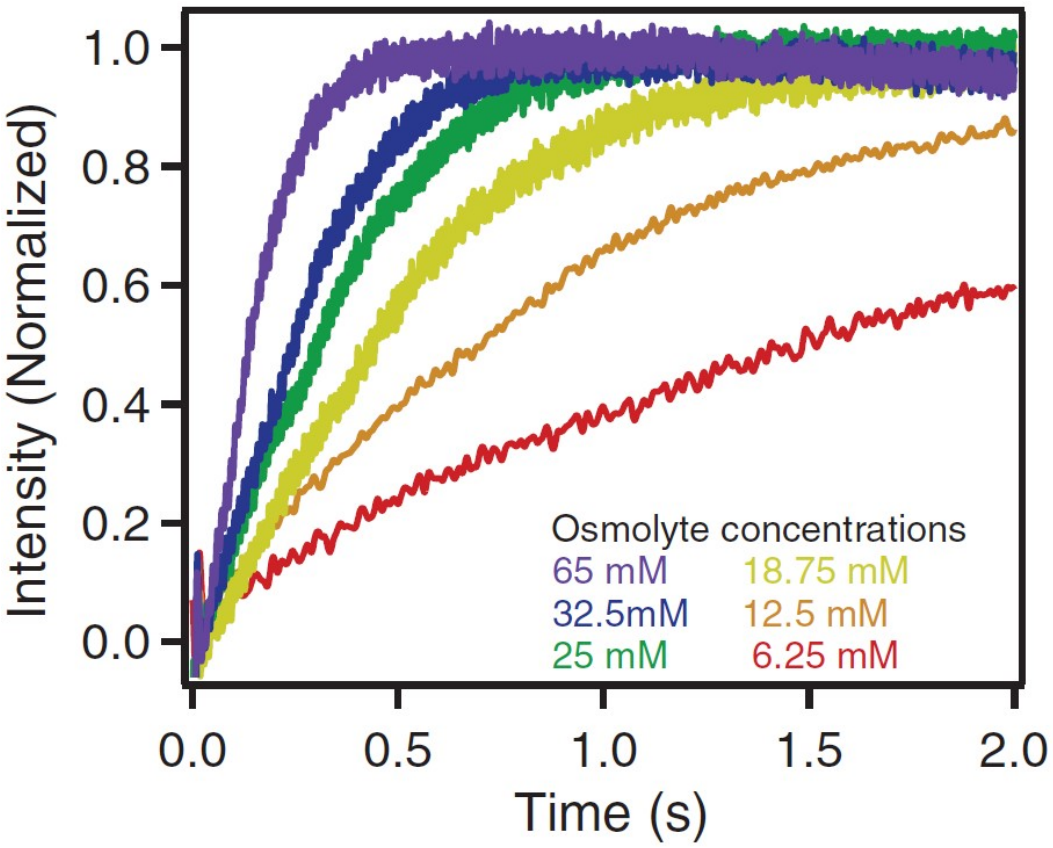

Figure 4.14: Light scattering traces taken from CNTP-polymersomes mixed with a series of HPTS concentrations.

tions from the predictions from these equilibrium shape diagrams, including budding, division, and tubulations, have also been observed most frequently associated with the generation of spontaneous membrane curvature through non-homogeneous distribution of membrane molecules [50, 51]. Our present observations are consistent with (but do not independently establish) the idea that the high concentration of CNTPs in polymer membranes may be accompanied by generation of spontaneous curvature and lateral phase separation, which promote budding and division over stomatocyte shape transformations under hypertonic conditions.

The unitary permeability of CNTPs, measured in the stopped-flow data experiments was $7.7\times10^{-14} \pm 2.5 \times 10^{-14}$cm^{3}s^{-1} (see Figure 4.17). These results agree with the water permeability that we previously reported for 1.5 nm diameter CNTPs embedded in lipid vesicles [16] (5.9×10^{-14}cm^3 s^{-1}), suggesting that the water transport mechanism in CNTPs is largely conserved

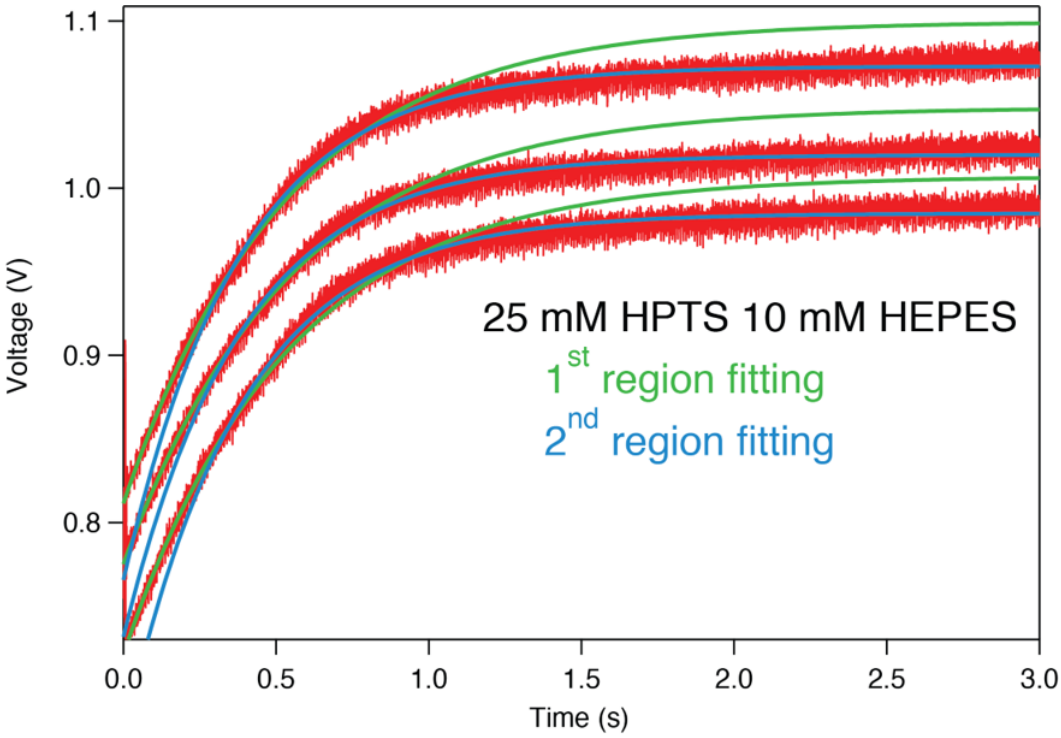

Figure 4.15: Light scattering traces monitoring water efflux from PBPEO 1800 vesicles triggered by exposure to HPTS osmolyte. Smaller osmolyte, such as HPTS, induces subtle deviations from ideal single exponential vesicle shrinkage curve. The kinetic follow two regions, each best fit by an independent exponential curve.

between the two-membrane scaffolds. Notably, unlike the behavior that we observed in the experiments with lipid vesicles [16], the water permeability was independent of the osmotic stress (see Figure4.17), which we attribute to the lower stretching moduli of the polymer membrane.

The experiments described in the previous sections show that CNTP channels in the walls of polymersomes facilitate mass exchange between the bulk solution and polymersome lumen. The small diameter of these channels should allow the CNTP-polymersomes to selectively encapsulate large molecules. This arrangement opens up a possibility to use CNTP polymersomes as nanoscale reactor compartments that contain and isolate some of the reaction components, whereas the other components can be delivered through the CNTPs. We first used this concept to demonstrate localized chemiluminescence production in CNTP-polymersomes. We placed an enzyme, HRP, into the lumen of polymersomes that contained CNTPs in their walls. At 44 kDa, HRP was

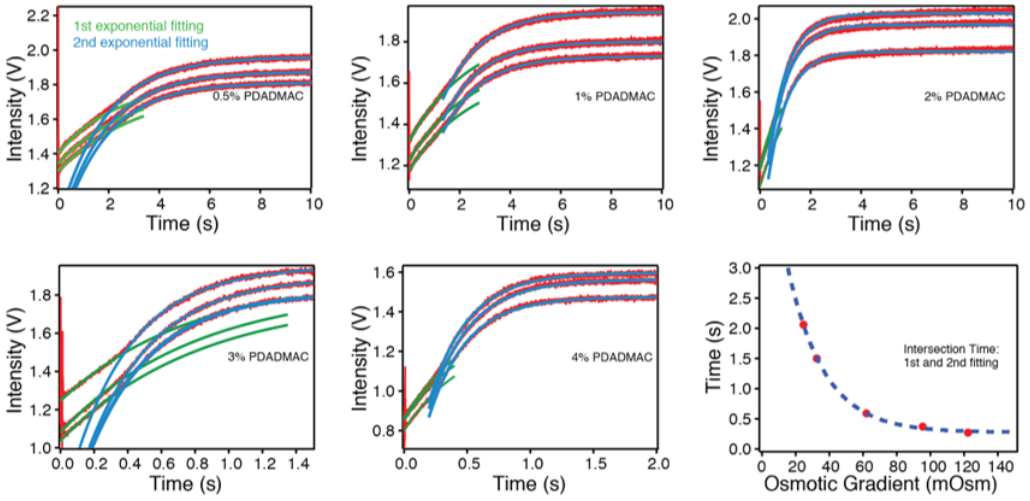

Figure 4.16: Light scattering traces monitoring water efflux from PBPEO 1800 vesicles triggered by exposure to PDADMAC osmolyte. Two-region kinetics is even more evident for a larger osmolyte such as PDADMAC. Right bottom graph shows that the intersection time as a function of osmotic gradient follows an exponential decal dependence (dashed line).

too large to pass through the CNTPs and thus remained trapped inside the lumen. However the 1.5 nm CNTPs were still large enough to transport small organic molecules [52] such as luminol and hydrogen peroxide that react with HRP to produce chemiluminescence. Indeed, when we added luminol and H_2O_2 to this sample, we observed a strong increase in the chemiluminescence (Figure 4.18). In contrast, when the polymersomes lacked the CNTP channels in the wall, addition of luminol and H_2O_2 did not increase chemiluminescence, showing that the encapsulated enzyme and the substrate remained spatially separated. These experiments demonstrated that 1.5 nm CNTPs facilitate the transport of small molecules and highlight the potential of CNTP-based nanoreactors to conduct cell-free reactions in the conditions that can simulate crowded intracellular environments.

Another interesting possibility is to use CNTPs as a nanoscale conduit for small-molecule exchange between two nanoscale compartments, mimicking the functionality of connexin channels, which form gap junctions that mediate direct cell-cell exchange of small molecules [5]. Our previous studies [13] indicated that CNTPs have a propensity to bridge two adjacent bilayers, forming a simplified mimic of a gap junction. Unfortunately, subsequent MD simulations also raised the possibility that this configuration could also facilitate membrane fusion after the nanotube bridges two lipid bilayers [53]. Thus, for

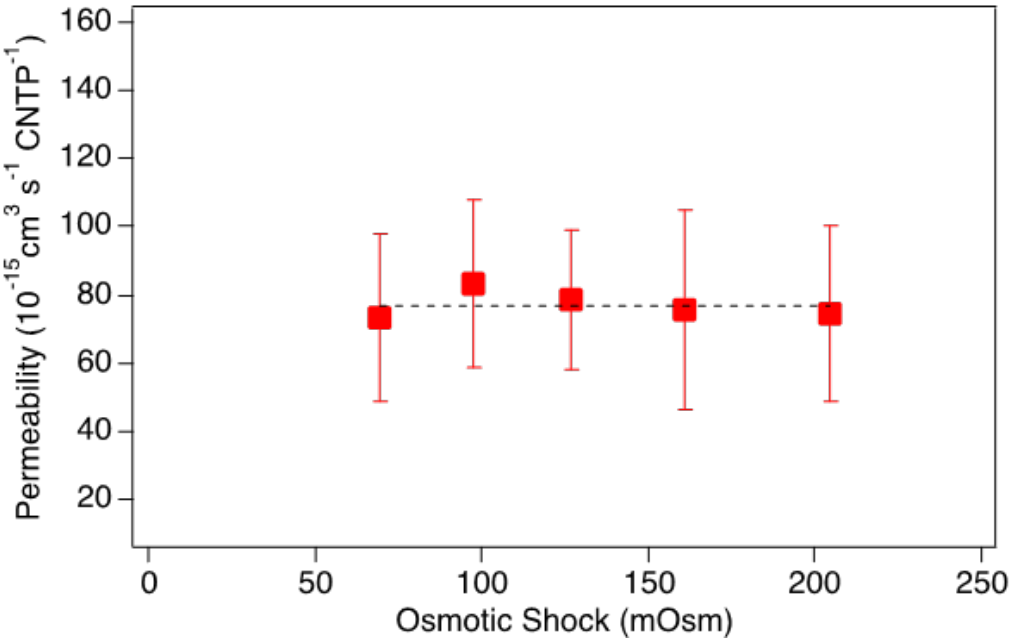

Figure 4.17: Water permeability through CNTPs in polymer vesicles as a function of applied osmotic shock. The values are reported from a series of three independent measurements on vesicles, with error bars representing the standard error of the mean. The unitary permeability value is independent of the osmotic shock, with the average value of $7.7 \times 10^{-14} \pm 2.5 \times 10^{-14} cm^3 s^{-1}$ (value is based on a weighted linear fit through the data, dashed line).

a CNTP to act as a gap junction mimic this undesirable process needs to be suppressed.

We hypothesized that if a nanotube bridges two dissimilar membranes, e.g. a polymer and a lipid membrane, fusion cannot occur. To test this hypothesis, we labeled a fraction of lipids with a self-quenching concentration of Rhodamine B-DOPE (see 4.19). Both the hemi-fusion and full fusion events [54] would lead to the dilution of the labeled lipid and dequenching of the dye. Indeed, we observed significant dequenching (Figure 4.19, top trace) when both populations of interacting vesicles (donor vesicles that contained CNTPs, and recipient vesicles that did not) were formed with lipid bilayers. In contrast, when we used CNTP-polymersomes as the donor vesicles, their interactions with the recipient liposomes did not show any dequenching (Figure 4.19, bottom trace) indicating that, as expected, CNTPs did not facilitate fusion between vesicles made of dissimilar types of bilayers.

To demonstrate CNTP-mediated material exchange between two separate vesicular compartments, we encapsulated a large Ca^{2+} indicator dye Fluo-4

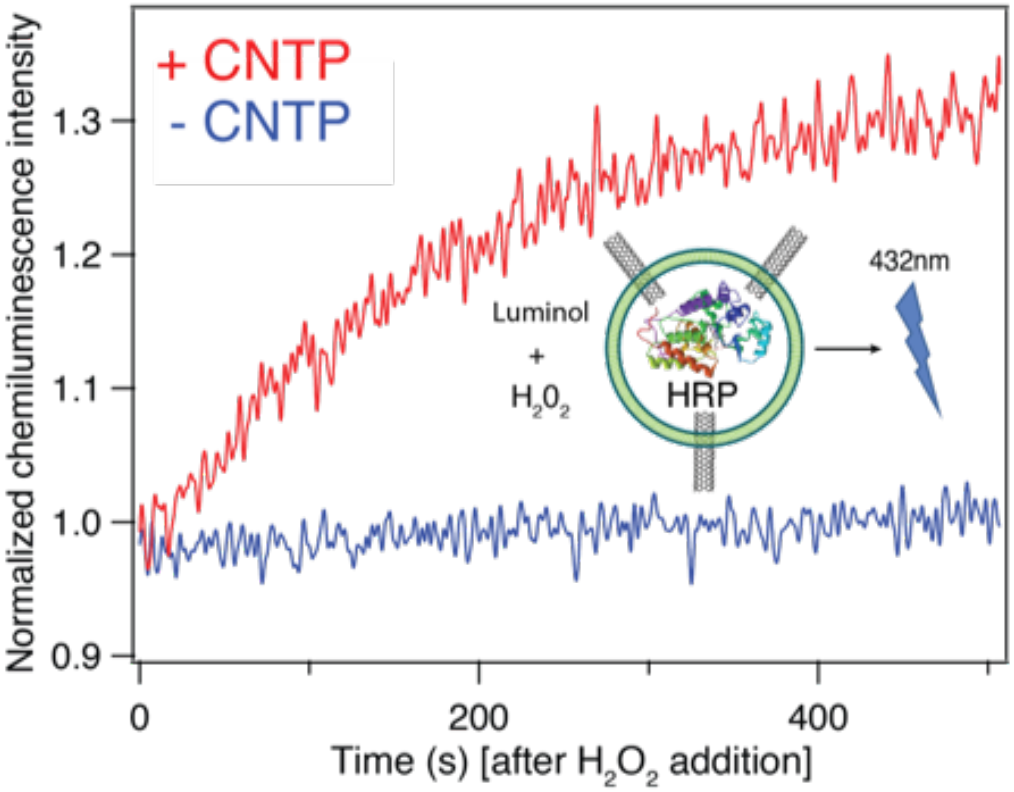

Figure 4.18: CNTPs as molecular exchange conduits. Chemiluminescence intensity recorded after adding luminol and hydrogen peroxide to the solution of polymersomes sequestering HRP enzyme in presence (red trace), and in absence (blue trace) of CNTPs in the polymersomes. Chemiluminescence signal was normalized to the signal recorded at the time t = 0.

(see Figure 4.20), which should not escape through 1.5 nm diameter CNTPs, in the polymersomes and added them to the lipid vesicles that contained 60×10^{-3}M $CaCl_2$. As expected, we observed a clear increase in the Fluo-4 emission after mixing these two vesicle populations (Figure 4.21), indicating that Ca^{2+} ions were able to diffuse into the polymersome interior through the CNTP connections formed between the two types of vesicles. We also observed a nearly identical increase in the Ca^{2+} reporter signal when we added a Ca^{2+} chelator EGTA to the extravesicular buffer solution (Figure 4.21, inset, green trace), indicating that the majority of the fluorescence increase was indeed caused by Ca^{2+} ions traveling from one vesicular compartment to another directly through the CNTP. Significantly when CNTPs were absent from the polymersomes, (Figure 4.21 inset, blue trace), we did not observe Fluo-4 signal

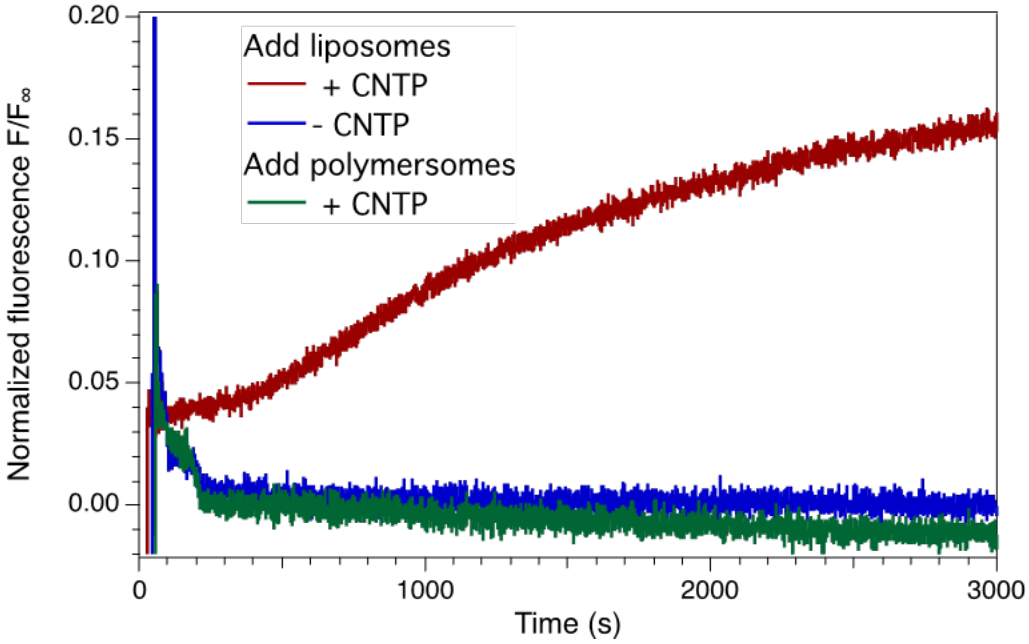

Figure 4.19: Membrane fusion assay. Normalized fluorescence traces obtained as liposomes containing rhodamine B labeled DOPE in the concentration just above self-quenching threshold were added to the liposomes and polymersomes with and without CNTPs (as indicated on the legend). The appearance of spiked traces after addition of rhodamine B labeled liposomes were due to disruption of the fluorescence signal by bubbles formed from pipetting. Fluorescence traces were normalized to the fully de-quenched fluorescence intensity, F_∞, recorded after disrupting all the vesicular content of the sample with Triton X-100.

increase, confirming that CNTPs were required for Ca^{2+} diffusion between the two vesicular compartments. These experiments also point to an interesting possibility for designing versatile CNTP gap junction mimics that could tune the transport selectivity simply by using nanotube porins of different diameter.

4.5 Conclusions

Our results show that CNTPs can insert into the block-copolymer layers to form completely synthetic mimics of biological membranes. CNTPs form transmembrane pores in polymersomes similar to those formed in lipid bilayers, and we show that these pores also have similar transport properties, establishing CNTPs as a universal membrane channel mimic. In particular, CNTPs

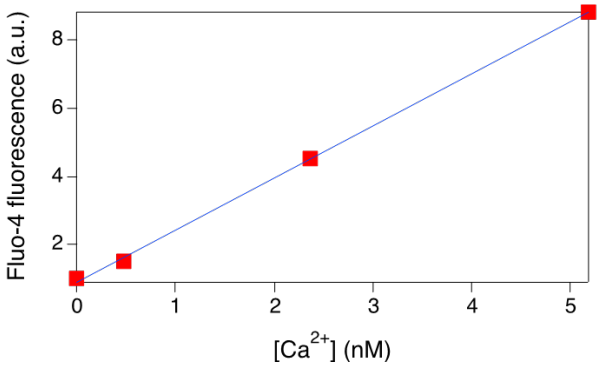

Figure 4.20: Fluo-4 fluorescence as a function of calcium ion concentration. Calibration curve obtained by adding small amounts of buffered Ca^{2+} (buffered with EGTA) to 270 nM of Fluo-4 in buffer.

maintain high proton and water permeability similar to those we reported previously for lipid membranes. The ability to use CNTPs in non-lipid membrane matrices allowed us to construct more sophisticated transport systems with CNTPs not only facilitating transmembrane transport, but also enabling gap-junction-like communication between different population of vesicles. We believe that these findings enable a number of interesting possibilities for designing new biomaterials systems. CNTPs of different size and length can be used to control transport selectivity, to regulate the communication between compartments of synthetic proto-cells or between proto-cell and live cells, and to facilitate sophisticated cargo exchange in these systems.

References

(1) Mulder, J., *Basic principles of membrane technology*; Springer Science & Business Media: 2012.

(2) Shannon, M. A.; Bohn, P. W.; Elimelech, M.; Georgiadis, J. G. *Science and technology for water purification in the coming decades. Nature* **2008**, *452*, 301.

(3) Werber, J. R.; Osuji, C. O.; Elimelech, M. *Nature Reviews Materials* **2016**, *1*, 16018.

(4) Shen, Y.-x.; Saboe, P. O.; Sines, I. T.; Erbakan, M.; Kumar, M. *Journal of Membrane Science* **2014**, *454*, 359–381.

(5) Alberts, B.; Johnson, A.; Lewis, J.; Raff, M.; Roberts, K.; Walter, P. **2007**.

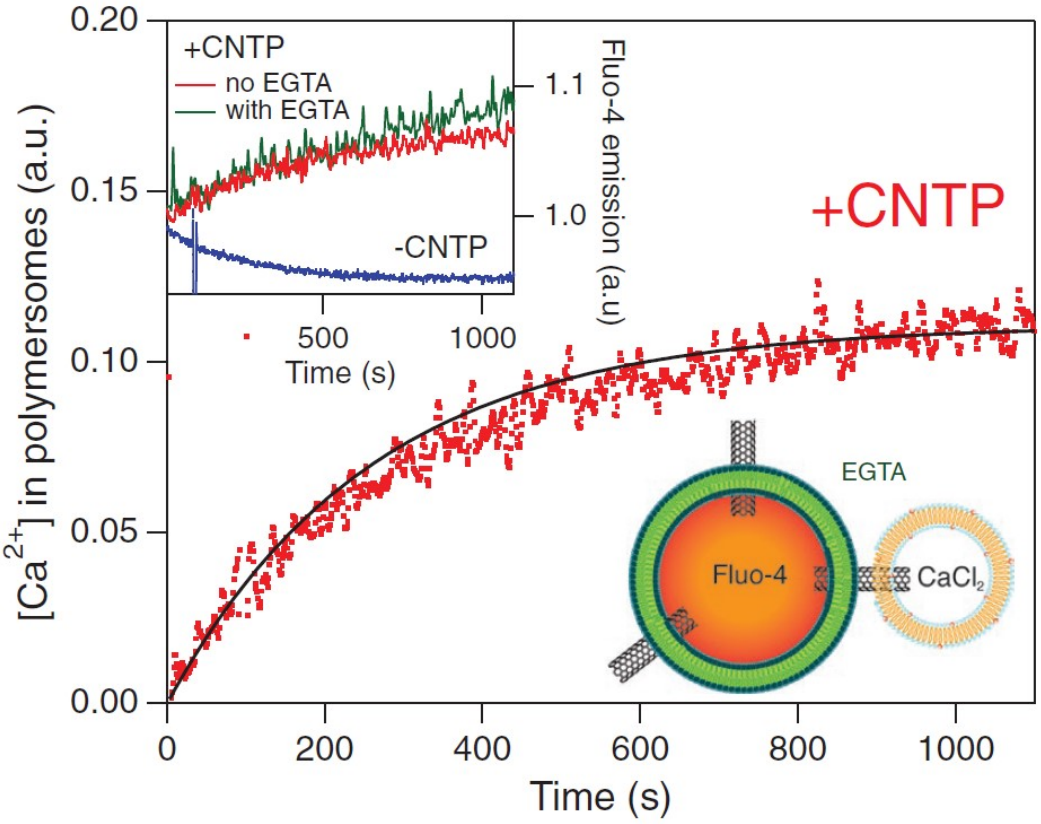

Figure 4.21: CNTPs as molecular exchange conduits for Ca^{2+}. A graph showing an increase in the differential fluorescence intensity of a Ca^{2+} reporter dye Fluo-4 encapsulated inside polymersomes caused by diffusion of Ca^{2+} ions from liposomes to polymersomes through CNTP conduits (inset schematics). The solid line corresponds to the fit of the data to a first order kinetics: $F = F_{max} \cdot [1 - exp(-\frac{t}{\tau})]$, where $\tau = 260 \pm 4$s. Inset: Fluo-4 fluorescence kinetics recorded in absence (blue trace) and in presence (red trace) of CNTPs in the polymersome wall. The green trace was recorded at the same condition as the red trace, except a Ca^{2+} chelator EGTA was added to the extravesicular buffer solution.

(6) Percec, V.; Dulcey, A. E.; Balagurusamy, V. S.; Miura, Y.; Smidrkal, J.; Peterca, M.; Nummelin, S.; Edlund, U.; Hudson, S. D.; Heiney, P. A., et al. *Nature* **2004**, *430*, 764.

(7) Barboiu, M.; Gilles, A. *Accounts of chemical research* **2013**, *46*, 2814–2823.

(8) Shen, Y.-x.; Si, W.; Erbakan, M.; Decker, K.; De Zorzi, R.; Saboe, P. O.; Kang, Y. J.; Majd, S.; Butler, P. J.; Walz, T., et al. *Proceedings of the National Academy of Sciences* **2015**, *112*, 9810–9815.

(9) Benke, B. P.; Aich, P.; Kim, Y.; Kim, K. L.; Rohman, M. R.; Hong, S.; Hwang, I.-C.; Lee, E. H.; Roh, J. H.; Kim, K. *Journal of the American Chemical Society* **2017**, *139*, 7432–7435.

(10) Langecker, M.; Arnaut, V.; Martin, T. G.; List, J.; Renner, S.; Mayer, M.; Dietz, H.; Simmel, F. C. *Science* **2012**, *338*, 932–936.

(11) Seifert, A.; Göpfrich, K.; Burns, J. R.; Fertig, N.; Keyser, U. F.; Howorka, S. *ACS nano* **2014**, *9*, 1117–1126.

(12) Howorka, S. *Nature nanotechnology* **2017**, *12*, 619.

(13) Geng, J.; Kim, K.; Zhang, J.; Escalada, A.; Tunuguntla, R.; Comolli, L. R.; Allen, F. I.; Shnyrova, A. V.; Cho, K. R.; Munoz, D., et al. *Nature* **2014**, *514*, 612.

(14) Tunuguntla, R. H.; Chen, X.; Belliveau, A.; Allen, F. I.; Noy, A. *The Journal of Physical Chemistry C* **2017**, *121*, 3117–3125.

(15) Tunuguntla, R. H.; Allen, F. I.; Kim, K.; Belliveau, A.; Noy, A. *Nature nanotechnology* **2016**, *11*, 639.

(16) Tunuguntla, R. H.; Henley, R. Y.; Yao, Y.-C.; Pham, T. A.; Wanunu, M.; Noy, A. *Science* **2017**, *357*, 792–796.

(17) Discher, D. E.; Eisenberg, A. *Science* **2002**, *297*, 967–973.

(18) Menger, F. M.; Gabrielson, K. D. *Angewandte Chemie International Edition in English* **1995**, *34*, 2091–2106.

(19) Nam, K. T.; Shelby, S. A.; Choi, P. H.; Marciel, A. B.; Chen, R.; Tan, L.; Chu, T. K.; Mesch, R. A.; Lee, B.-C.; Connolly, M. D., et al. *Nature materials* **2010**, *9*, 454.

(20) Stupp, S. I.; LeBonheur, V.; Walker, K.; Li, L.-S.; Huggins, K. E.; Keser, M.; Amstutz, A. *Science* **1997**, *276*, 384–389.

(21) Zhang, L.; Eisenberg, A. *Science* **1995**, *268*, 1728–1731.

(22) Tangorra, R. R.; Operamolla, A.; Milano, F.; Omar, O. H.; Henrard, J.; Comparelli, R.; Italiano, F.; Agostiano, A.; De Leo, V.; Marotta, R., et al. *Photochemical & Photobiological Sciences* **2015**, *14*, 1844–1852.

(23) Peters, R. J.; Nijemeisland, M.; van Hest, J. C. *Angewandte Chemie International Edition* **2015**, *54*, 9614–9617.

(24) Christian, D. A.; Tian, A.; Ellenbroek, W. G.; Levental, I.; Rajagopal, K.; Janmey, P. A.; Liu, A. J.; Baumgart, T.; Discher, D. E. *Nature materials* **2009**, *8*, 843.

(25) Carlsen, A.; Glaser, N.; Le Meins, J.-F.; Lecommandoux, S. *Langmuir* **2011**, *27*, 4884–4890.

(26) Discher, D. E.; Ahmed, F. *Annu. Rev. Biomed. Eng.* **2006**, *8*, 323–341.

(27) Discher, B. M.; Won, Y.-Y.; Ege, D. S.; Lee, J. C.; Bates, F. S.; Discher, D. E.; Hammer, D. A. *Science* **1999**, *284*, 1143–1146.

(28) Kang, M.; Tuteja, M.; Centrone, A.; Topgaard, D.; Leal, C. *Advanced functional materials* **2018**, *28*, 1704356.

(29) Gettel, D. L.; Sanborn, J.; Patel, M. A.; de Hoog, H.-P.; Liedberg, B.; Nallani, M.; Parikh, A. N. *Journal of the American Chemical Society* **2014**, *136*, 10186–10189.

(30) Tunuguntla, R. H.; Escalada, A.; Frolov, V. A.; Noy, A. *Nature protocols* **2016**, *11*, 2029.

(31) Stewart, J. C. M. *Analytical biochemistry* **1980**, *104*, 10–14.

(32) Al-Hanbali, O.; Onwuzo, N. M.; Rutt, K. J.; Dadswell, C. M.; Moghimi, S. M.; Hunter, A. C. *Analytical biochemistry* **2007**, *361*, 287–293.

(33) Kumar, M.; Grzelakowski, M.; Zilles, J.; Clark, M.; Meier, W. *Proceedings of the National Academy of Sciences* **2007**, *104*, 20719–20724.

(34) Choi, H.-J.; Montemagno, C. D. *Nano letters* **2005**, *5*, 2538–2542.

(35) May, S.; Andreasson-Ochsner, M.; Fu, Z.; Low, Y. X.; Tan, D.; de Hoog, H.-P. M.; Ritz, S.; Nallani, M.; Sinner, E.-K. *Angewandte Chemie International Edition* **2013**, *52*, 749–753.

(36) Meier, W.; Nardin, C.; Winterhalter, M. *Angewandte Chemie* **2000**, *112*, 4747–4750.

(37) Smolsky, I. L.; Liu, P.; Niebuhr, M.; Ito, K.; Weiss, T. M.; Tsuruta, H. *Applied Crystallography* **2007**, *40*, s453–s458.

(38) Glatter, O.; Kratky, O., *Small angle X-ray scattering*; Academic press: 1982.

(39) Antaris, A. L.; Seo, J.-W. T.; Green, A. A.; Hersam, M. C. *ACS nano* **2010**, *4*, 4725–4732.

(40) Zhang, Y.; Tunuguntla, R. H.; Choi, P.-O.; Noy, A. *Philosophical Transactions of the Royal Society B: Biological Sciences* **2017**, *372*, 20160226.

(41) Salva, R.; Le Meins, J.-F.; Sandre, O.; Brûlet, A.; Schmutz, M.; Guenoun, P.; Lecommandoux, S. *Acs Nano* **2013**, *7*, 9298–9311.

(42) Hubert, D. H.; Jung, M.; Frederik, P. M.; Bomans, P. H.; Meuldijk, J.; German, A. L. *Langmuir* **2000**, *16*, 8973–8979.

(43) Discher, B. M.; Won, Y.-Y.; Ege, D. S.; Lee, J. C.; Bates, F. S.; Discher, D. E.; Hammer, D. A. *Science* **1999**, *284*, 1143–1146.

(44) Kumar, M.; Habel, J. E.; Shen, Y.-x.; Meier, W. P.; Walz, T. *Journal of the American Chemical Society* **2012**, *134*, 18631–18637.

(45) Boroske, E.; Elwenspoek, M.; Helfrich, W. *Biophysical journal* **1981**, *34*, 95–109.

(46) Miao, L.; Seifert, U.; Wortis, M.; Döbereiner, H.-G. *Physical Review E* **1994**, *49*, 5389.

(47) Mui, B.; Döbereiner, H.; Madden, T.; Cullis, P. *Biophysical journal* **1995**, *69*, 930–941.

(48) Canham, P. B. *Journal of theoretical biology* **1970**, *26*, 61–81.

(49) Svetina, S.; Žekš, B. *European biophysics journal* **1989**, *17*, 101–111.

(50) Döbereiner, H.; Käs, J.; Noppl, D.; Sprenger, I.; Sackmann, E. *Biophysical journal* **1993**, *65*, 1396–1403.

(51) Yanagisawa, M.; Imai, M.; Taniguchi, T. *Physical review letters* **2008**, *100*, 148102.

(52) Kim, K.; Geng, J.; Tunuguntla, R.; Comolli, L. R.; Grigoropoulos, C. P.; Ajo-Franklin, C. M.; Noy, A. *Nano letters* **2014**, *14*, 7051–7056.

(53) Bhaskara, R. M.; Linker, S. M.; Vögele, M.; Köfinger, J.; Hummer, G. *ACS nano* **2017**, *11*, 1273–1280.

(54) Wadhwani, P.; Reichert, J.; Bürck, J.; Ulrich, A. S. *European Biophysics Journal* **2012**, *41*, 177–187.

Chapter 5

Carbon Nanotube Porins Protected Antifouling Biosensors

Limited biocompatibility and fouling propensity can restrict real-world applications of a large variety of biosensors. Biological systems are adept at protecting and separating vital components of biological machinery with semipermeable membranes that often contain defined pores and gates to restrict transmembrane transport only to specific species. Here we use a similar approach for creating fouling-resistant pH sensors. We integrate silicon nanoribbon transistor sensors with an antifouling lipid bilayer coating that contains proton-permeable carbon nanotube porin (CNTP) channels and demonstrate robust pH detection in a variety of complex biological fluids.

5.1 Introduction

Biological signaling mechanisms often involve small molecules, ions [1], and protons and facile in situ monitoring of the levels of these species is vital for medical diagnostics. Even the simplest signals, such as intracellular pH level can provide important information: for example, acidification of tumors because of elevated glucose uptake and lactic acid release is a biomarker of cancer cells [2]. Acidification of extracellular fluid is also one of the key processes during epileptic seizures, and monitoring and controlling pH of extracellular fluid has diagnostic and therapeutic potential [3]. Of all biosensing platforms,

This chapter is adapted with permission from "Chen, X., Zhang, H., Tunuguntla, R.H. and Noy, A., **2019**. Silicon Nanoribbon pH Sensors Protected by a Barrier Membrane with Carbon Nanotube Porins. *Nano letters*, 19(2), pp.629-634".

electrical sensors represent the best opportunity to develop implantable long-term sensing platforms because of their typically high sensitivity levels, fast response, and ease of multiplexing, signal processing, and coupling to wireless readout components [4, 5].

Although ion-selective electrodes represent the most ubiquitous electrical ion sensing platform, field effect transistors (FETs) have matured into a versatile alternative sensing platform that excels at continuous monitoring of small analyte levels [6]. FET sensors typically respond to the changes in the surface potential on the device channel region due to analyte binding or local ionization events and then amplify this signal using the high intrinsic transistor gain. Silicon nanowire/nanoribbon devices that exploited tailorable nature of silicon, advances in nanowire synthesis, and the existing mature silicon processing technologies have developed into a versatile platform for real-time, label-free, highly sensitive detection of disease biomarkers [7–12], DNA mismatches [13–15], and viruses [16].

As the FET-based biosensing and diagnostic platforms move into the realms of clinical use and potentially even long-term implantable applications, some of the limitations of the technology come into sharp relief, especially those related to device fouling in complex fluid environments. Researchers have used different fouling mitigation strategies based on polymeric surface coatings [17–19], bioinspired functionalization approaches [20, 21], and low-adhesion coatings [22]. Another general strategy to mitigate fouling is based on separating the sensing surface, which houses the analyte targets, from the measuring surface of the FET device. To implement this strategy, researchers developed sensors with side gate [23], floating gate [24, 25], and dual gate [26, 27]. We have also proposed an alternative strategy that uses a semipermeable lipid membrane coating on a device that incorporates specific membrane channels that isolates the sensor surface from the solution and only allows the species of interest to reach the device sensing surface [28, 29]. In the past, we have demonstrated the versatility of this approach by creating SiNW FET devices that incorporate specific ion channels [29], and ion pumps [30].

To create robust pH FET sensors based on this principle, the lipid membrane needs to incorporate a robust channel that is highly permeable (and, ideally, highly specific) to protons. We have recently demonstrated that narrow 0.8 nm diameter carbon nanotube porins (CNTPs) [31, 32], about 10 nm carbon nanotube (CNT) segments that spontaneously insert into a lipid membrane and form transmembrane channels, have extremely high proton permeability that is an order of magnitude higher than proton permeability of bulk water. Inert smooth surface of the 0.8 nm diameter nanotube pores, which is responsible for creating conditions that favor fast proton transport, also ensures that CNTPs can effectively block most of the fouling components of biological mixtures and prevent them from reaching the sensor surface.

In this work, we integrate the lipid membrane with small diameter CNTP pores with silicon nanoribbon (SiNR) field-effect transistor pH sensors (Figure 5.1). We show that this lipid-CNTP barrier membrane does not degrade the sensing performance of SiNR FET devices. Moreover, long-term fouling tests show that the lipid-CNTP coating makes SiNR FET sensors quite resistant to fouling by a range of complex biological fluids.

5.2 Device fabrication

SiNR-FET devices were fabricated from Silicon-on-Insulator (SOI) wafers (University Wafer, SIMOX, 2268). The device layer thickness was 50 nm, buried oxide (BOX) thickness was 145 nm, and the handle layer thickness was 775 μm. After careful piranha cleaning and oxygen plasma cleaning, the wafer was dehydrated and spin-coated with maN 2403 photoresist. Silicon nanoribbons (2 μm $\times$ 20 μm) were patterned with E-beam lithography (Vistec VB300 Electron Beam Lithography system) and developed in ma-D 532 Developer. After a brief descum cleaning the patterned wafer was etched at -120 °C for 20s using inductively coupled plasma (ICP) (Oxford Plasma Lab 100 Viper). Etched wafers were cleaned with acetone, rinsed with DI water, dried under nitrogen, descummed again, cleaned with acetone, rinsed with DI water, and dried under nitrogen. A thin (10 nm) dielectric silicon oxide layer on the silicon nanoribbon was then deposited using 250 cycles of plasma-enhanced atomic layer deposition at 300 °C (Oxford FlexAL). The wafers were subsequently annealed at 900 °C under nitrogen flow in a rapid thermal furnace for 10 min, followed by another acetone cleaning and DI water rinse. The wafer was dehydrated under a dry nitrogen stream and spin-coated with LOR 5A and S1805 photoresist. UV lamp was used to expose the electrode pattern. The wafer was developed in MF26A developer solution and then etched in 1:30 diluted buffer oxide etchant (BHF). The etched wafer was rinsed in DI water, dried with nitrogen and immediately transferred to the E-beam evaporator (Semicore SC600) to deposit 100 nm of nickel. Remover PG (heated to 70 °C) was used for metal liftoff. The wafer was rinsed with acetone and DI water, descummed in oxygen plasma (RIE) and then annealed in a rapid thermal annealing system at 380 °C. Finally, to create an about 0.8 μm-thick passivation layer, the device wafer was spin-coated with SU-8 (MicroChem SU-8 TF 6001) at 3k rpm and baked at 110 °C. In the final step, the small windows exposing the central regions of the nanoribbons were defined by photolithography, the wafer was baked at 110 °C, developed in SU-8 developer and descummed in oxygen plasma (RIE). Devices were diced out from the wafer and inspected with a field-emission SEM (Zeiss Gemini Ultra-55).

5.3 Performance benchmarking

A flow cell constructed of a custom-molded polydimethylsiloxane (Sylgard 184 Silicone Elastomer, Dow Corning, 0007997641) was placed on the top surface of the device and secured to a fixture. The flow cell was connected to a syringe pump (LEGATO 110, KD Scientific, 78-8110) with LDPE micromedical tubing (Scientific Commodities Inc., BB31695-PE/3, inner diameter 0.58 mm). The flow cell also incorporated an opening for a reference Ag/AgCl microelectrode that served as a gate electrode. Transfer characteristics were typically measured with the drain-source voltage (V_{DS}) at 0.1 V. The fluid cell was filled with the 10 mM HEPES-K, 30 mM KCl, and 150 mM NaCl, buffer solution (pH = 7.2). Only the devices with threshold potentials between -0.5 and -1.5 V were used for the subsequent measurements (a higher threshold voltage typically indicated poor silicide contact between the silicon nanoribbon and nickel electrode, whereas a lower threshold voltage indicated excessive dopant levels in the SOI wafer).

Device response kinetics were measured at 100 mV source-drain voltage. To ensure high device sensitivity we chose V_G values corresponding to the steepest slope in transfer characteristics curve; for our devices, this region corresponded to -1.3 $\pm$ 0.4 V. The average pH sensitivity for the uncoated SiNR devices (defined as the percentage change in drain-source current) was 49 $\pm$ 24% per pH unit. The rate of the device response does not reflect the intrinsic speed of the device; rather, SiNR device response is limited by the kinetics of the buffer exchange in the fluid cell, which was limited by the maximum syringe pump flow rate of 0.4 mL/min (higher flow rates tended to infuse air bubbles into the chamber and caused noisy spikes in the current readout).

5.4 Lipid membrane coating

CNTPs, DOPC LUVs, and CNTP-LUVs were prepared using previously reported protocols [33]. The lipid membrane coating was formed using Ca^{2+} induced vesicle fusion. Briefly, the fluid cell was filled with the solution of LUVs in 10 mM HEPES-K, 30 mM KCl and 150 mM NaCl buffer solution, incubated for 20 min, then washed with 50 mM $CaCl_2$ and 10 mM HEPES buffer, incubated for 10 min, and flushed with 10 mM HEPES-K, 30 mM KCl, and 150 mM NaCl buffer solution to get the lipid bilayer membrane on the device surface. Fluorescence microscopy images of the device surface were taken with Leica DM4000 equipped with Hamamatsu Orca Flash 4.0 camera. For the fluorescence recovery after photobleaching (FRAP) measurements after taking the initial image, a spot was bleached in the center of the device for 10

min. The recovery image was taken after 20 min of recovery.

5.5 Antifouling tests

Bovine serum albumin (BSA, Sigma, SLBK3715 V) was used at a concentration of 1.0 mg/mL in 10 mM HEPES-K, 30 mM KCl, and 150 mM NaCl buffer. Milk solution was prepared from condensed milk powder (purchased from a Target store) dissolved in 10 mM HEPES-K, 30 mM KCl, and 150 mM NaCl buffer to achieve a final concentration of 1.0 mg/mL milk protein density. Bovine plasma (Sigma, SLBS4463) was diluted in 10 mM HEPES-K, 30 mM KCl, and 150 mM NaCl buffer to a final concentration of 1.0 mg/mL. In a typical fouling experiment, the foulant solution was introduced into the fluid cell and the whole device assembly was kept in a humid environment for 60 h with aluminum foil wrapped on the outside to avoid light exposure. To retest the same device performance without lipid/CNTP coating it was removed by surfactant (Triton X-100, VWR, 0606C284) and the same fouling experiment protocol was repeated.

5.6 Results and discussion

Majority of silicon nanowire FET devices described in the literature fall into two loosely defined categories of "bottom-up" fabricated devices that use silicon nanowires fabricated by catalytic CVD and subsequently transferred onto the device wafer [34, 35] and "top-down" fabricated devices in which silicon nanowires or nanoribbons (SiNRs) are etched from a thin top layer of silicon-on-insulator (SOI) wafer [11]. For this work, we have used the second approach because it allowed us to fabricate a large number of devices with identical geometry on the wafer, although we note that our approach would be equally applicable to the "bottom-up" fabricated family of devices.

We used the "top-down" approach to fabricate FET devices with 2 μm wide SiNR channels (Figure 5.2). The device sensitivity and signal-to-noise ratio (SNR) can be optimized by tuning the geometrical dimensions of the device. In this work, we primarily focus on micron-scale nanoribbons, which simplify the fabrication process. The relatively wide channel surface characteristic of this device architecture also simplifies lipid membrane fusion on the SiNR and ensures that the coated surface would contain a large number of CNTPs. We also coated the SiNRs with a thin (10 nm) layer of SiO_2 deposited by atomic layer deposition, which after rapid thermal annealing step created a pinhole-free dielectric layer on the SiNR. Nanoribbons were then connected to nickel source and drain electrodes with nickel silicide contacts. Finally, we sealed the

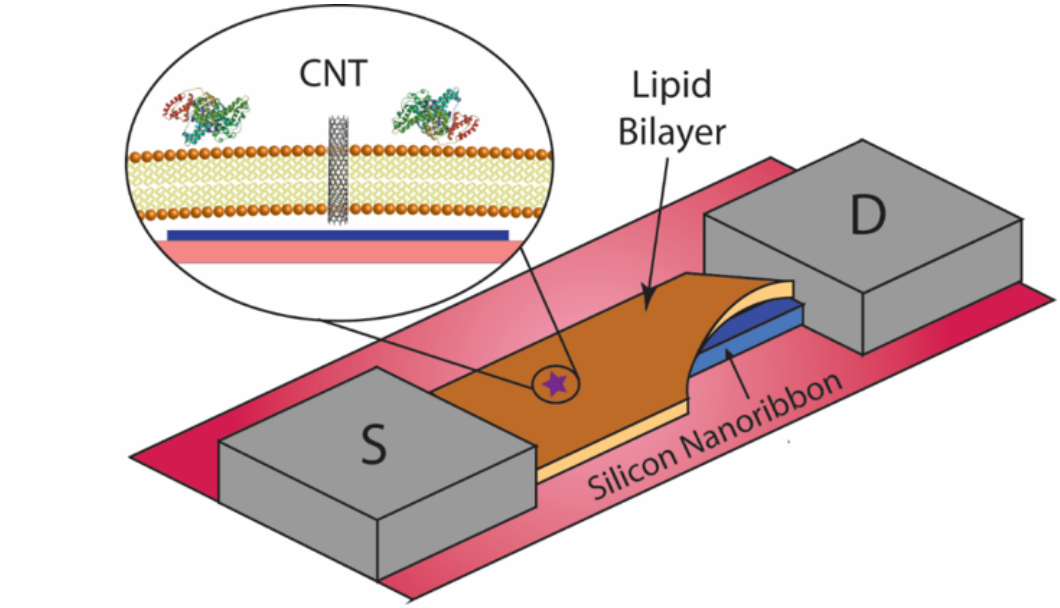

Figure 5.1: Silicon nanoribbon (SiNR) field-effect transistors. Schematics showing a silicon nanoribbon transistor device coated with the protective lipid layer. Source and drain electrodes of the device are marked as S and D, respectively. Inset shows a magnified region of the device showing carbon nanotube porins inserted into the lipid bilayer.

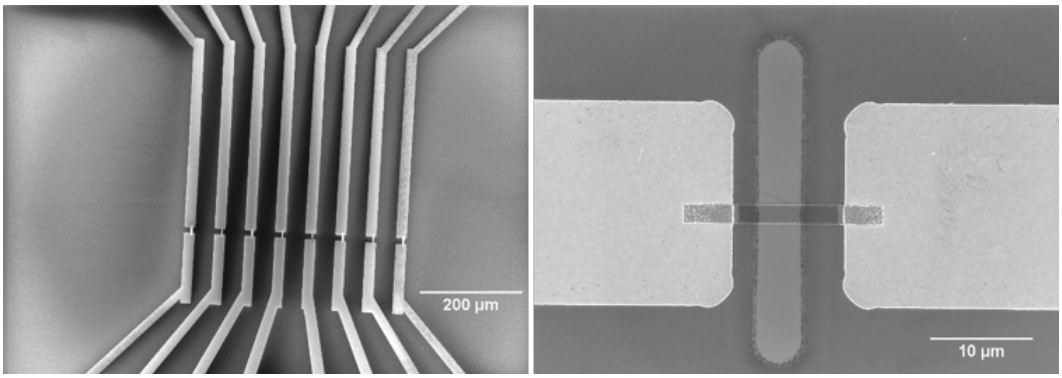

Figure 5.2: Scanning electron microscopy images of (left) an area of the chip showing several devices, and (right) a magnified image of an individual transistor device showing the source and drain electrodes connected with a nanoribbon and channel etched in the passivating layer to expose the central part of the ribbon.

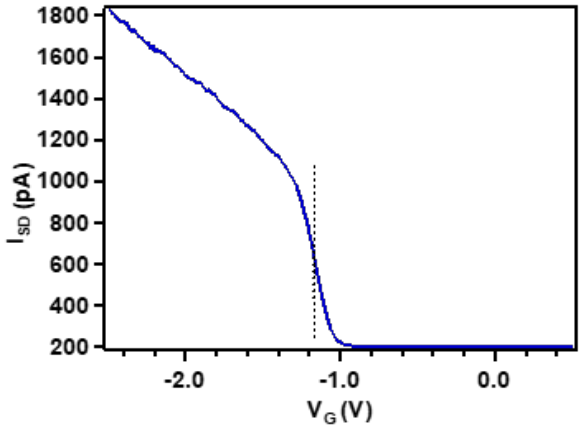

Figure 5.3: A plot of the source-drain current, I_{SD}, versus gate voltage, V_G (transfer characteristics), for an uncoated SiNR device. Dashed line indicates the gate voltage of -1.18 V, corresponding to the maximum transconductance of 3.8 nS.

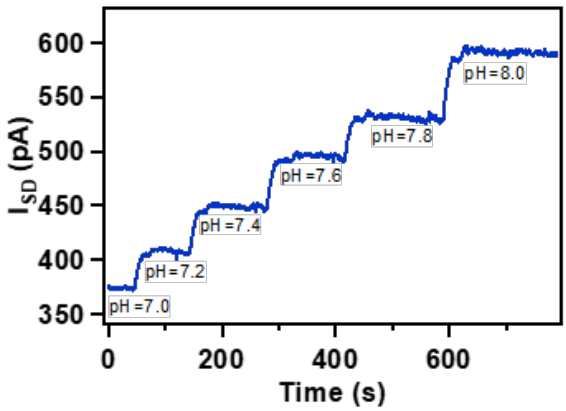

Figure 5.4: Time trace of the source-drain current (I_{SD}) of the uncoated device recorded as it was exposed to different pH buffer solutions (pH values indicated on the graph).

devices with an SU-8 epoxy protective layer that was etched to make only the central area of the nanoribbon accessible to the solution (Figure 5.2).

These devices exhibited a typical FET device transfer characteristic (I_{SD}-V_G) with the source-drain current turning off at gate voltages below -1 V and rapidly increasing at the gate voltages above this value (Figure 5.3). The typical field effect mobility of our SiNR FET devices was 0.014 cm^2 V^{-1} s^{-1} [36] and the electrical double layer capacitance per unit area was 26.4 μF cm^{-2} [37].

It is also important to optimize the device sensitivity to the changes of the environment around the nanoribbon. In principle, the highest sensitivity is achieved in the subthreshold regime where device conductance depends exponentially on gate voltage [36]. However, in this regime the device conductance and, consequently, the absolute magnitude of the signal is very small. Hence, we chose to operate our devices at the gate voltage that corresponds to the maximum device transconductance (Figure 5.3, dashed line), where a small change in the potential can still lead to a significant change in current/conductance.

pH sensitivity of silicon nanowire and nanoribbon-based FETs that arises from the ionization of the silanol groups on the device surface is well documented in the literature [38]. Electrical conductance of our devices also exhibited well-defined strong response to a stepwise pH increase of the buffer solution in the fluid cell (Figure 5.4). As expected, this response also did not depend on the direction or the order of the pH change. In our experimental setup, the device response kinetics are limited by the rate of buffer exchange in the fluid cell and thus do not reflect the true speed of the device.

To create the barrier lipid-CNTP membrane on the nanoribbon surface we fused DOPC-CNTP vesicles onto the device surface using protocols that we reported previously [29] (Figure 5.5). Fluorescence images (Figure 5.6) indicate that Si nanoribbons were completely covered by the lipid bilayer (to assist with imaging we added a small percentage of lipid labeled with the Texas Red dye to the lipid used for vesicle preparation). To assess the bilayer quality, we conducted fluorescence recovery after photobleaching (FRAP) experiments where we used a focused light spot from the microscope to bleach a region in the lipid bilayer and then monitored the diffusion of the labeled lipid molecules back into the bleached spot (Figure 5.7). Analysis of the line profiles of the resulting images (Figure 5.8) shows that unbleached lipid is able to diffuse back into the bleached spot and thus confirms that the SiNR was covered with the continuous lipid bilayer.

Lipid membrane coating has a profound effect on the electrical response of the device to the pH changes (Figure 5.9). The lipid coating makes the device virtually unresponsive to solution pH changes, confirming that the bilayer can act as a protective shield. Remarkably, addition of the CNTP channels, which

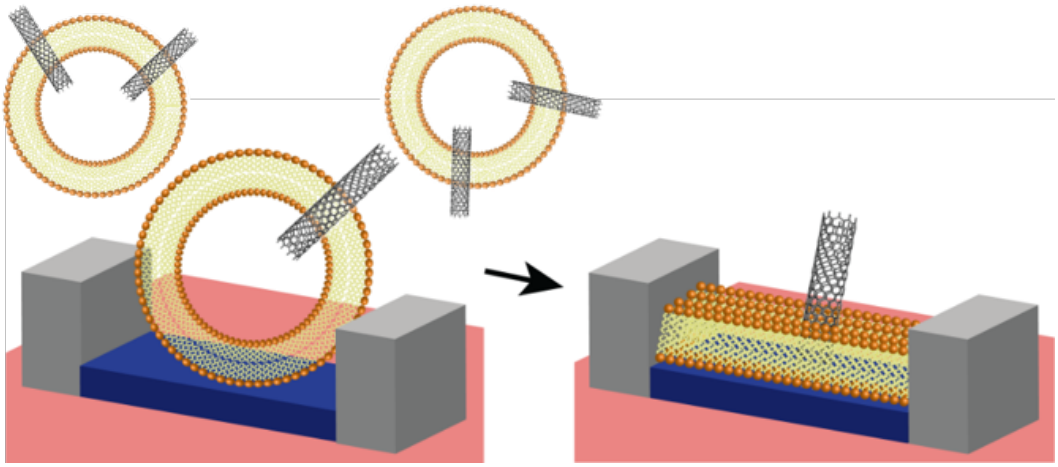

Figure 5.5: CNTP-SiNR pH sensors. Schematics showing the vesicle fusion process used to form the lipid-CNTP coating on the devices.

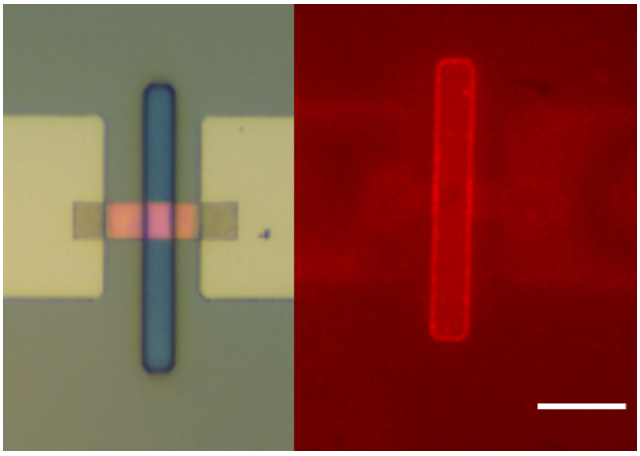

Figure 5.6: Bright-field (left) and fluorescence microscopy images of two SiNR devices coated with lipid bilayer. Scale bar: 10 μm.

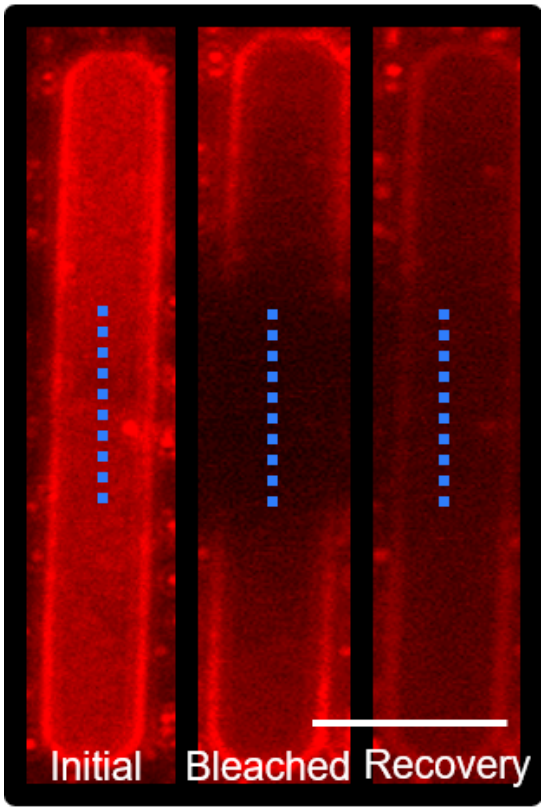

Figure 5.7: Fluorescence images of the etched channel region on a single device obtained before photobleaching, immediately after it, and after 20 min of recovery time. Scale bar: 10 μm.

act as high-efficiency proton conduits through the lipid bilayer, fully restores the pH sensitivity pattern of the device (Figure 5.9) with the average response going back up to about 59 $\pm$ 27% per unit pH.

We also evaluated the performance of our modified pH sensors in several mixtures that contained common foulants such as bovine serum albumin (BSA), milk, or bovine blood plasma. For each of these experiments, we have characterized the ability of our sensor to respond to variations in the solution pH values before and after continuous exposure to the different foulant mixtures (average protein concentration was 1.0 mg/mL) for 60 h. Taking BSA as an example, the literature on BSA fouling contains examples of foulant concentrations that range from 20 μg/mL to 10 mg/mL and fouling times that range from 6 h to 4 days [39–44]. We designed our fouling experiments to fall roughly in the middle of those conditions range. The data showed (Figure 5.10 - 5.12) that uncoated SiNR sensors were irreversibly fouled and completely lost their pH response for all three foulants used (Figure 5.10 - 5.12, blue traces). In

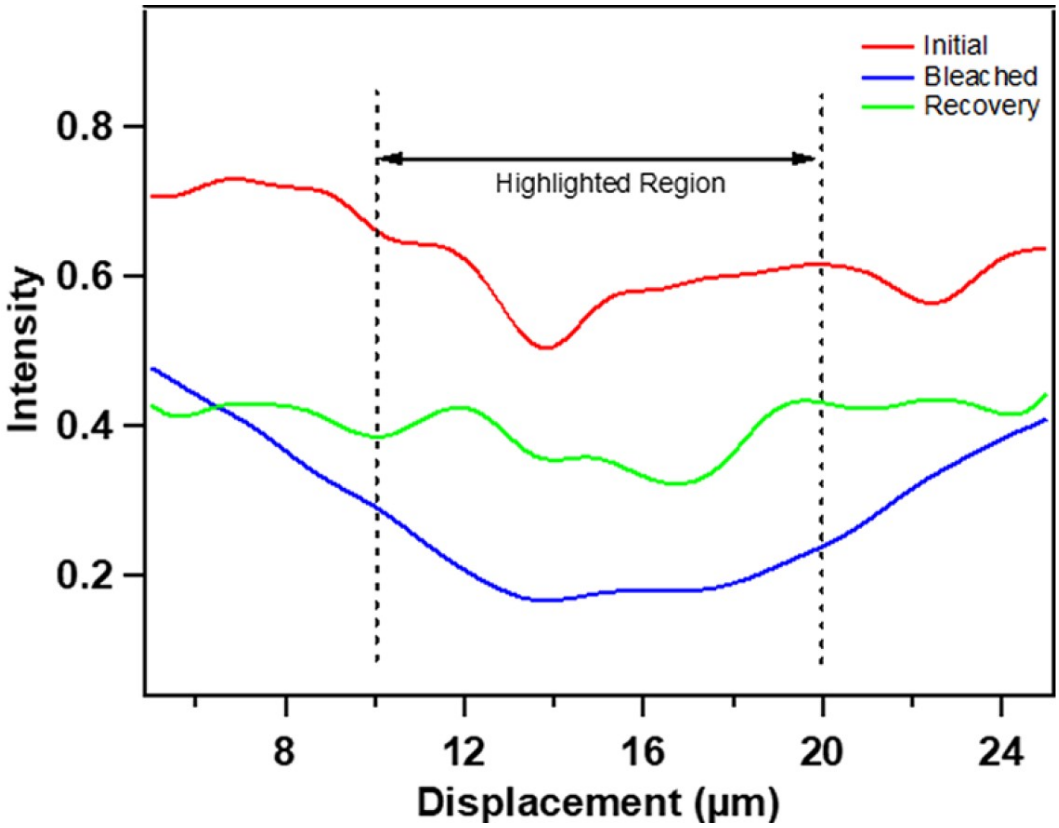

Figure 5.8: Line profiles of fluorescence intensity across the Si nanoribbon (indicated by the blue dashed lines) from Figure 5.7. The line profiles are low-pass filtered for clarity.

contrast, when the lipid bilayer incorporated CNTP channels, the pH response was preserved and showed very little signs of degradation (Figure 5.10 - 5.12, red traces), even in a rather complex fouling environment of blood plasma (Figure 5.12). For CNTP-SiNR sensors measured in the presence of foulants, we measured pH sensitivity of 43, 64, and 35% per unit pH in BSA, milk, and bovine blood plasma, respectively.

It is possible that the lipid bilayer itself acted as an antifouling coating to prevent the protein from sticking to the device surface. To test that possibility, we have used BSA labeled with a fluorescent FITC marker and imaged the device surface after exposure to this foulant. Both uncoated and lipid-CNTP-coated devices showed significant levels of protein adsorption on the surface (Figure 5.10, insets), indicating that lipid bilayer was not able to prevent protein adsorption on the device completely and that small size and high proton permeability of CNTP pores plays an important role in enabling the sensing

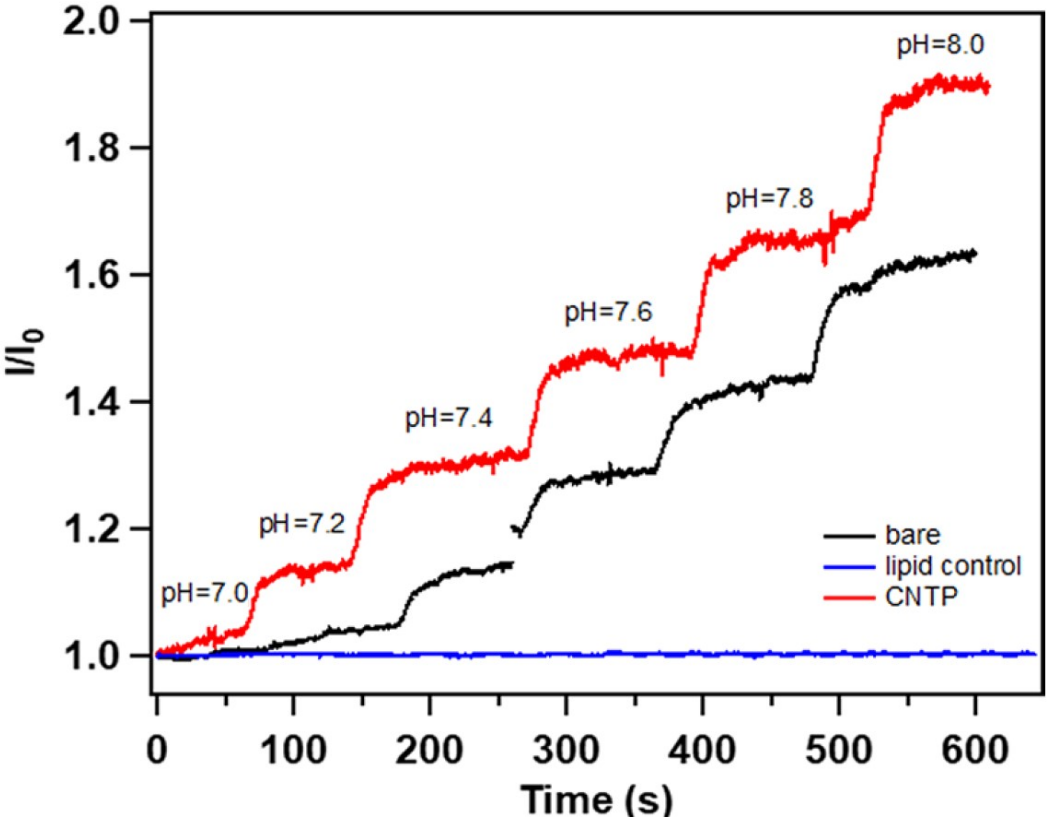

Figure 5.9: Time traces of the device source-drain current (I_{SD}) recorded in buffer solutions of different pH (as indicated on the graph) for the uncoated SiNR device (black), SiNR device coated with lipid bilayer (blue), and SiNR device coated with the lipid bilayer incorporating CNTP channels. All current traces were normalized to the initial current I_0.

functionality. We also note that even though our sensors show significant degree of fouling resistance they still can be defeated by a thick and dense fouling layer formed on top of the device. For example, we observed that very high concentrations of milk protein and BSA (about 40 mg/mL) that are close to the maximum solubility of the proteins tended to foul the device irreversibly even in the presence of CNTPs.0

5.7 Conclusions

These results show that lipid coating incorporating CNTP pores can act as an effective protective membrane for Si nanoribbon devices. Moreover, proton permeability, engineered by adding CNTPs to the membrane allowed those de-

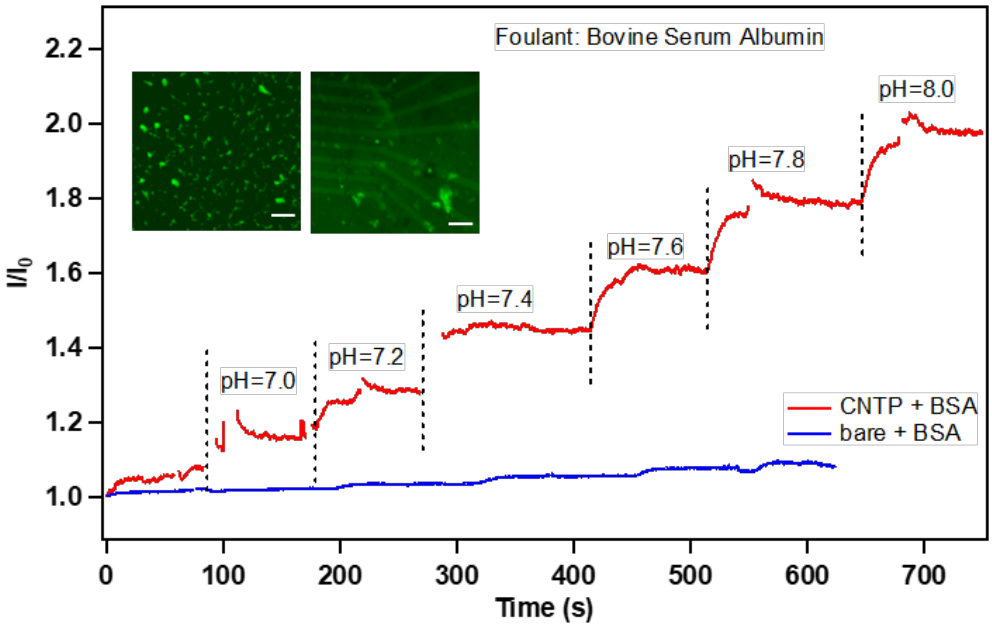

Figure 5.10: Time traces of a CNTP-SiNR device source-drain current (I_{SD}) recorded in buffer solutions of different pH in the presence of 1.0 mg/mL bovine serum albumin (red). Time trace of the I_{SD} for an uncoated SiNR device recorded in different pH buffers in the presence of bovine serum albumin (blue) shows strong fouling. Inset shows fluorescence microscopy images of FITC dye-labeled BSA attached to the surface of the lipid-coated (left) and uncoated (right) SiNR device chip Scale bar: 100 μm.

vices to report solution pH in complex multicomponent biological fluids with high fouling propensity. CNTP robustness and tunability of their permeability characteristics also opens up opportunities to expand the performance envelope of these sensors by engineering CNTPs to transmit specific ions and small molecules while blocking other biomolecules. These capabilities could transform SiNR or a similar SiNW platform into a versatile platform-type sensing technology that could be used in applications ranging from disease diagnosis, genetic screening, and drug discovery to environmental monitoring.

References

(1) Alberts, B. et al. Mol Biol Cell (Garland Science, New York), 2002.

(2) Damaghi, M.; Wojtkowiak, J. W.; Gillies, R. J. *Frontiers in physiology* **2013**, *4*, 370.

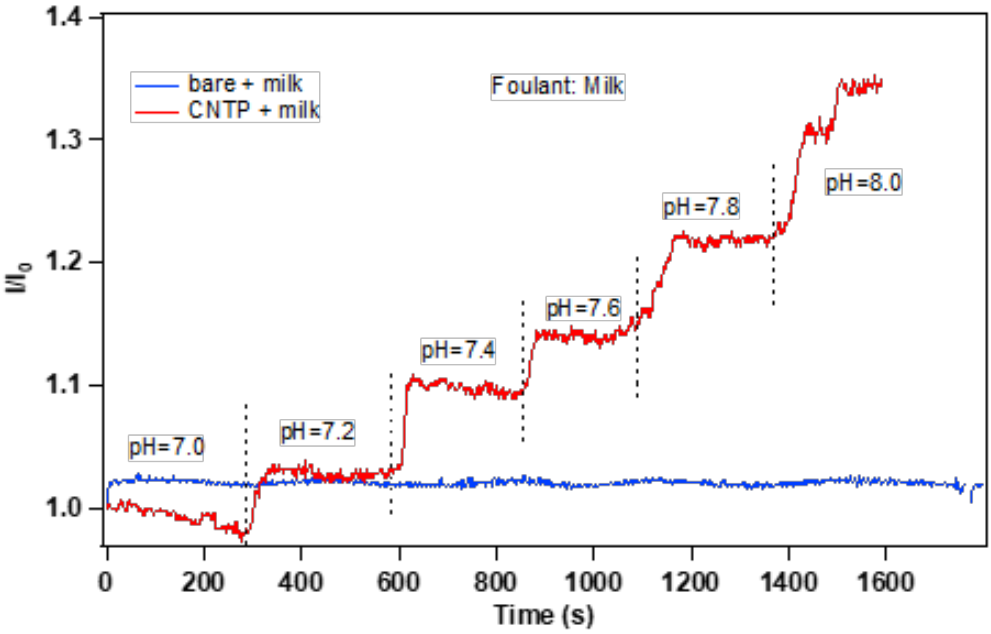

Figure 5.11: Time traces of CNTP-SiNR device (red) and uncoated SiNR device (blue) source-drain current (I_{SD}) recorded in buffer solutions of different pH after the devices were exposed for 60 h to simulated milk (1.0 mg/mL milk protein in 10 mM HEPES-K, 30 mM KCl, 150 mM NaCl buffer).

(3) Pavlov, I.; Kaila, K.; Kullmann, D. M.; Miles, R. *The Journal of physiology* **2013**, *591*, 765–774.

(4) Ronkainen, N. J.; Halsall, H. B.; Heineman, W. R. *Chemical Society Reviews* **2010**, *39*, 1747–1763.

(5) Lin, P.; Yan, F.; Chan, H. L. *ACS applied materials & interfaces* **2010**, *2*, 1637–1641.

(6) Chen, K.-I.; Li, B.-R.; Chen, Y.-T. *Nano today* **2011**, *6*, 131–154.

(7) Zheng, G.; Patolsky, F.; Cui, Y.; Wang, W. U.; Lieber, C. M. *Nature biotechnology* **2005**, *23*, 1294.

(8) Lin, T.-W.; Hsieh, P.-J.; Lin, C.-L.; Fang, Y.-Y.; Yang, J.-X.; Tsai, C.-C.; Chiang, P.-L.; Pan, C.-Y.; Chen, Y.-T. *Proceedings of the National Academy of Sciences* **2010**, *107*, 1047–1052.

(9) Wang, W. U.; Chen, C.; Lin, K.-h.; Fang, Y.; Lieber, C. M. *Proceedings of the National Academy of Sciences* **2005**, *102*, 3208–3212.

(10) Chua, J. H.; Chee, R.-E.; Agarwal, A.; Wong, S. M.; Zhang, G.-J. *Analytical chemistry* **2009**, *81*, 6266–6271.

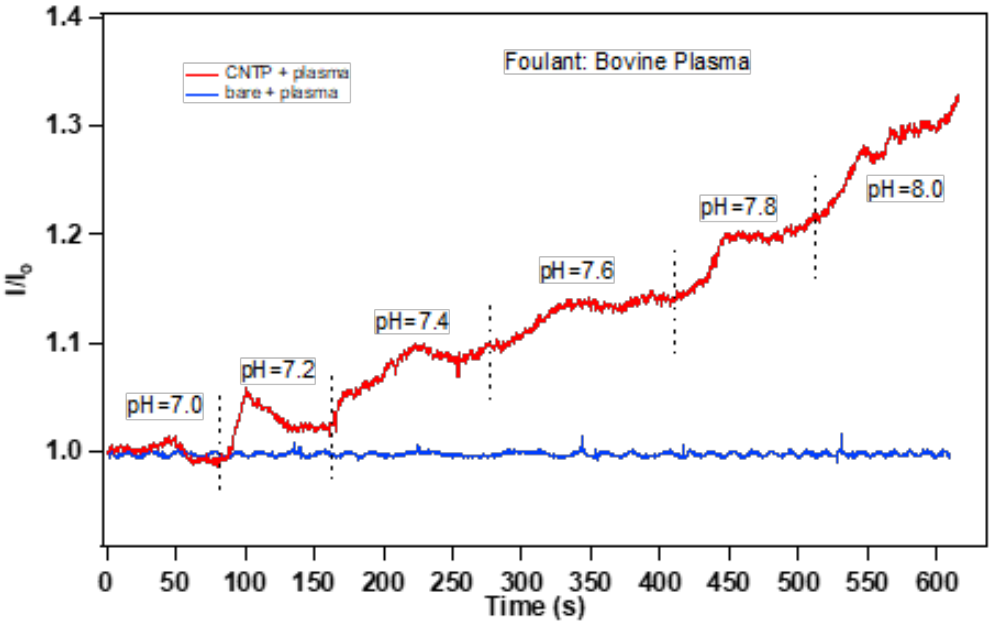

Figure 5.12: pH response of the CNTP-SiNR device after (red) exposure for 60 h to bovine blood plasma solution (1.0 mg/mL bovine plasma in 10 mM HEPES-K, 30 mM KCl, 150 mM NaCl). A control experiment shows pH response of an uncoated SiNR device after (blue) the same 60 h exposure to bovine blood plasma. On all panels the solution pH values are indicated on the graphs.

(11) Stern, E.; Klemic, J. F.; Routenberg, D. A.; Wyrembak, P. N.; Turner-Evans, D. B.; Hamilton, A. D.; LaVan, D. A.; Fahmy, T. M.; Reed, M. A. *Nature* **2007**, *445*, 519.

(12) Stern, E.; Vacic, A.; Rajan, N. K.; Criscione, J. M.; Park, J.; Ilic, B. R.; Mooney, D. J.; Reed, M. A.; Fahmy, T. M. *Nature nanotechnology* **2010**, *5*, 138.

(13) Hahm, J.-i.; Lieber, C. M. *Nano letters* **2004**, *4*, 51–54.

(14) Li, Z.; Chen, Y.; Li, X.; Kamins, T.; Nauka, K.; Williams, R. S. *Nano Letters* **2004**, *4*, 245–247.

(15) Ganguly, A.; Chen, C.-P.; Lai, Y.-T.; Kuo, C.-C.; Hsu, C.-W.; Chen, K.-H.; Chen, L.-C. *Journal of Materials Chemistry* **2009**, *19*, 928–933.

(16) Patolsky, F.; Zheng, G.; Hayden, O.; Lakadamyali, M.; Zhuang, X.; Lieber, C. M. *Proceedings of the National Academy of Sciences* **2004**, *101*, 14017–14022.

(17) Banerjee, I.; Pangule, R. C.; Kane, R. S. *Advanced materials* **2011**, *23*, 690–718.

(18) Krishnan, S.; Weinman, C. J.; Ober, C. K. *Journal of Materials Chemistry* **2008**, *18*, 3405–3413.

(19) Vaisocherová, H.; Brynda, E.; Homola, J. *Analytical and bioanalytical chemistry* **2015**, *407*, 3927–3953.

(20) Zhang, P.; Lin, L.; Zang, D.; Guo, X.; Liu, M. *Small* **2017**, *13*, 1503334.

(21) Nir, S.; Reches, M. *Current opinion in biotechnology* **2016**, *39*, 48–55.

(22) Detty, M. R.; Ciriminna, R.; Bright, F. V.; Pagliaro, M. *Accounts of chemical research* **2014**, *47*, 678–687.

(23) White, S. P.; Sreevatsan, S.; Frisbie, C. D.; Dorfman, K. D. *ACS Sensors* **2016**, *1*, 1213–1216.

(24) Meyburg, S.; Goryll, M.; Moers, J.; Ingebrandt, S.; Böcker-Meffert, S.; Lüth, H.; Offenhäusser, A. *Biosensors and bioelectronics* **2006**, *21*, 1037–1044.

(25) Meyburg, S.; Stockmann, R.; Moers, J.; Offenhäusser, A.; Ingebrandt, S. *Sensors and Actuators B: Chemical* **2007**, *128*, 208–217.

(26) Wu, T.; Alharbi, A.; You, K.-D.; Kisslinger, K.; Stach, E. A.; Shahrjerdi, D. *ACS nano* **2017**, *11*, 7142–7147.

(27) Ahn, J.-H.; Choi, S.-J.; Han, J.-W.; Park, T. J.; Lee, S. Y.; Choi, Y.-K. *Nano letters* **2010**, *10*, 2934–2938.

(28) Artyukhin, A. B.; Shestakov, A.; Harper, J.; Bakajin, O.; Stroeve, P.; Noy, A. *Journal of the American Chemical Society* **2005**, *127*, 7538–7542.

(29) Misra, N.; Martinez, J. A.; Huang, S.-C. J.; Wang, Y.; Stroeve, P.; Grigoropoulos, C. P.; Noy, A. *Proceedings of the National Academy of Sciences* **2009**, *106*, 13780–13784.

(30) Huang, S.-C. J.; Artyukhin, A. B.; Misra, N.; Martinez, J. A.; Stroeve, P. A.; Grigoropoulos, C. P.; Ju, J.-W. W.; Noy, A. *Nano letters* **2010**, *10*, 1812–1816.

(31) Geng, J.; Kim, K.; Zhang, J.; Escalada, A.; Tunuguntla, R.; Comolli, L. R.; Allen, F. I.; Shnyrova, A. V.; Cho, K. R.; Munoz, D., et al. *Nature* **2014**, *514*, 612.

(32) Tunuguntla, R. H.; Allen, F. I.; Kim, K.; Belliveau, A.; Noy, A. *Nature nanotechnology* **2016**, *11*, 639.

(33) Tunuguntla, R. H.; Escalada, A.; Frolov, V. A.; Noy, A. *Nature protocols* **2016**, *11*, 2029.

(34) Wang, M. C.; Gates, B. D. *Materials today* **2009**, *12*, 34–43.

(35) Su, B.; Wu, Y.; Jiang, L. *Chemical Society Reviews* **2012**, *41*, 7832–7856.

(36) Sze, S. M.; Ng, K. K., *Physics of semiconductor devices*; John wiley & sons: 2006.

(37) Park, S.; Lee, S.; Kim, C.-H.; Lee, I.; Lee, W.-J.; Kim, S.; Lee, B.-G.; Jang, J.-H.; Yoon, M.-H. *Scientific reports* **2015**, *5*, 13088.

(38) Mu, L.; Chang, Y.; Sawtelle, S. D.; Wipf, M.; Duan, X.; Reed, M. A. *IEEE Access* **2015**, *3*, 287–302.

(39) Wang, Y.-N.; Tang, C. Y. *Journal of Membrane Science* **2011**, *376*, 275–282.

(40) Li, Q.; Xu, Z.; Pinnau, I. *Journal of Membrane Science* **2007**, *290*, 173–181.

(41) Park, J.-S.; Chilcott, T.; Coster, H.; Moon, S.-H. *Journal of Membrane Science* **2005**, *246*, 137–144.

(42) Park, J.-S.; Choi, J.-H.; Yeon, K.-H.; Moon, S.-H. *Journal of Colloid and Interface Science* **2006**, *294*, 129–138.

(43) Mo, H.; Tay, K. G.; Ng, H. Y. *Journal of Membrane Science* **2008**, *315*, 28–35.

(44) Meng, H.; Cheng, Q.; Wang, H.; Li, C. *Journal of Chemistry* **2014**, *2014*.

Chapter 6

Outlook

The Carbon Nanotube Porin based biosensors can be a really versatile sensing platform (Figure 6.1). The spontaneous insertion of CNTPs into lipid bilayers opens up the possibility to achieve intracellular recording in cells through this CNTP cellular interface. The rim of CNTPs can be functionalized by EDC coupling [1]. This fine tune of porin rim can be used to achieve tailorable channels which allows only specific ions to go through. With minimal surface chemistry modification, the sensors can have receptors for different ions. By adopting a differential setup, the sensors can be used to perform multimodal sensing for different ions simultaneously. This chapter will cover some exploratory design ideas for this CNTP based sensing platform.

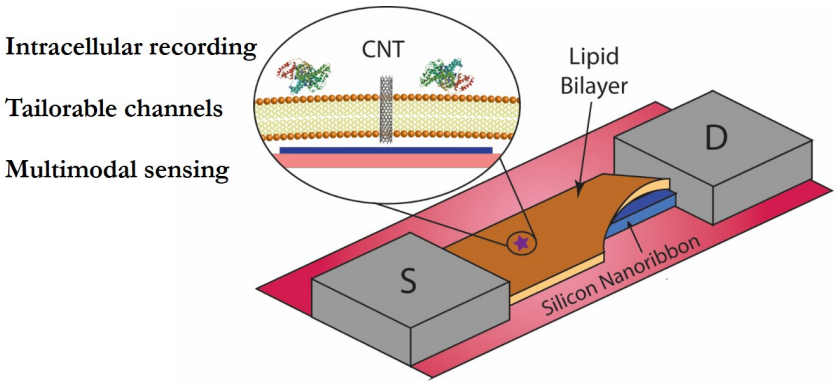

Figure 6.1: Outlook of Carbon Nanotube Porin based biosensors. From the channel part, we can expect intracellular recording possibility and tailor the channel to achieve selectivity. From the device end, we can attach receptor to the device surface enabling multimodal sensing ability.

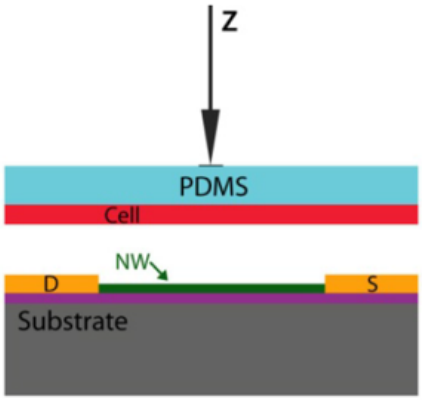

Figure 6.2: Schematic for cellular interface. The cells are cultured on a PDMS/glass substrate and brought down to the devices by glass pipette controlled by micro-manipulator. The use of PDMS will ensure homogeneous force to apply on the cells. (Reproduced with permission from [3]. © *2009 The National Academy of Sciences of the USA*).

6.1 Cellular interface

CNTPs have shown the ability to self-insert into synthetic lipid membranes as well as cellular membranes [2]. When the CNTPs are inserted into the supported lipid bilayers on device surface, they have the potential to penetrate through cellular membranes when the cells are brought down to the surface (Figure 6.2). Inspired by Lieber's previous work [3], I cultured cells on a PDMS/cover glass substrate and used micro-manipulator to mechanically push cells down to the device surface gently (Figure 6.3). Two major advantages of this setup are: a) device can be set up for cellular measurement before introducing cells into the system, thus minimizing the exposure time of cells to ambient environment (versus incubator condition of 37 °C and 5% CO_2); and b) the sensors can be recycled for multiple runs.

Ideally when the cells are brought down to the device surface during real-time measurements, we can expect to see the transition from intercellular potential to intracellular potential. This transition should also be reversible when we pull the cells up. We can also use chemicals to stimulate the cells and monitor the drug effect on the action potential.

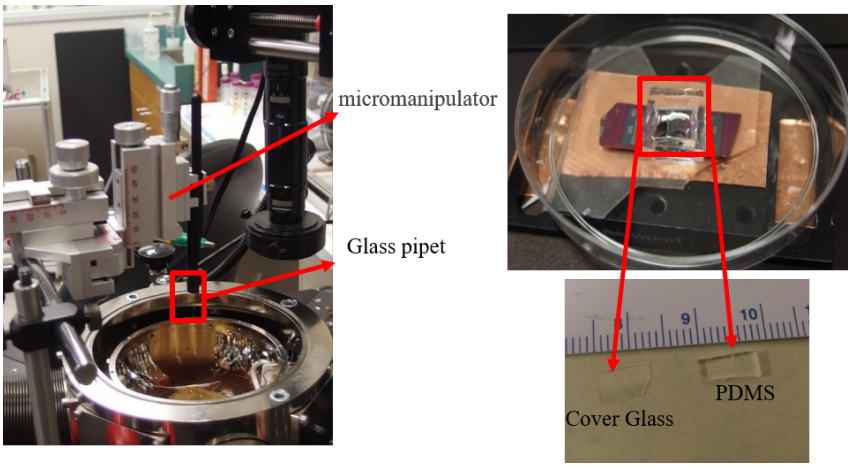

Figure 6.3: Instrument setup for cellular interface.(Left) the glass pipet is controlled by micro-manipulator to apply force on the cell substrate; (Right) the cells will be cultured on a substrate consist of PDMS and cover glass. The microfluidic chamber is made from PDMS as well.

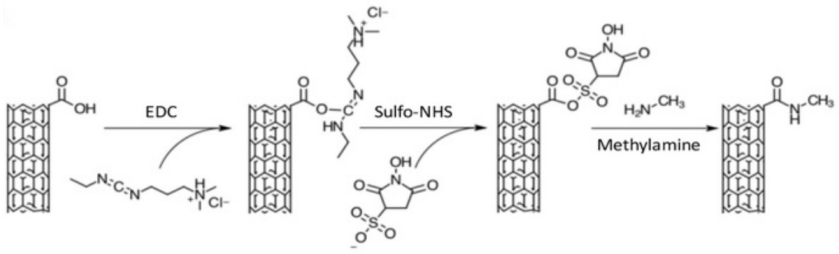

Figure 6.4: EDC coupling. Schematics of the functionalization of the CNTP rim with methylamide groups to neutralize the negative charges. (Reproduced with permission from [1]. © *2018 The Royal Society of Chemistry*).

6.2 Tailorable channels

As nanofluidic channels, CNTPs have extremely small diameters and hydrophobic inner walls. With chemical modification at the rim of CNTPs, they can expand their versatility as transport channel even more. Prior work has shown that we can use EDC coupling to functionalize the CNTP rims (Figure 6.4) [1]. By converting the -COOH groups at the channel entrance, we can have neutral and positively charged channels, thus changing the selectivity of the channels. Size exclusion, steric hindrance and Debye screening all contribute to the selectivity of CNTPs.

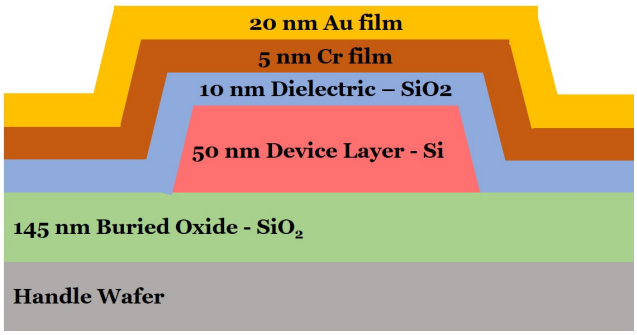

Figure 6.5: Au thin film coating schematics. The Au layer enables the gold-thiol chemistry. Due to the lattice mismatch, a thin layer of Cr will function as adhesive layer to help the atomic layer deposition of Au on SiO_2.

6.3 Multimodal sensing

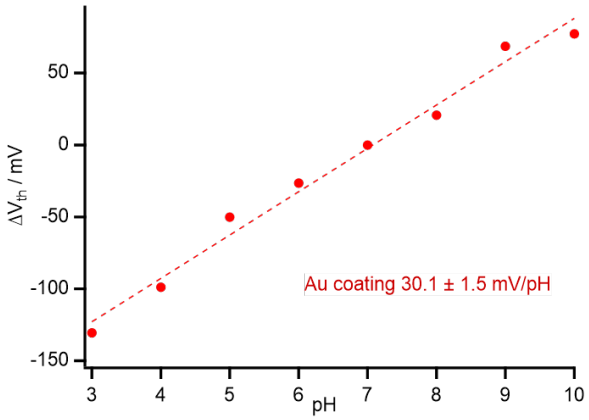

Figure 6.6: pH sensitivity of FETs with Au coating. The sensitivity is measured by the shift of threshold voltage (Δ V_{th}) of gold-coated FETs vs pH. When a thin layer of Au is deposited on the surface, less than 1% of gold atoms will be oxidized, thus having hydroxyl groups protruding out of the surface. These hydroxyl group will have similar protonation/deprotonation process as Silicon Nanoribbon FETs sustaining the pH sensitivity.

Field Effect transistor (FET) devices can easily expand its sensing ability by grafting receptors on the device surface. For example, the crown ethers are known to be good receptor for small cations, like Na^+ or K^+. One approach to have the crown ether assembled on the surface relies on the gold-thiol chemistry. So after the normal device fabrication protocol, we can deposit a thin

Figure 6.7: 15-Crown-5 Ether synthesis. Under an argon atmosphere, 5-aminobenzo-15-crown-5, racemic lipoic acid, and N,N′-diisopropylcarbodiimide were dissolved in anhydrous dichloromethane to have the final product for self assembled monolayer (SAM) formation.

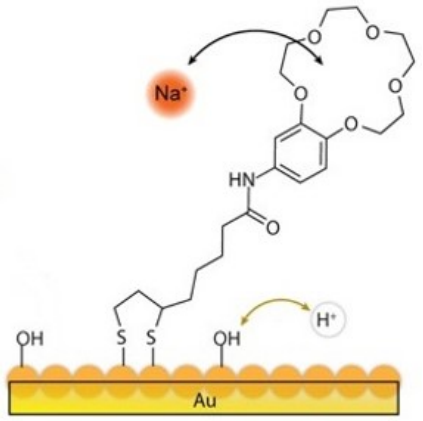

Figure 6.8: Immobilization reaction scheme of the sodium-selective crown ether on gold. The thiol only reacts with (reduced) gold atoms, leaving the number of hydroxyl groups unchanged. (Reproduced with permission from [4]. © *2013 American Chemical Society*).

layer of Au on top of the dielectric layer (Figure 6.5). 20 nm Au coating on FETs will not compromise device sensitivity. With Au coating, the threshold voltage shift of FETs can still respond to different pH (Figure 6.6). Self assembled monolayer of crown ethers (Figure 6.7) will have a good structural stability on gold surface [4] (Figure 6.8).

Wipf et al. have shown the multimodal sensing of proton and Na^+ by using a sodium selective 15-crown-5 ether [4]. They adopted a differential setup where one device is Crown Ether functionalized (active) while the other device is pristine (control) (Figure 6.9). By subtracting the control device signal from the active device signal, they can get the Na^+ concentration information, while the readout from control device indicates pH level. The results show good

selective sensitivity towards Na^+ concentration (Figure 6.10).

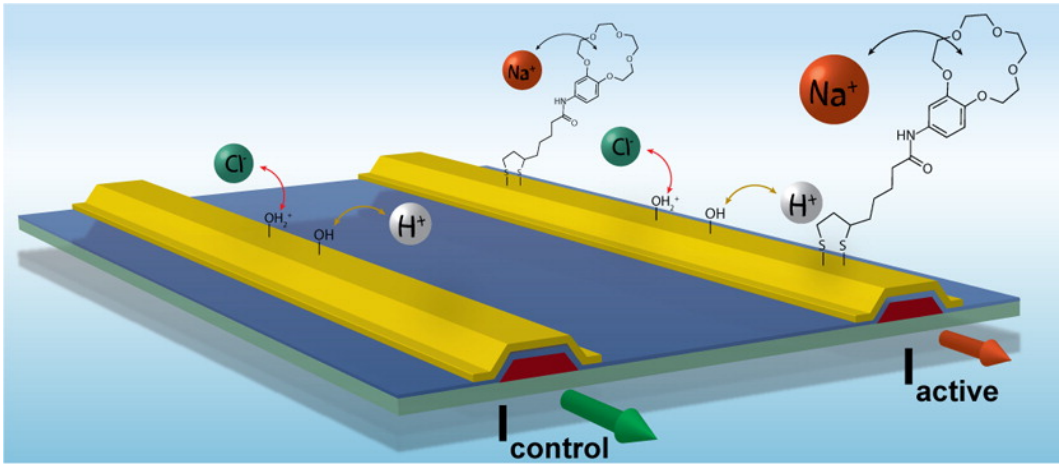

Figure 6.9: Scheme of differential setup of modified FETs for pH and cation sensing. In the active device, the threshold voltage shift (Δ V_{th}) is the indicator of both Na^+ and H^+ concentration in solution; while in the control device, the threshold voltage shift (Δ V_{th}) only corresponds to the pH level. Since the crown ether receptor only bonds to (reduced) gold atom, the hydroxyl groups in both devices remain the same. Therefore the contribution of pH level in active device is the same as in control device. We can simply subtract the control signal from the active signal to derive the Na^+ concentration information. (Reproduced with permission from [4]. © *2013 American Chemical Society*).

Similar setup can be used for other cations as well. For example, if we aim to achieve K^+ sensing, we can just switch 15-Crown-5 to 18-Crown-6 Ether. One thing to note here is that after Crown Ether SAM functionalization, it might be hard to fuse lipid vesicles on top of the device surface. One possible solution is to use thiolated tethered lipid anchoring (e.g. DSPE-$(PEG)_N$-SH, see Figure 6.11) to facilitate the vesicle fusion by reducing the height discrepancy between the complex device surface and the supported lipid bilayer with CNTPs.

References

(1) Tunuguntla, R. H.; Hu, A. Y.; Zhang, Y.; Noy, A. *Faraday discussions* **2018**, *209*, 359–369.

(2) Geng, J.; Kim, K.; Zhang, J.; Escalada, A.; Tunuguntla, R.; Comolli, L. R.; Allen, F. I.; Shnyrova, A. V.; Cho, K. R.; Munoz, D., et al. *Nature* **2014**, *514*, 612–615.

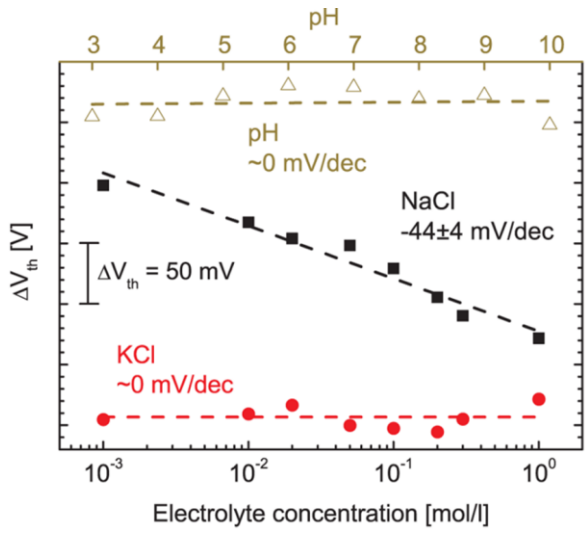

Figure 6.10: Differential threshold voltage (active device minus control device, ΔV_{th}) of gold-coated FETs vs the electrolyte concentration and pH. The 15-crown-5 ether shows high selectivity toward Na^+. (Reproduced with permission from [4]. © *2013 American Chemical Society*).

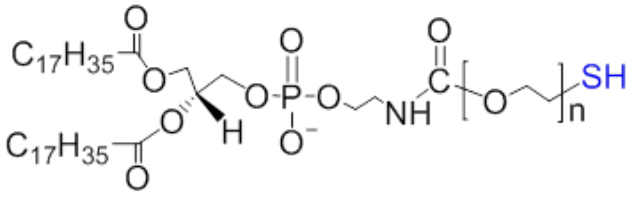

Figure 6.11: DSPE-$(PEG)_N$-SH thiolated tethered lipid. This lipid can be used to facilitate the vesicle fusion by reducing the height discrepancy between the complex device surface and the supported lipid bilayer with CNTPs. We can adjust the number of PEG groups to fine-tune the length of the lipid, matching the height difference on surface. The thiol group at the end can bond to the Au surface to help supported lipid bilayer formation.

(3) Cohen-Karni, T.; Timko, B. P.; Weiss, L. E.; Lieber, C. M. *Proceedings of the National Academy of Sciences* **2009**, *106*, 7309–7313.

(4) Wipf, M.; Stoop, R. L.; Tarasov, A.; Bedner, K.; Fu, W.; Wright, I. A.; Martin, C. J.; Constable, E. C.; Calame, M.; Schonenberger, C. *ACS nano* **2013**, *7*, 5978–5983.

Appendix A

Silicon Nanoribbon FET Fabrication Protocol

SIMOX SOI wafer specification:
Device thickness: 50nm
BOX thickness: 145nm
Handle thickness: 775um

Optional wafer clean step (only for dirty wafers, do not use for clean wafers out of the wafer box): piranha clean for 30 min and oxygen plasma for 5 mins (descum recipe).

Ebeam Lithography and Cryo Etching

1. Dehydrate clean wafer at 120 C on the hotplate for 5 min
2. Spin HMDS at 1k rpm, then dehydrate at 100 C for 1 min
3. Spin maN 2403 Ebeam resist at 3k rpm, then bake at 100 C for 2 min
4. Ebeam writing and development (Staff Scientist)
5. Descum in oxygen plasma (RIE) for 30s
6. Turn on liquid nitrogen supply and set VIPER plasma etcher to -120 degree
7. Etch for 20s with Xi Chen Cryo Silicon receipt in VIPER plasma etcher
8. Inspect the edge of the etched wafer (additional 5 second of etch might be required if the edge is not etched completely)
9. Clean the wafer with acetone, rinse with water, and dry with nitrogen
10. Descum in oxygen plasma (RIE) for 4 min
11. Clean the wafer with acetone

Atomic Layer Deposition

1. Dehydrate wafer at 120 C on the hotplate for 5 min
2. Set ALD tool to 300 degrees
3. Deposit silicon oxide for 250 cycles at 300C
4. Set rapid thermal furnace to 900C for 10min, ramping time 2min
5. Place wafer inside the furnace and seal the chamber
6. Set nitrogen flow at 20 sccm and wait for 30 min
7. Start the annealing process
8. When the chamber cools to below 100C, turn off the nitrogen flow and remove the wafer.
9. Clean the wafer with acetone, rinse with water, and dry with nitrogen

Electrode Deposition

1. Dehydrate wafer at 120C on the hotplate for 5min
2. Spin LOR 5A at 3k rpm and bake for 5 min at 180C
3. Spin S1805 at 3k rpm and bake for 90s at 115C
4. Align electrode mask to the etched wafer
5. Expose for 2s at 17mW/cm^2
6. Develop in MF 26a solution for 30s
7. Vent Semicore ebeam evaporator
8. Prepare 1 to 30 diluted buffer oxide etchant (BHF)
9. Etch the wafer in diluted BHF for 1 min
10. Rinse in water and dry under nitrogen
11. Place the wafer inside of the evaporator immediately after drying
12. Once the evaporator pumped down to 2e-6 torr, deposit 100nm of Nickel
13. Heat Remover PG at 70 C on the hotplate
14. Place the evaporated wafer in the hot Remover PG for metal liftoff
15. Once metal is lifted off from the wafer, remove the wafer from Remover PG
16. Rinse with acetone and water
17. Descum in oxygen plasma (RIE) for 2 min
18. Place the wafer inside the rapid thermal annealer (RTP1 in Berkeley nanolab), use XC_380 receipt to anneal Nickel

SU8 Electrode Passivation

1. Dilute 1 part of SU-8 3010 with 2 part of SU-8 thinner

2. Sonic and filter the diluted solution
3. Spin SU-8 at 1000k
4. Bake at 95 C for 2 mins
5. Align the passivation mask layer on the wafer
6. Expose for 6s at 14mW/cm^2
7. Post bake for 2 min at 95 C
8. Develop in SU8 developer for 2 min
9. Descum in oxygen plasma for 2 min

Appendix B

Cell Culture Protocol

Cell Line Name: NG108-15 Cell Line
ECACC No.: 88112302
ATCC No.: HB-12317
Key Words: Mouse neuroblastoma x rat glioma hybrid
Cell Line Description: Neuroblastoma x glioma hybrid was form by Sendai virus-induced fusion of the mouse neuroblastoma clone N18TG-2 and the rat glioma clone C6BV-1
Species: Rat/mouse hybrid

Morphology: Neuronal

Subculture Routine: Split sub-confluent cultures (70-80%) 1:4 to 1:10 seeding. Cells adhere lightly, detach by gently knocking the flask. DO NOT use trypsin. 5% CO2, 37C. The cells do produce large amounts of CO2. Media change may be necessary.

Materials:

Dulbecco's Modified Eagle Medium (DMEM) (Gibco 11965-084):
Contains 4,500 mg/L D-glucose, and L-glutamine, but no sodium pyruvate.

Hypoxanthine-Aminopterin-Thymidine (H.A.T.) 500X concentrate (ATCC 69-X)

Penicillin-Streptomycin (Gibco 15140)

Stock DMEM:
1000mL DMEM + 1 bottle H.A.T + 10mL PenStrep = 1000mL DMEM with 1% PenStrep

Proliferation Medium:
90% Stock DMEM + 10% FCS

Differentiation Medium:
90% Stock DMEM + 10% Proliferation Medium or
99% Stock DMEM + 1% FCS

Cryopreservation Medium:
92.5% Proliferation Medium + 7.5% DMSO

Passaging Cells:

- Upon 70-80% confluency, detach cells by gently shooting streams of media at the bottom of the flask or tapping the flask for a few minutes
- Pipette cells up and down 5 to 10 times to disperse cell suspension
- Centrifuge cell suspension at 800-1000rpm for 5min
- Resuspend cells in 1ml of fresh medium
- Subculture cells at 1:4 to 1:10
- Remaining cells can be counted and used for experiments

Counting and Seeding Cells for Experiments (continue from Subculture):

- Dilute 50ul of the 1ml cell suspension with 450ul of fresh medium in an Eppendorf tube
- Vortex cell suspension and add 10ul to each end of the hematocytometer
- Count cells and calculate cell density of the 1ml cell suspension
- Prepare cell solution from the 1ml cell suspension
- Depending on experiment, cell solution can be prepared using proliferation or differentiation medium.
- Seed cells at 2000 to 6000 cells in 100ul of medium per well in 96-well plate or at 5000 to 15000 cells in 400ul of medium per well in 8-well chamber slide

Cryopreservation:

- To freeze cells, upon 70-80% confluency in T-25 flask
  - Detach cells and centrifuge cell suspension at 800-1000rpm for 5min
  - Resuspend cells in 4 to 10ml of cryopreservation medium
  - Aliquot cell suspension into 4 to 10 cryogenic vials
  - Store cryogenic vials at -20C for a few hours, then at -80C overnight, finally transfer to liquid nitrogen storage tank next day (vapor phase preferred)
- To thaw cells,
  - Retrieve cryogenic vials from liquid nitrogen storage tank
  - Thaw vial quickly in a 37C water bath
  - Immediately transfer cell suspension to a T-25 flask and add 10ml of fresh, warm proliferation medium to the flask 1ml at a time over a few minutes

Fixing Cells:

- Add equal volume of pre-warmed 4% paraformaldehyde to cell culture
- Incubate for at least 30-40min at room temperature or 37C
- Remove paraformaldehyde/medium
- Wash cells with PBS

Permeabilize Cells:

- After fixing, add enough 0.2% Triton X-100 (prepared in PBS) to cover cells
  - Prepare 0.2% Triton X-100 from a 2% Triton X-100 stock
  - Prepare 2% Triton X-100 stock in PBS, store at 4C
- Incubate for 5min at room temperature

Appendix C

Neuronal Cell Seeding Protocol

Materials Preparation

- substrates
  - **devices**: pyrex cloning cylinders (6 mm) sealed onto devices with PDMS adhesive; UV sterilization for 30 mins.
  - **polystyrene 96-well plate**
  - **PDMS/cover glass**: 4×6 mm^2 PDMS and cover glass pieces heated at 120 °C for 3 hrs; ethanol wash 3X and UV sterilization for 30 mins.
- Poly-D-lysine (in borate buffer, store at -20 °C)
- Sterile distilled water
- Neuron media
  - Neural basal plus medium
  - Gentamycin
  - GlutaMax
  - B27

Device/Substrate Surface Treatment

PDL coating on all surfaces

- Add 70 μL of PDL
- incubate in BSC for 1 hr
- Remove PDL, wash 3X with 200 μL sterile distilled water

- Air dry over night
- Add 70μL of neuron media and incubate in incubator

Seeding

Seed the cells at the cell count of $\sim 1 \times 10^6$ cells

- seed cells at seeding density of $\sim$ 1200 cells/mm^2
  - 27.6 μL on device (surface area $\sim$ 0.23 cm^2)
  - 38.4 μL on well (surface area $\sim$ 0.32 cm^2)
  - 28.8 μL on PDMS/glass (surface area $\sim$ 0.24 cm^2)
- change media after 1 hr of seeding
- T25 flask: seed remaining cells ($\sim$ 641 μL remaining); top up flask with 5 mL of neuron media.

Media Change

50% media change every 3 DIV.